POLITECNICO
MILANO 1863

SCUOLA DI INGEGNERIA INDUSTRIALE
E DELL'INFORMAZIONE

Numerical Simulation of a Vertical Axis Wind Turbine Using the Actuator Line Method: Geometric Characterization and Validation Against Experimental Data

TESI DI LAUREA MAGISTRALE IN
ENERGY ENGINEERING
INGEGNERIA ENERGETICA

Author: **Sandra Giulia Fodor**

Student ID: 10729228
Advisor: Vincenzo Dossena
Academic Year: 2025-26

Abstract

Vertical-axis wind turbines are often proposed for small-scale wind energy applications because they can operate independently of wind direction and have a relatively simple mechanical layout. Nevertheless, predicting their aerodynamic performance is challenging, particularly at low tip speed ratios, where the angle of attack changes continuously and effects such as dynamic stall and blade–wake interaction become important. This thesis evaluates whether an actuator line model implemented in OpenFOAM can be used as a computationally efficient alternative to full three-dimensional CFD simulations for predicting the performance of a small vertical-axis wind turbine. The numerical model is validated against wind tunnel measurements obtained from the physical turbine. Since the original blade geometry was not available as a digital model, the blade profile was first reconstructed through reverse engineering and then used in two-dimensional CFD simulations to generate the aerodynamic coefficient database required by the actuator line model. Different solver and turbulence model configurations were tested, and transient simulations with the K-ω SST turbulence model were selected as the basis for the aerodynamic data. The actuator line model was implemented in turbinesFoam, and simulations were performed in the low tip speed ratio range measured experimentally. The results show that including dynamic stall improves the predicted power trend compared with the uncorrected model. Wind tunnel tests also showed limited power production across the tested operating range. Overall, both the experimental and numerical results indicate that the analyzed turbine produced low power under the tested operating conditions. Therefore, the actuator line model can be considered useful for preliminary analysis, but in its present form it is not yet sufficient for reliable quantitative prediction of this turbine. Further work is required on the aerodynamic coefficient database, the dynamic stall calibration, and the experimental characterization.

Key-words: Actuator Line Method, Vertical Axis Wind Turbine, dynamic stall, low tip speed ratio, wind tunnel experiment, OpenFOAM.

Abstract in Italiano

Le turbine eoliche ad asse verticale sono spesso proposte per applicazioni di piccola scala poiché possono operare indipendentemente dalla direzione del vento e presentano una configurazione meccanica relativamente semplice. Tuttavia, la previsione delle loro prestazioni aerodinamiche risulta complessa, soprattutto a bassi tip speed ratio, dove l'angolo di attacco varia continuamente e fenomeni come lo stallo dinamico e l'interazione tra pala e scia assumono un ruolo significativo.

Questa tesi valuta se un modello ad actuator line implementato in OpenFOAM possa essere utilizzato come alternativa computazionalmente efficiente alle simulazioni CFD tridimensionali complete per la previsione delle prestazioni di una piccola turbina eolica ad asse verticale. Il modello numerico è stato validato mediante misure sperimentali ottenute in galleria del vento sulla turbina reale.

Poiché la geometria originale delle pale non era disponibile in formato digitale, il profilo aerodinamico è stato inizialmente ricostruito tramite reverse engineering e successivamente utilizzato in simulazioni CFD bidimensionali per generare il database dei coefficienti aerodinamici richiesto dal modello ad actuator line. Sono state testate diverse configurazioni di solutori e modelli di turbolenza e, tra queste, le simulazioni transitorie con il modello di turbolenza k-ω SST sono state selezionate come base per la generazione dei dati aerodinamici.

Il modello ad actuator line è stato implementato in turbinesFoam e le simulazioni sono state eseguite nell'intervallo di bassi tip speed ratio investigato sperimentalmente. I risultati mostrano che l'inclusione dello stallo dinamico migliora l'andamento della potenza prevista rispetto al modello privo di correzioni. Le prove in galleria del vento hanno inoltre evidenziato una limitata produzione di potenza nell'intero intervallo operativo analizzato.

Nel complesso, sia i risultati sperimentali sia quelli numerici indicano che la turbina studiata ha prodotto una bassa potenza nelle condizioni operative considerate. Pertanto, il modello ad actuator line può essere ritenuto utile per analisi preliminari, ma nella sua forma attuale non risulta ancora sufficiente per una previsione quantitativa affidabile delle prestazioni di questa turbina. Saranno necessari ulteriori sviluppi riguardanti il database dei coefficienti aerodinamici, la calibrazione del modello di stallo dinamico e la caratterizzazione sperimentale.

Parole chiave: Actuator Line Method, turbina eolica ad asse verticale, stallo dinamico, basso tip speed ratio, esperimento in galleria del vento, OpenFOAM.

Contents

Motivation and Objectives

The aerodynamic analysis of VAWTs is complicated by the fact that the blades do not operate under steady inflow conditions. During each revolution, the relative velocity and angle of attack vary continuously, producing cyclic aerodynamic loading, torque oscillations, flow separation, and, especially at low tip-speed ratios, dynamic stall. As a result, power and torque cannot be estimated only from steady aerodynamic assumptions.

A complete 3D CFD simulation of the rotating turbine geometry can provide a detailed representation of the flow around the blades, the wake development, and the interaction between the rotor and the surrounding flow. However, this approach requires the generation of a complex moving mesh and involves a high computational cost, especially when several operating conditions must be simulated. For this reason, simplified numerical methods such as the actuator line method represent an attractive alternative. In this approach, the blades are not explicitly meshed as solid surfaces but are represented through body forces distributed along actuator lines. This allows the main aerodynamic effect of the rotor to be included in the flow solution with a significantly lower computational cost.

The main objective of this thesis is to assess whether an actuator line computational model can be considered a valid alternative to a fully meshed 3D CFD simulation for the prediction of the global aerodynamic performance of a small vertical-axis wind turbine. The objective is not to replace blade-resolved CFD for the detailed study of local flow phenomena, but to assess whether the ALM can provide reliable engineering-level predictions of mean torque and power coefficient in the low tip-speed-ratio operating range.

To evaluate this, the computational model is compared with experimental data obtained from wind tunnel measurements. The numerical part of the work includes the reconstruction of the Darrieus blade geometry, the generation of a dedicated aerodynamic coefficient database from 2D CFD simulations, and the implementation of the actuator line model in OpenFOAM/turbinesFoam. The experimental part provides the reference power coefficient curve through torque and rotational speed measurements. The comparison between both approaches is used to determine whether the numerical model captures the same performance trend observed experimentally and to identify the possible causes of discrepancy.

A secondary but important motivation of the work is related to the actual power production of the turbine. The device was presented by its manufacturer as capable of generating a significant amount of power. For this reason, an independent quantitative assessment is necessary in order to verify whether this expectation is supported by measured and simulated performance. Both the computational and experimental analyses provide useful information in this regard. If the predicted and measured power coefficients are low, this indicates that the real energetic contribution of the turbine may be more limited than suggested by the original performance claims.

The problem addressed in this thesis is therefore both methodological and practical. From the methodological point of view, the work assesses the validity and limitations of the actuator line method as a reduced-cost alternative to full 3D turbine simulations. From the practical point of view, it uses the numerical and experimental results to evaluate whether the turbine, in its present configuration and under the tested operating conditions, is capable of producing significant power.

1 Introduction

This chapter provides an overview of the historical development of wind turbines and introduces the main characteristics of different turbine concepts, with particular attention to the advantages and limitations of horizontal- and vertical-axis wind turbines.

1.1. Wind Energy Generation and History

Wind energy is an indirect form of solar energy, generated by the Sun's nuclear fusion processes that produce heat and radiation. A small fraction of this solar energy reaches Earth, and about 2% is converted into wind.

Wind is created by air moving from high pressure to low pressure regions, and stronger pressure gradients produce stronger winds and more extractable wind power. However, wind generation is complex and influenced by several factors, the most important being uneven solar heating, the Coriolis effect from Earth's rotation, and local geography. Among these, uneven solar radiation is the dominant cause. Because Earth is spherical, the equator receives more direct sunlight than the poles, creating temperature and pressure gradients that drive large scale air circulation (Figure 1-1) [1].

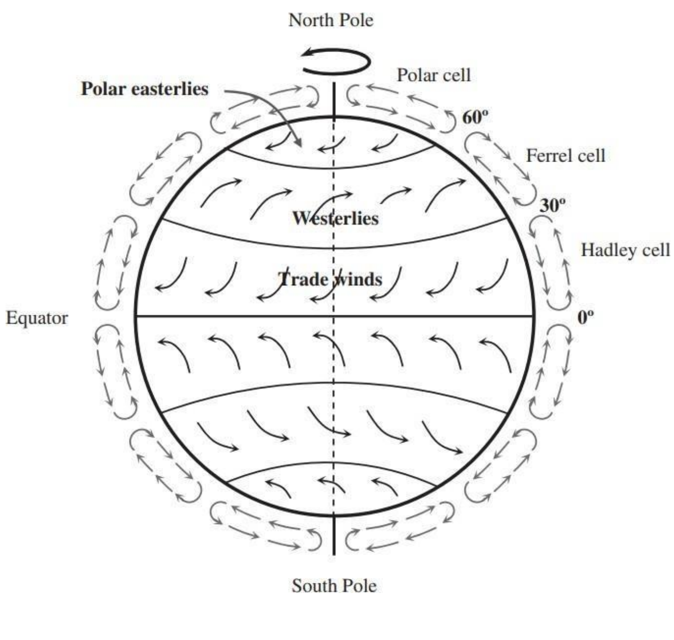

Figure 1-1: Idealized atmospheric circulation

The use of wind by humans dates back several millennia. It is documented that from as early as 3400 BC the ancient Egyptians exploited the wind to sail on the Nile river. Wind-powered sailing later became essential for transport, trade, and exploration in many ancient civilizations. [2].

About 300 BC, the ancient Sinhalese made use of strong monsoon winds to supply air to their furnaces, allowing them to reach temperatures above 1100 °C for smelting iron and enabling them to produce high-carbon steel.

Around 200 BC, the first true windmill was built in China for pumping seawater to extract salt. By about 600 AC, windmills were also being used to grind wheat in the regions corresponding to present-day Iran and Afghanistan. These early machines (Figure 1-2) had a vertical axis and relied on drag to capture wind power, which greatly limited their efficiency. Because part of the rotor always moved against the wind, they required a protective wall on one side, meaning they could only operate effectively in locations where the wind direction was predominantly constant, since they were unable to adjust to directional changes. In general, lift-based rotors can reach higher efficiencies than drag-based rotors, which explains the limited performance of these early vertical-axis windmills. [3].

Figure 1-2:Windmills in Iran

Much later, in the 1180s, horizontal-axis windmills were developed in northwestern Europe. These early machines, known as post mills, had four blades mounted on a central post. Over time, improved versions such as smock mills (Figure 1-3), Dutch mills and fan mills were created, particularly in the Netherlands and Denmark. Horizontal-axis windmills eventually became the dominant design in Europe and

North America for many centuries because they offered higher efficiency and better technical performances compared with vertical-axis windmills [1].

Wind turbines in the United States during the 19th century and up to the 1930 were primarily used for irrigation. They featured a large number of steel blades and held significant economic value due to their widespread use, with around 8 million units installed across the country (Figure 1-4).

Figure 1-3: Smock mill

Figure 1-4: 19th century USA mill

The first attempts to generate electricity from wind date back to the late 19th century, and they became increasingly common during the first half of the following century. While most of these early designs used a horizontal axis, in 1931 George Jean Marie Darrieus developed one of the most well-known and widely adopted types of vertical-axis wind turbines, a design that still carries his name today [3].

1.2. Wind Turbines Classification

Wind turbines can be classified according to several criteria, including rotor-axis orientation, the aerodynamic principle used to generate torque, rotor geometry, size, and application. Among these criteria, the most common and fundamental distinction is based on the orientation of the axis of rotation. According to this classification, wind turbines are generally divided into horizontal-axis wind turbines and vertical axis wind turbines. Horizontal axis wind turbines (HAWTs) have a rotor axis approximately parallel to the incoming wind direction, while vertical axis wind turbines (VAWTs) have a rotor axis perpendicular to the ground [4]. This distinction is widely used in literature because it strongly influences the aerodynamic behavior, mechanical layout, control requirements, and typical applications of the turbine.

Horizontal-axis wind turbines represent the dominant configuration in modern wind energy production. Their success is mainly due to their high aerodynamic efficiency, mature design, and suitability for large-scale electricity generation. In most commercial applications, HAWTs use two or three blades connected to a rotor mounted on a nacelle, which is positioned at the top of a tower. Since the rotor must face the incoming wind, these turbines usually require a yaw system to align the rotor with the wind direction. This configuration is particularly suitable for open-field and offshore wind farms, where wind direction and wind speed are more favorable and less disturbed.

Vertical-axis wind turbines differ from HAWTs because their rotor axis is verticalc. This configuration allows the turbine to accept wind from any horizontal direction, reducing or eliminating the need for a yaw mechanism [5]. For this reason, VAWTs are often considered interesting for small-scale applications, urban environments, complex terrain, and locations where the wind direction changes frequently. However, VAWTs generally present more complex unsteady aerodynamic behavior than HAWTs, especially because the blades experience large variations in angle of attack during each revolution [6].

Another important way to classify wind turbines is according to the aerodynamic force mainly responsible for torque generation. From this point of view, turbines can be divided into lift-based and drag-based machines [5]. Lift-based turbines generate torque mainly through aerodynamic lift, which acts on airfoil-shaped blades. This category includes modern HAWTs and Darrieus-type VAWTs. On the other hand, drag-based turbines generate torque mainly through the pressure difference produced by the wind acting on surfaces with different drag characteristics. The Savonius rotor is the most common example of a drag-based wind turbine. Drag-based turbines are usually simpler and can have good self-starting capability, but they generally operate at lower rotational speeds and lower efficiency than lift-based turbines [7].

Within the family of vertical-axis wind turbines, the most common configurations are the Savonius rotor, the Darrieus rotor and the H-Darrieus rotor. The Savonius turbine is a drag-driven machine characterized by a simple geometry and relatively high starting torque. The Darrieus turbine, instead, is a lift-driven machine that uses curved or straight airfoil-shaped blades to generate torque. The H-Darrieus configuration can be considered a straight-bladed version of the Darrieus concept, while helical rotors are designed to reduce torque fluctuations during rotation. Hybrid configurations combining Savonius and Darrieus rotors have also been proposed in order to combine the self-starting ability of drag-based rotors with the higher efficiency of lift-based rotors [8].

Wind turbines may also be characterized according to their size and application. Large-scale turbines are mainly used for grid-connected electricity production in onshore and offshore wind farms. Medium and small-scale turbines may be used for distributed generation, isolated systems, experimental research, water pumping, battery charging, or urban energy applications. In addition, turbines can be classified according to their control strategy, such as fixed-speed or variable-speed operation, and according to their power regulation method, such as stall control, pitch control, or active power control. These classifications are important because they affect the turbine performance, structural loading, generator selection, and overall energy production.

In summary, no single criterion is sufficient to fully describe a wind turbine. The distinction between horizontal and vertical-axis turbines describes the general rotor arrangement, while the distinction between lift- and drag-based turbines describes the physical mechanism responsible for torque production. For the present work, both classifications are relevant because the turbine analyzed belongs to the family of vertical-axis wind turbines and operates mainly as a lift-based Darrieus-type rotor. This classification provides the basis for the following sections, where horizontal-axis and vertical-axis wind turbines are discussed in more detail.

1.3. Horizontal Axis Wind Turbines

Horizontal-axis wind turbines are the dominant configuration in modern wind energy production and represent most installed wind turbines worldwide. A typical HAWT is composed of several main components, including the rotor blades, hub, nacelle, drivetrain, generator, yaw system, pitch system, and tower (Figure 1-5). The rotor blades extract energy from the wind and transfer the resulting aerodynamic loads to the hub, which is connected to the drivetrain. The nacelle, mounted at the top of the tower, generally houses the main mechanical and electrical components, such as the gearbox, generator, brake, and control systems. The tower supports the rotor–nacelle assembly at a suitable height, where wind speeds are generally higher and less affected by ground roughness. Since the rotor must face the incoming wind, the yaw system aligns the nacelle with the wind direction, while the pitch system adjusts the blade angle to regulate aerodynamic loads and power production [4].

Different generator technologies can be used for grid connection, including synchronous and asynchronous machines. Synchronous generators can allow direct-drive configurations, avoiding the need for a gearbox and reducing noise and mechanical complexity. However, direct-drive systems are usually larger and more expensive. For this reason, geared configurations with other generator types have historically been widely adopted, although modern wind turbine designs may use different drivetrain solutions depending on the application, power rating, and cost requirements.

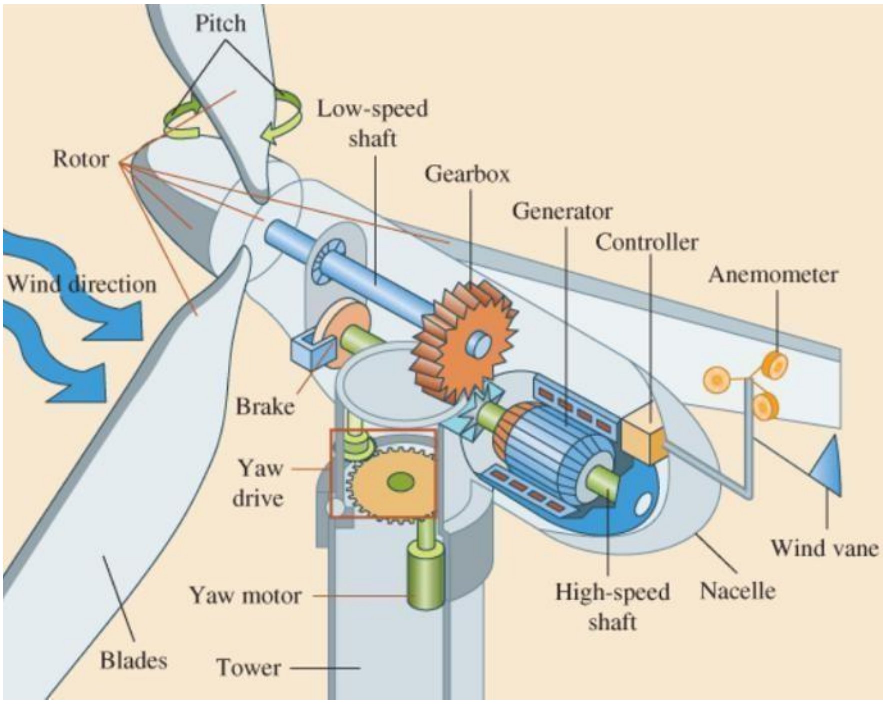

Figure 1-5: HAWT components

From an aerodynamic point of view, HAWTs are mainly lift-based machines. Their operating principle can be understood by comparison with an aircraft wing [9]. When an airfoil is exposed to a relative flow, a pressure difference is generated between its surfaces, producing a resultant aerodynamic force. This force can be decomposed into lift, acting perpendicular to the relative velocity, and drag, acting parallel to it. In wind turbines, the blades are constrained to rotate around the hub; therefore, the aerodynamic force produces torque around the rotor axis instead of translational motion. This torque causes the rotor to spin and enables the conversion of wind energy into mechanical power. A more detailed discussion of lift, drag, aerodynamic coefficients, and power extraction is provided in Chapter 2.

Although drag is also produced during operations, it does not represent the main useful contribution to power generation in HAWTs. On the contrary, drag generally opposes motion and contributes to aerodynamic losses. For this reason, the design of HAWT blades aims to maximize lift while minimizing drag, allowing the turbine to operate efficiently at relatively high tip-speed ratios.

A common classification of HAWTs is based on the position of the rotor with respect to the tower and the incoming wind direction [4]. HAWTs can be divided into upwind and downwind configurations. In upwind turbines, the rotor is placed in front of the tower, facing the incoming wind. This arrangement allows the airflow to reach the blades before interacting with the nacelle or tower, reducing disturbances and power losses. However, because the blades are located upstream of the tower, there is a risk of blade deflection towards the tower under strong aerodynamic loading. For this reason, upwind turbines require sufficient clearance between the rotor and the tower, as well as adequate blade stiffness and structural design. In addition, a yaw system is needed to keep the rotor aligned with the wind direction.

In downwind turbines, the rotor is located behind the tower. One advantage of this configuration is that the rotor can naturally align with the wind direction, reducing the need for an active yaw mechanism [10]. Moreover, blade deflection occurs away from the tower, which can reduce risk of tower strike and may allow more flexible blade designs. However, the airflow reaches the rotor after passing around the tower and nacelle, producing tower-shadow effects, unsteady loading, and increased fatigue on the blades. These disadvantages can reduce aerodynamic efficiency and contribute to structural vibrations. For this reason, upwind configurations are generally preferred in modern commercial wind turbines.

The most common and successful HAWT configuration today is the three-bladed upwind rotor. This design provides a good compromise between aerodynamic efficiency, structural balance, noise reduction, mechanical stability, and visual acceptance. High performance is achieved through carefully optimized blade geometry and the use of lightweight materials. These materials reduce rotor inertia and structural loads, allowing the turbine to respond more effectively to changes in wind speed while maintaining adequate strength and durability.

The main advantages of HAWTs are their high aerodynamic efficiency, technological maturity, and suitability for large-scale electricity generation. Their design has been extensively optimized, and their performance is well understood compared with other wind turbine architectures. However, they also present some limitations. The need for yaw alignment increases mechanical complexity, and the location of heavy components at the top of the tower can make installation and maintenance more difficult. In addition, their performance is sensitive to wind direction and inflow quality, making them less suitable for highly turbulent or rapidly changing wind environments.

Although HAWTs dominate the current wind energy market, other turbine configurations remain relevant for specific applications. In particular, vertical-axis wind turbines offer different characteristics, such as omnidirectional wind acceptance and the possibility of locating part of the drivetrain closer to the ground. These aspects make VAWTs relevant for small-scale systems, urban applications, and complex wind conditions. For this reason, the following section focuses on the main features and configurations of vertical-axis wind turbines.

1.4. Vertical Axis Wind Turbines

Vertical-axis wind turbines are characterized by a rotor axis arranged vertically, perpendicular to the ground. This configuration allows the rotor to accept wind from any horizontal direction without continuous alignment with the incoming flow. For this reason, VAWTs are often considered attractive for applications where the wind direction is variable, such as urban environments, complex terrain, and small-scale distributed generation systems. Unlike HAWTs, in which the blades generally experience a more uniform inflow during rotation, the blades of a VAWT pass through continuously changing flow conditions. During one revolution, the relative velocity and the angle of attack vary with the azimuthal position of the blade. As a consequence, VAWTs are associated with highly unsteady aerodynamic loads, torque fluctuations, and, in some operating conditions, dynamic stall [7].

Within the group of vertical-axis machines, several rotor concepts have been developed, differing mainly in blade geometry, structural arrangement, and method of torque generation. Early and simple designs, such as the Panemone and Savonius rotors, use surfaces or buckets that are pushed by the wind, while more advanced configurations, such as Darrieus-type turbines, use airfoil-shaped blades to produce torque more efficiently. Figure 1-6 presents several VAWT configurations, including Darrieus, Savonius, Solarwind™, helical, Noguchi, Maglev, and Cochrane concepts [1]. Among these, the Savonius and Darrieus rotors are the most established and widely discussed. The other configurations can be considered specialized variants, often developed to improve starting behavior, reduce torque fluctuations, or address specific mechanical and structural limitations. Among these configurations, the Savonius and Darrieus rotors remain the most established and widely discussed VAWT concepts, while the other designs can be considered specialized variants developed to address particular aerodynamic, mechanical, or structural limitations.

Drag-dominated VAWTs provide the simplest example of vertical-axis wind energy conversion and are useful as a contrast with lift-based rotors. The Panemone is an early drag-based vertical-axis wind machine. Its sails or panels generate torque when they are exposed broadside to the wind on the advancing side of the rotor. To reduce the negative torque produced on the returning side, the panels may be shielded from the wind or arranged so that they turn edge-on while moving against the wind. Although this mechanism improves the basic drag rotor concept, the Panemone remains relatively inefficient compared with modern lift-based turbines [11].

The Savonius rotor is the most representative drag-dominated VAWT in modern applications. It usually consists of two or more curved blades or semi-cylindrical buckets arranged around a vertical shaft. The advancing blade experiences a larger aerodynamic force than the returning blade, producing a net torque on the rotor. The main advantages of Savonius turbines are their simple construction, robustness, and good self-starting capability, even at relatively low wind speeds. However, their performance is limited by the negative torque generated by the returning blade and by the low rotational speeds typical of drag-dominated operation. Therefore, Savonius rotors are generally used when reliability, simplicity, and starting torque are more important than maximum efficiency [6].

In contrast with these drag-dominated machines, Darrieus-type VAWTs use airfoil-shaped blades and are designed to exploit aerodynamic lift. This allows them to operate at higher tip-speed ratios and to achieve higher power coefficients, making them more suitable for energy production. Within the Darrieus family, different rotor architectures have been proposed in order to improve structural behavior, manufacturability, and torque smoothness. The most common configurations include the H-shaped rotor, the V-shaped rotor, the classical Troposkien rotor, and the helical or Gorlov rotor, as shown in Figure 1-7.

The H-shaped Darrieus rotor, also known as the H-rotor or Giromill, uses straight vertical blades connected to the central shaft by horizontal support arms. This configuration is easier to manufacture than curved-bladed Darrieus rotors because the blades can have a constant airfoil section along the span. For this reason, H-shaped rotors are widely used in small-scale turbines, laboratory experiments, and numerical studies. However, the support arms introduce additional drag, and the straight blades are subjected to strong cyclic variations of angle of attack during rotation, which can lead to torque fluctuations and dynamic stall at low tip-speed ratios.

The V-shaped Darrieus rotor uses inclined blades connected to the central shaft, producing a tapered rotor geometry. This arrangement can be considered an intermediate solution between the straight-bladed H-rotor and the curved classical Darrieus rotor. The inclination of the blades modifies the distribution of aerodynamic and centrifugal loads along the span and may reduce some structural stresses. However, the geometry is more complex than the H-shaped rotor and is less common in practical applications.

The classical Darrieus rotor is often associated with the troposkien shape, which gives the turbine its characteristic “eggbeater” appearance. A troposkien curve corresponds approximately to the shape assumed by a flexible cable rotating around a vertical axis. This geometry is structurally advantageous because it allows centrifugal forces to be carried mainly in tension, reducing bending moments in the blades. Nevertheless, the curved blade shape is more difficult to manufacture than straight blades, and the turbine still presents typical Darrieus limitations such as poor self-starting capability, cyclic aerodynamic loading, and torque oscillations.

The Gorlov rotor is a helical development of the Darrieus concept. In this configuration, the blades are twisted around the vertical axis, so different blade sections operate at different azimuthal positions at the same time. This distributes the aerodynamic loading more uniformly over one revolution, reducing torque ripple, vibration, and cyclic loading. The main disadvantage is the increased manufacturing and structural complexity associated with the helical blade geometry [12].

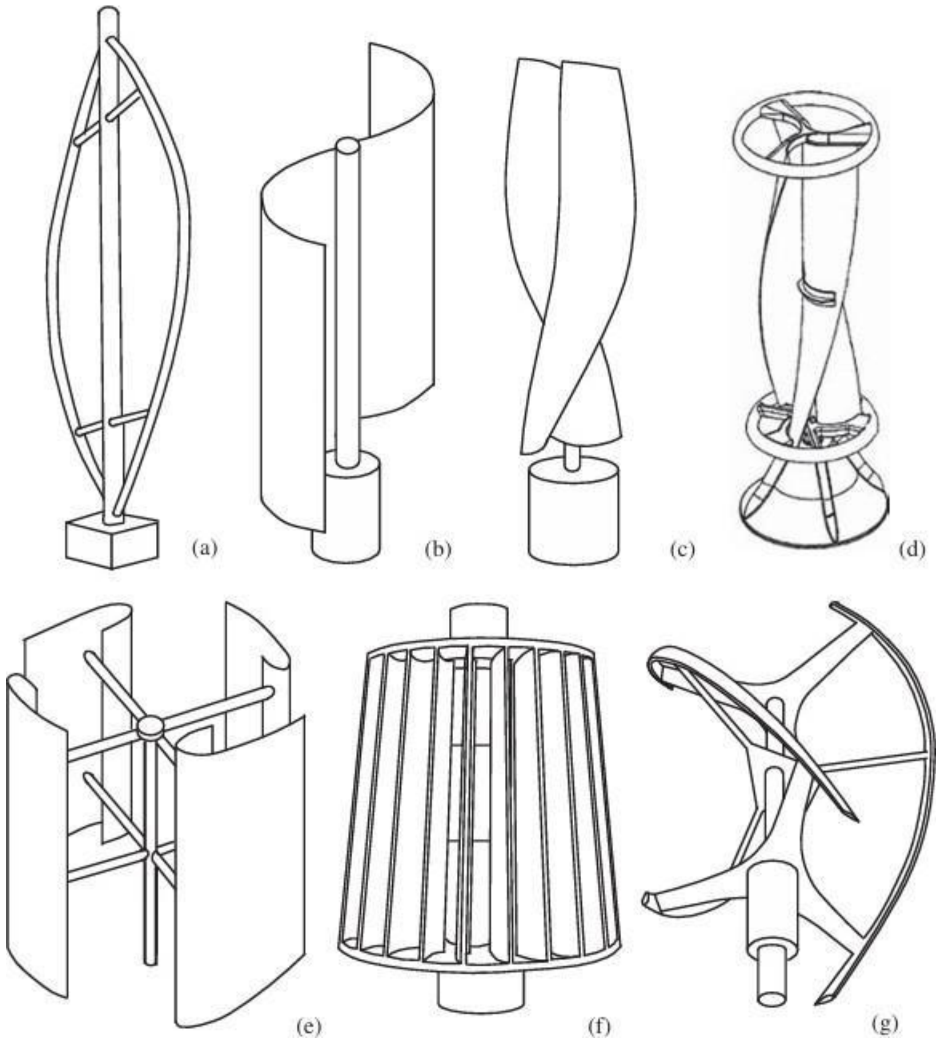

Figure 1-6: Several typical types of vertical-axis wind turbines: (a) Darrius; (b) Savonius; (c) Solarwind™;(d) Helical; (e) Noguchi; (f) Maglev; (g) Cochrane

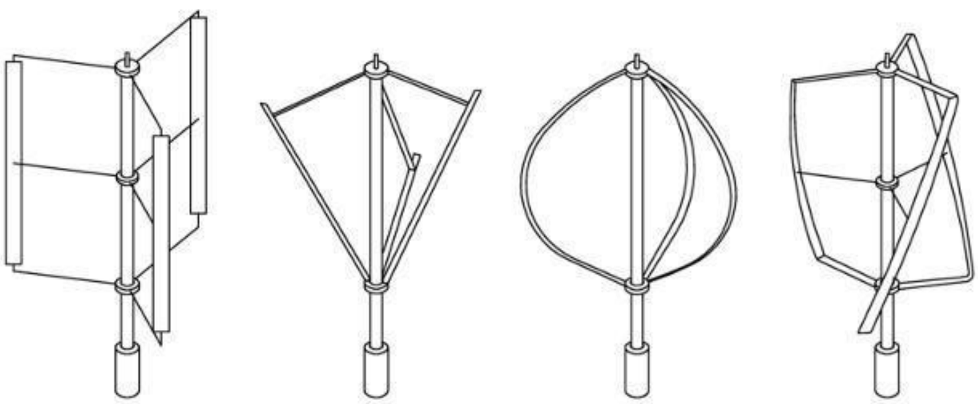

Figure 1-7: Various Darrieus rotor architectures. From left to right: H-Shaped, V-Shaped,Troposkien and Gorlov

Vertical-axis wind turbines present several characteristics that make them attractive for specific applications, especially in comparison with conventional horizontal-axis turbines. One of their main advantages is their ability to accept wind from any horizontal direction, which reduces or eliminates the need for a yaw mechanism. This characteristic is particularly useful in environments where the wind direction changes frequently, such as urban areas, complex terrain, or small-scale distributed generation sites. In addition, some VAWT configurations allow the generator and part of the drivetrain to be positioned closer to the ground, simplifying access for installation, inspection, and maintenance. Their compact geometry and potential suitability for turbulent or variable wind conditions have therefore encouraged their use in small-scale and experimental wind energy systems [6].

Despite these advantages, VAWTs also present important technical limitations. Their aerodynamic behavior is inherently unsteady because each blade experiences continuously changing relative velocity and angle of attack during rotation. As a result, the aerodynamic forces vary periodically with the azimuthal position of the blade, producing torque oscillations, cyclic loading, vibration, and fatigue stresses. These effects are especially relevant for lift-based VAWTs, such as Darrieus rotors, where the blade motion can lead to large variations in aerodynamic loading over a single revolution. In addition, supporting arms, struts, and the central shaft may introduce extra drag losses, reducing the effective efficiency of the rotor [13].

Another significant limitation of many Darrieus-type VAWTs is their poor self-starting capability. Since these turbines rely mainly on lift generation, they often require a minimum rotational speed before producing positive average torque. At low rotational speeds or low tip-speed ratios, the blades may experience very large angles of attack, leading to flow separation and dynamic stall. Although dynamic stall can temporarily increase the instantaneous aerodynamic forces, it also produces strong load fluctuations, torque ripple, and possible reductions in average performance. For this reason, some Darrieus turbines require external starting systems, variable-pitch mechanisms, or hybridization with drag-based rotors such as Savonius turbines.

Overall, VAWTs offer relevant advantages, including omnidirectional wind acceptance, simpler yaw requirements, possible ground-level drivetrain placement, and suitability for small-scale or complex-flow environments. However, their development is limited by unsteady aerodynamics, self-starting difficulties, torque fluctuations, fatigue loading, and generally lower commercial maturity compared with HAWTs. Among the different VAWT concepts, Darrieus-type turbines remain particularly important because they combine the advantages of vertical-axis operation with the higher efficiency of lift-based energy conversion. At the same time, their complex aerodynamic behavior makes them a challenging subject of study, especially under low-tip-speed-ratio conditions where dynamic stall becomes significant [7].

For the present thesis, these aspects are especially relevant because the performance of a Darrieus-type VAWT cannot be fully understood from steady aerodynamic considerations alone. The cyclic variation of angle of attack, the development of dynamic stall, and the resulting torque fluctuations must be considered in order to evaluate the rotor behavior accurately. This motivates the aerodynamic and performance analysis presented in the following chapter.

2 Aerodynamics and Performance Metrics

2.1. Basic Aerodynamics

2.1.1. Governing Flow Concepts

Wind turbine aerodynamics is governed by the interaction between the incoming airflow and the turbine blades. The wind can be described as a flow field characterized by velocity, pressure, density, and viscosity. Under normal operating conditions for wind turbines, the flow speed is much lower than the speed of sound; therefore, air is commonly treated as an incompressible fluid. In this assumption, density variations are neglected, and the flow is governed mainly by the conservation of mass and momentum [14].

The conservation of mass for an incompressible flow is expressed by the continuity equation:

$$\nabla \cdot \boldsymbol{u} = 0 \tag{2.1}$$

where u is the velocity vector. This equation states that fluid mass is conserved and that, for incompressible flow, the net volume flow rate entering and leaving a control volume must be balanced.

The conservation of momentum is described by the Navier–Stokes equations. For an incompressible Newtonian fluid with constant properties, they can be written as:

$$\rho \left(\frac{\partial \boldsymbol{u}}{\partial t} + \boldsymbol{u} \cdot \nabla \boldsymbol{u}\right) = -\nabla \boldsymbol{p} + \mu \nabla^2 \boldsymbol{u} + \boldsymbol{f} \tag{2.2}$$

where ρ is the air density, $\boldsymbol{p}$ is the pressure, μ is the dynamic viscosity, and $\boldsymbol{f}$ represents external body forces or momentum sources. The different terms in Equation (2.2) represent unsteady acceleration, convective acceleration, pressure forces, viscous diffusion, and external forces, respectively.

In wind turbine applications, these equations describe how the incoming flow is modified by the presence and motion of the blades. As air moves around a blade, the pressure field and viscous stresses on the blade surface generate aerodynamic forces.

These forces are responsible for torque production, structural loading, and wake formation. In vertical-axis wind turbines, the problem is particularly unsteady because each blade continuously changes its position with respect to the incoming wind. As a result, the local flow conditions around the blade vary during each revolution, producing time-dependent aerodynamic loads.

Although the full Navier–Stokes equations provide the theoretical basis for wind turbine aerodynamics, obtaining analytical solutions is generally not possible for practical turbine flows. For this reason, simplified analytical models, experimental measurements, and numerical methods such as computational fluid dynamics are commonly used to evaluate turbine performance. In the following sections, the basic aerodynamic quantities required for this analysis are introduced, starting from airfoil geometry, the relative flow experienced by the blade, and the resulting aerodynamic forces.

2.1.2. Airfoil Geometry

An airfoil is the two-dimensional cross-section of a blade, shaped to generate aerodynamic forces when exposed to a moving fluid. In wind turbines, the blade sections are shaped as airfoils in order to extract energy from the wind and convert it into mechanical rotation. The airfoil geometry affects the pressure distribution, boundary-layer development, stall behavior, and aerodynamic forces generated during operation.

The main geometric features of an airfoil are shown in Figure 2-1. The leading edge (LE) is the front point of the airfoil that first meets the incoming relative flow, while the trailing edge (TE) is the rear point where the flow leaves the airfoil. The straight line connecting the leading edge and the trailing edge is called the chord line, and its length is known as the chord length, usually denoted by c. The chord is one of the most important reference dimensions in airfoil analysis because it is used to define geometric parameters, Reynolds number, and aerodynamic force coefficients [15].

Another important geometric element is the camber line, also called the mean camber line. It is the curve located halfway between the upper and lower surfaces of the airfoil. The maximum distance between the camber line and the chord line is known as the maximum camber. If the camber line coincides with the chord line, the airfoil is symmetric. If the camber line is curved away from the chord line, the airfoil is cambered. Cambered airfoils generally produce lift even at zero geometric angle of attack, while symmetric airfoils produce no lift at zero angle of attack under ideal symmetric flow conditions [16].

The thickness distribution describes how the distance between the upper and lower surfaces varies along the chord. The maximum thickness is usually expressed as a percentage of the chord length. For example, an airfoil with a maximum thickness equal to 15% of the chord is described as having a relative thickness of $t/c = 0.15$. Thickness is important because it affects both aerodynamic and structural behavior. Thicker airfoils can provide greater structural stiffness, but they may also modify drag, separation, and stall characteristics.

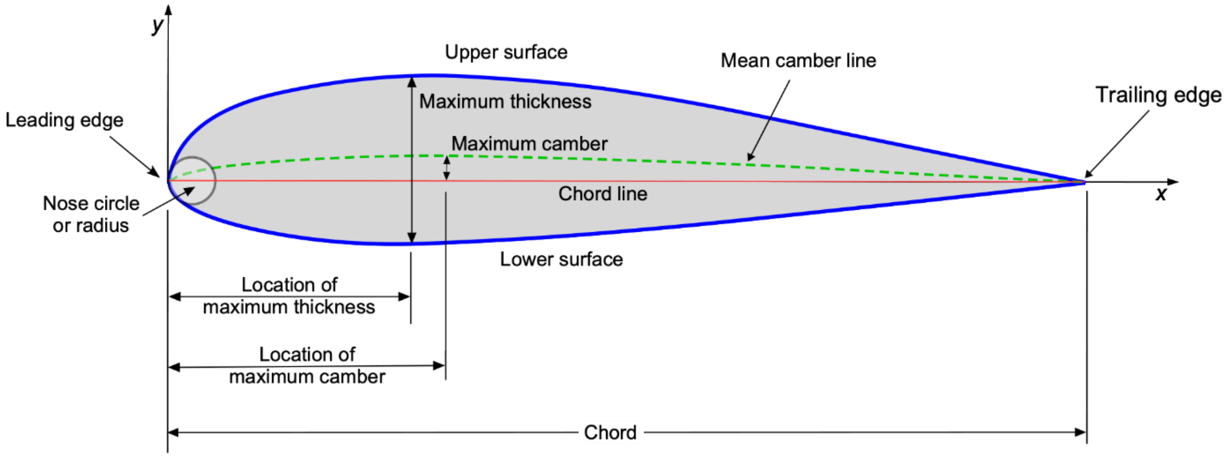

Figure 2-1: Airfoil geometry components

In vertical-axis wind turbines, airfoil selection is particularly important because the blades experience both positive and negative angles of attack during each revolution. For this reason, many Darrieus-type VAWTs use symmetric airfoils, such as profiles from the NACA 00-series. Symmetric airfoils provide similar aerodynamic behavior for positive and negative incidence angles, which is useful for rotors where the flow direction relative to the blade changes continuously. However, the final choice of airfoil also depends on Reynolds number, expected operating tip-speed ratio, structural requirements, and stall behavior [17].

The geometric characteristics of the airfoil therefore define the basic shape of the blade and strongly affect the aerodynamic response of the turbine. After defining the airfoil geometry, the next step is to describe the relative velocity experienced by a moving blade and the angle of attack, which determines how the incoming flow interacts with the airfoil.

2.1.3. Relative Velocity and Angle of Attack

In a vertical-axis wind turbine, the velocity experienced by each blade is the result of the vector combination between the free-stream wind velocity and the blade tangential velocity [10]. As shown in Figure 2-2, the direction and magnitude of the relative velocity vary with the azimuthal position of the blade. Consequently, the angle of attack is not constant during one revolution, but changes continuously as the blade moves around the rotor.

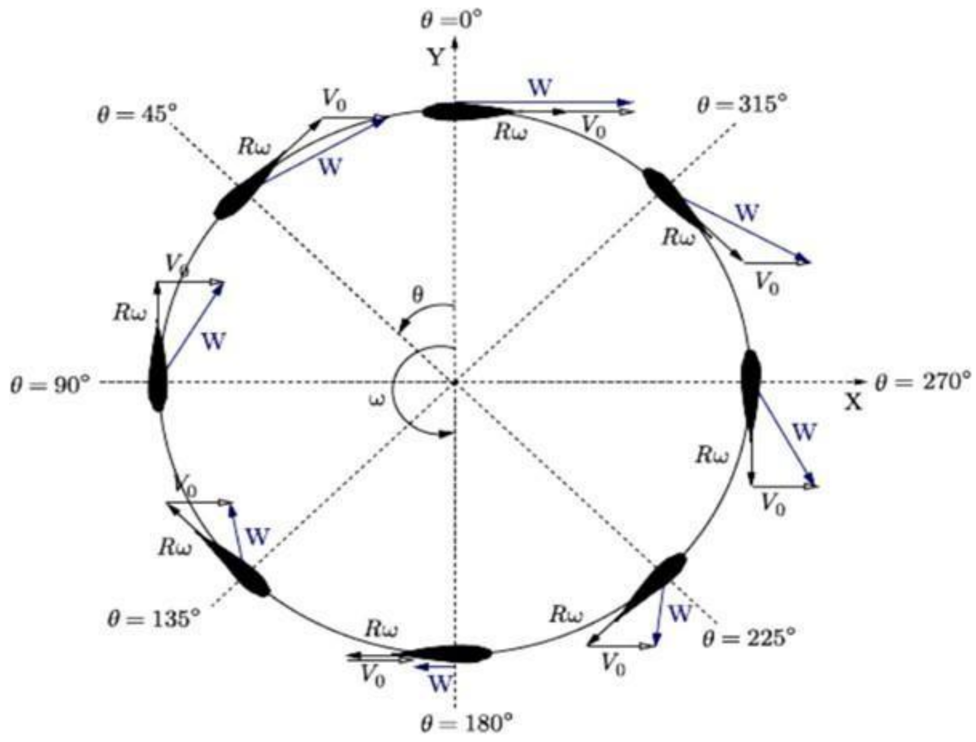

Figure 2-2: Variation of VAWT blade relative flow velocity and angle of attack over a revolution

This behavior is one of the main aerodynamic differences between HAWTs and VAWTs. In a HAWT, under uniform inflow, each blade section usually operates under relatively stable aerodynamic conditions. In contrast, in a Darrieus-type VAWT, the blade passes through upstream and downstream regions where the relative flow direction changes significantly. This produces cyclic variations in angle of attack, aerodynamic forces, and torque [18].

In Figure 2-2, V_0 represents the free-stream wind velocity, $R\omega$ is the blade tangential velocity, and W is the resulting relative velocity seen by the blade. The angle between the relative velocity W and the blade chord defines the instantaneous angle of attack. Since the blade position changes with the azimuthal angle θ, the direction of W also changes during rotation.

The variation of relative velocity and angle of attack in a VAWT is strongly influenced by the ratio between the blade tangential speed and the incoming wind speed. This ratio is known as the tip-speed ratio, usually denoted by λ. A high tip-speed ratio means that the blade rotational velocity is dominant compared with the free-stream wind velocity, leading to smaller variations in angle of attack. Conversely, at low tip-speed ratios, the incoming wind velocity has a stronger influence on the relative flow direction, causing larger angle-of-attack variations and increasing the likelihood of flow separation and dynamic stall [19]. The tip-speed ratio is formally defined and discussed as a performance parameter in Section 2.3.

2.1.4. Lift, Drag and Aerodynamic Force Generation

When an airfoil is exposed to a relative flow, the interaction between the fluid and the blade surface produces a resultant aerodynamic force. This force originates from two main contributions: the pressure distribution acting normal to the airfoil surface and the viscous shear stresses acting tangentially along the surface. The pressure field around the airfoil depends on its geometry, angle of attack, and flow conditions. As the flow accelerates and decelerates around the profile, pressure differences are generated between the two sides of the airfoil, producing a force that can be used for energy conversion.

The resultant aerodynamic force is commonly decomposed into two components with respect to the relative velocity. The component perpendicular to the relative velocity is called lift, while the component parallel to the relative velocity is called drag. Lift is the main useful force in lift-based wind turbines, because part of it can be converted into a tangential force that produces torque on the rotor. Drag, on the other hand, generally opposes the motion of the blade and contributes to aerodynamic losses, although it is always present in real flows because of pressure drag and viscous friction.

In wind turbines, the aerodynamic force must be considered in relation to the rotor motion. The component of the force acting in the tangential direction contributes directly to torque production, while the component acting normal or radial to the rotor path mainly contributes to structural loading. For this reason, even though lift and drag are defined relative to the incoming flow, turbine performance depends on how these forces are projected onto the rotor coordinate system. This distinction is particularly important for vertical-axis wind turbines, where the relative velocity direction changes continuously with the azimuthal position of the blade.

In Darrieus-type VAWTs, the blades generate torque mainly through lift. However, because the angle of attack varies during the revolution, the direction and magnitude of the aerodynamic force also change with time. This produces a periodic variation of the tangential force and therefore of the instantaneous torque. If the angle of attack becomes too large, the flow may separate from the blade surface, modifying the pressure distribution and reducing the effectiveness of lift generation [20]. This behavior leads naturally to the discussion of flow separation and stall.

2.1.5. Flow Separation and Stall

When an airfoil operates at small or moderate angles of attack, the flow generally remains attached to most of the blade surface. Under these conditions, the pressure distribution around the airfoil is relatively stable, and the aerodynamic force varies smoothly with the angle of attack. However, as the angle of attack increases, the flow over the suction side of the airfoil must move against an increasingly adverse pressure gradient. If the boundary layer does not have enough momentum to overcome this pressure increase, it detaches from the surface, as can be seen in Figure 2-3. This phenomenon is known as flow separation.

Flow separation modifies the pressure distribution around the airfoil and reduces the effectiveness of lift generation. When separation becomes sufficiently large, the airfoil reaches stall. Stall is generally associated with a strong reduction in lift, an increase in drag, and a significant change in the aerodynamic force direction. In wind turbines, stall can reduce the useful tangential force available for torque production and can increase unsteady loads on the blades.

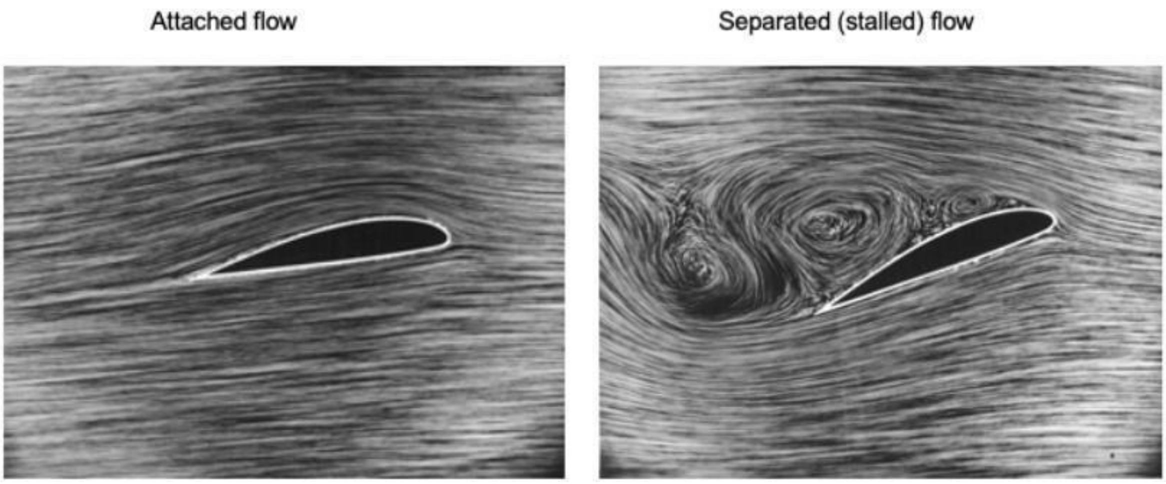

Figure 2-3: Flow-visualization images show smooth streamlines typical of attached flow (left image) and detached or separated flow and turbulence characteristic of stall onset (right image)

The angle at which stall occurs depends on several factors, including the airfoil geometry, surface roughness, Reynolds number, turbulence level, and the rate at which the angle of attack changes. For a stationary airfoil under steady flow conditions, stall is usually described as a static phenomenon. However, in rotating machines, especially vertical-axis wind turbines, the angle of attack may vary rapidly during operation. In these cases, the stall process becomes unsteady and cannot be fully described by static airfoil behavior alone [16].

For Darrieus-type VAWTs, stall is especially important because the blades experience large cyclic variations in angle of attack during each revolution. At low tip-speed ratios, these variations become larger, increasing the probability of flow separation over part of the rotation. This can produce large fluctuations in aerodynamic forces, torque, and structural loading. Therefore, understanding flow separation and stall is essential before introducing dynamic stall and its effects on VAWT performance.

2.1.6. Dynamic Stall

Dynamic stall is an unsteady aerodynamic phenomenon that occurs when the angle of attack changes rapidly and the flow separation process is delayed compared with the corresponding static stall condition. During dynamic stall, the airfoil can temporarily sustain lift beyond the static stall angle. This is often followed by the formation and convection of a leading-edge vortex, a sudden change in aerodynamic loads, and eventually a drop in lift as the separated flow develops [21].

In Darrieus-type VAWTs, dynamic stall is commonly observed at low tip-speed ratios because the blades undergo large and rapid changes in angle of attack. Although dynamic stall may temporarily increase the instantaneous aerodynamic force, it also produces strong load fluctuations and torque oscillations. For this reason, it is one of the key phenomena that must be considered when analyzing the performance of VAWTs operating in unsteady conditions.

2.2. Aerodynamic Coefficients

The aerodynamic forces acting on an airfoil depend on several dimensional quantities, including air density, relative velocity, chord length, blade span, and angle of attack. For this reason, aerodynamic performance is commonly described using non-dimensional coefficients. These coefficients allow different airfoils, operating conditions, and experimental or numerical results to be compared independently of the specific size or flow velocity used in the analysis.

2.2.1. Lift, Drag and Moment Coefficients

The lift coefficient (2.3) describes the ability of the airfoil to generate force perpendicular to the relative flow, while the drag coefficient (2.4) describes the resistance parallel to the flow. The moment coefficient (2.5) represents the pitching tendency of the aerodynamic force around a reference point, usually the quarter-chord or aerodynamic center.

$$C_L = \frac{L}{\frac{1}{2}\rho A W^2} \tag{2.3}$$

$$C_D = \frac{D}{\frac{1}{2}\rho A W^2} \tag{2.4}$$

$$C_M = \frac{M}{\frac{1}{2}\rho A W^2 c} \tag{2.5}$$

Airfoil aerodynamic coefficients are commonly represented through polar curves, which describe the variation of lift, drag, and moment coefficients with angle of attack. In the attached-flow region, the lift coefficient usually increases almost linearly with angle of attack, while the drag coefficient remains relatively low. As the angle of attack approaches stall, flow separation modifies the pressure distribution, causing the lift coefficient to decrease or level off and the drag coefficient to increase significantly. These polar curves are essential in blade-element and actuator-line models because they provide the local aerodynamic response of the blade section.

The aerodynamic coefficients of an airfoil depend not only on the angle of attack, but also on the Reynolds number. The Reynolds number is a non-dimensional parameter that expresses the ratio between inertial and viscous effects in the flow. For an airfoil section, it is commonly defined as:

$$Re = \frac{\rho W c}{\mu} \tag{2.6}$$

where W is the relative velocity experienced by the blade section, c is the airfoil chord, ρ is the air density and μ is the dynamic viscosity.

Reynolds number influences the development of the boundary layer, the transition from laminar to turbulent flow, flow separation, and stall behavior. As a consequence, the lift, drag, and moment coefficients of an airfoil may change significantly with Reynolds number, especially at low Reynolds numbers. This is particularly important for small-scale wind turbines and Darrieus-type VAWTs, where the operating Reynolds number can be much lower than that of large commercial HAWTs.

2.2.2. Normal and Tangential Force Coefficients

Although lift and drag coefficients are useful for describing the aerodynamic behavior of an airfoil, they are not always the most convenient quantities for wind turbine analysis. Lift and drag are defined with respect to the relative velocity W: lift acts perpendicular to W, while drag acts parallel to W. However, for a rotating turbine blade, the most important force directions are usually the tangential direction, which produces torque, and the normal direction, which mainly contributes to structural loading [22].

For this reason, the aerodynamic force acting on a blade section can be expressed either in the lift–drag reference frame or in the normal–tangential reference frame. The two descriptions represent the same physical force but decomposed along different directions. The lift and drag coefficients are linked to the airfoil behavior, while the normal and tangential coefficients are more directly related to rotor performance.

The tangential force component is especially important because it is responsible for producing torque on the rotor. If the tangential force acts in the direction of rotation, it contributes positively to power generation. If it acts against the rotation, it produces negative torque. The normal force component, instead, does not directly contribute to power production, but it affects the structural loads acting on the blades, support arms, and shaft.

The corresponding sectional coefficients can be written as:

$$C_t = \frac{F_t}{\frac{1}{2}\rho A W^2} \tag{2.7}$$

$$C_n = \frac{F_n}{\frac{1}{2}\rho A W^2} \tag{2.8}$$

2.3. Power and Performance Metrics

The performance of a wind turbine is evaluated by comparing the mechanical power extracted by the rotor with the kinetic power available in the incoming wind. For a uniform free-stream velocity U_∞, the available wind power passing through the rotor swept area is:

$$P_{wind} = \frac{1}{2}\rho A U_\infty^3 \tag{2.9}$$

where ρ is the air density, A is the rotor swept area, and U_∞ is the free-stream wind velocity. This expression shows that the available power varies with the cube of the speed of the wind, meaning that small changes in wind velocity can produce large changes in the energy available to the turbine. For a straight-bladed vertical-axis wind turbine, the swept area is usually defined as:

$$A = 2RH \tag{2.10}$$

where R is the rotor radius, and H is the rotor height.

The aerodynamic forces acting on the blades generate a torque around the rotor axis. The useful force component for energy extraction is the tangential component, since it acts in the direction of rotation. The mechanical power produced by the rotor is given by:

$$P = T\omega \tag{2.11}$$

where T is the rotor torque and ω is the angular velocity. In vertical-axis wind turbines, the tangential force changes with the azimuthal position of the blade, causing the instantaneous torque and power to fluctuate during each revolution. For this reason, turbine performance is usually evaluated using averaged torque and power values over one or more complete rotations.

The most common non-dimensional performance parameter is the power coefficient, defined as:

$$C_P = \frac{P}{\frac{1}{2}\rho A U_\infty^3} \tag{2.12}$$

The power coefficient represents the fraction of the available wind power that is converted into mechanical power by the rotor. Since it is non-dimensional, it allows comparison between turbines of different sizes and operating conditions. In VAWTs, the instantaneous value of C_P may vary significantly during rotation, so the mean power coefficient is commonly used to describe the overall performance of the turbine.

Another useful performance parameter is the torque coefficient:

$$C_T = \frac{T}{\frac{1}{2}\rho A U_\infty^3 R} \tag{2.13}$$

where R is the rotor radius. While C_P describes the global energy conversion efficiency, C_T describes the non-dimensional torque production of the rotor. This is especially useful for VAWTs because torque can be analyzed as an instantaneous quantity over the azimuthal position or as an average value over a full revolution.

The connection between torque and power depends on the rotor angular velocity. For this reason, another fundamental performance parameter is the tip speed ratio, defined as:

$$\lambda = \frac{\omega R}{U_\infty} \tag{2.14}$$

where ωR is the blade tip speed and U_∞ is the free-stream wind velocity. The tip speed ratio indicates how fast the blade tip moves compared with the incoming wind. Therefore, it controls the relative importance of rotational motion and free stream velocity in determining the flow seen by the blade. In Darrieus-type VAWTs, this is especially important because λ strongly affects the relative velocity, the AoA variation, the tangential force, and consequently the torque generated by the rotor.

The power coefficient can be related directly to the torque coefficient by combining the definitions of C_P, C_T, and λ:

$$C_P = \lambda C_T \tag{2.15}$$

This relation shows that the power coefficient depends not only on the torque produced by the rotor, but also on the rotational speed at which that torque is generated. A turbine may produce high torque at low rotational speed, but this does not necessarily correspond to maximum power. For this reason, wind turbine performance is usually evaluated through the variation of C_P with tip-speed ratio.

For Darrieus-type VAWTs, the tip-speed ratio is also closely related to the aerodynamic regime. At low λ, the incoming wind has a strong influence on the relative flow direction, producing large angle-of-attack variations and increasing the probability of flow separation and dynamic stall. At higher λ, the blade tangential speed becomes dominant, the angle-of-attack variation is reduced, and the aerodynamic loading becomes smoother. However, excessively high tip-speed ratios may reduce the useful tangential force or increase losses. Therefore, the optimal operating point is generally identified by the maximum value of the C_P-λ curve [19].

2.4. Betz and Newman's Limit

The Betz limit is derived using the actuator disk model, schematically shown in Figure 2-4. In this idealized representation, the wind turbine is replaced by a permeable disk of area A, which extracts energy from the incoming flow without explicitly modeling the individual blades. The air that passes through the rotor is represented by a streamtube. Far upstream, the flow enters the streamtube with velocity $v_{in}$and area A_{in}. At the rotor plane, the flow velocity decreases to v_c, while farther downstream it reaches v_{out}. Since the flow is assumed incompressible, the reduction in velocity must be accompanied by an expansion of the streamtube area.

In Figure 2-4, the actuator disk produces a pressure discontinuity across the rotor plane. The pressure increases just upstream of the disk and decreases just downstream, allowing the turbine to extract mechanical power from the flow. However, the flow cannot be brought completely to rest behind the rotor, because in that case no additional air would pass through the turbine. Therefore, the maximum power is obtained by slowing the flow by an optimal amount rather than stopping it completely [23].

The axial induction factor a is introduced to quantify the velocity reduction between the free stream and the actuator disk:

$$a = \frac{U_{in} - U_c}{U_{in}} \tag{2.16}$$

The corresponding power coefficient is:

$$C_P = 4a(1-a)^2 \tag{2.17}$$

Maximizing this expression gives $a = 1/3$, and therefore:

$$C_{P,max} = \frac{16}{27} \approx 0.593$$

This value is known as the Betz limit and represents the maximum theoretical power coefficient of an ideal single actuator disk.

Although the actuator disk model in Figure 2-4 provides the basis for the Betz limit, it represents the turbine as a single disk. This approach is well suited as a general idealization, but it does not fully represent the way a vertical-axis wind turbine interacts with the flow. In a Darrieus-type VAWT, the upstream and downstream halves of the rotor both interact with the incoming flow. Newman extended the actuator disk concept to a tandem disk model, which is more representative of crossflow turbines such as VAWTs. This leads to a theoretical maximum power coefficient of:

$$C_{P,max} = \frac{16}{25} \approx 0.64$$

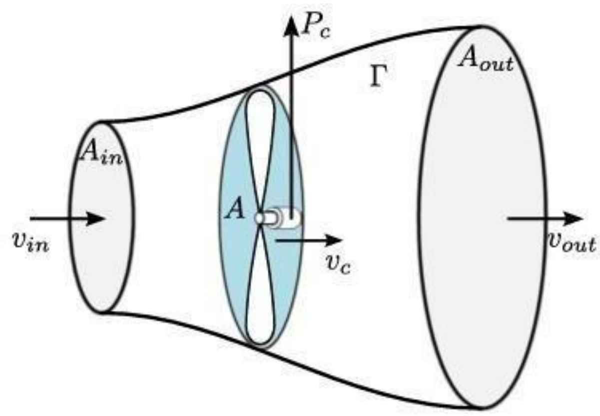

Figure 2-4: Actuator disk model of a wind turbine

3 Geometric Characterization

This chapter presents the geometric characterization of the blade profile used for the numerical simulations. Since the turbine was already available as a physical model, a reverse engineering approach was adopted to reconstruct the blade cross-section from the existing geometry and convert the real blade shape into a simplified two-dimensional profile suitable for numerical implementation in OpenFOAM. The reconstructed profile is then compared with standard airfoil geometries in order to evaluate whether the physical blade corresponds to a known profile or presents similarities with one of them.

3.1. Geometry Reconstruction

The turbine considered in this thesis is a hybrid Savonius-Darrieus VAWT, shown in Figure 3-1. However, due to the complexity of reconstructing the complete hybrid geometry in OpenFOAM, the present work focuses only on the Darrieus rotor. Consequently, the reverse engineering procedure and the subsequent numerical analysis are limited to the Darrieus blade geometry, as shown in Figure 3-2.

Figure 3-1: Original Savonius-Darrieus VAWT

Figure 3-2: VAWT with Darrieus component only considered for this project

The reverse engineering procedure started with the three-dimensional scanning of one Darrieus blade. The scan was performed in order to obtain a digital representation of the real blade shape, preserving the main geometric features of the physical component. Since the numerical model requires an accurate description of the blade cross-section, the scanned geometry was used as the starting point for the extraction of the two-dimensional profile. However, as commonly occurs in scanned geometries, the raw model contained local irregularities, surface noise, and small imperfections associated with the acquisition process. Therefore, the scan was refined before being imported into Autodesk Inventor. The refined scanned geometry is shown in Figure 3-3. Subsequently, the blade was divided into six cross-sections perpendicular to its longitudinal direction, as shown in Figure 3-4. Each section was extracted and compared with the others to evaluate the dimensional consistency of the blade along its span. Since no significant dimensional differences were observed among the extracted sections, one representative cross-section was selected for the subsequent geometric analysis (Figure 3-5).

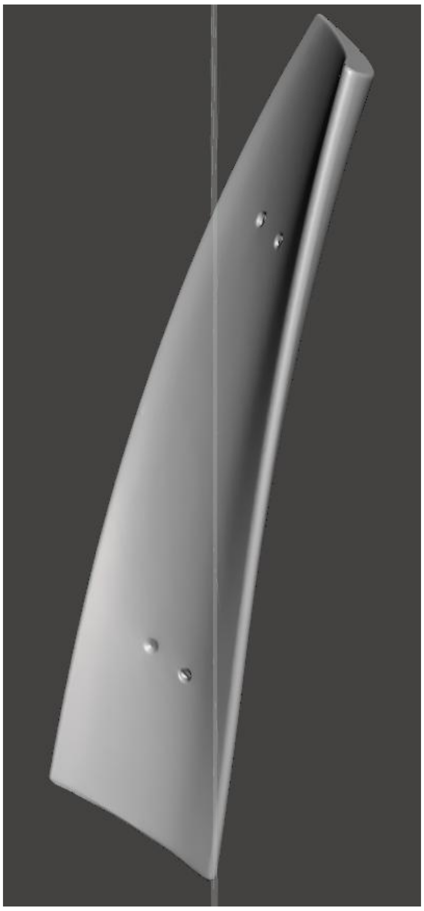

Figure 3-3: Scan of Darrieus blade

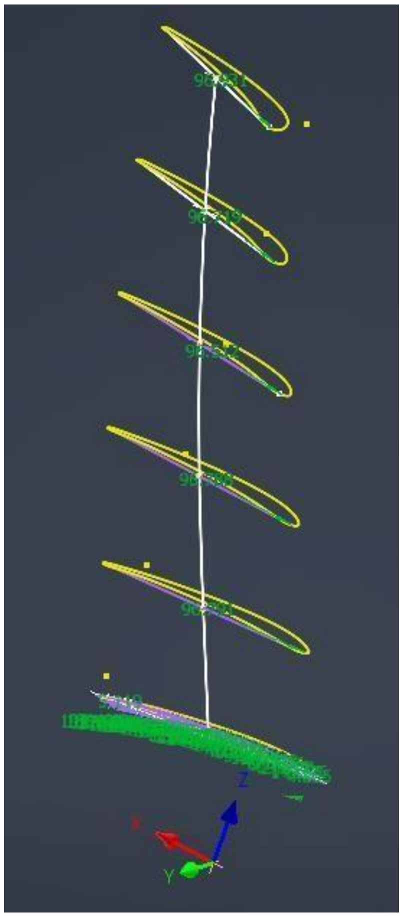

Figure 3-4: Cross sections of the blade

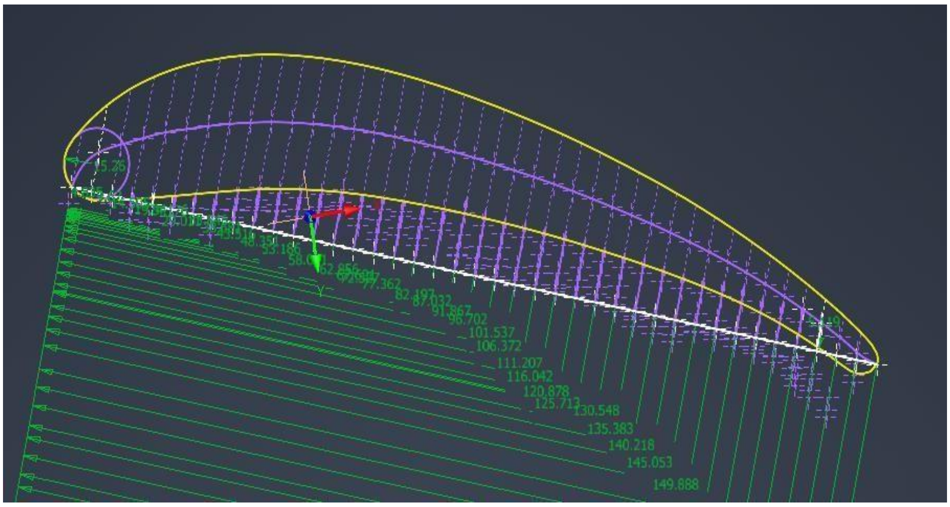

Figure 3-5: Representative cross-section showing the chord line (white), camber line, and leading-edge radius (purple)

3.2. Geometric Results

The reconstructed blade section presents the main characteristics of a cambered airfoil. The profile is defined by a rounded LE and TE. The rounded LE allows the incoming flow to approach the profile more gradually, while the rounded TE indicates that the section does not close into a sharp conventional airfoil geometry.

The measured chord length of the representative section is equal to 193.5 mm. The maximum thickness-to-chord ratio is 15.27% with the maximum thickness located at approximately 35% of the chord from the LE. This suggests that the profile is relatively thick, with the largest thickness positioned in the forward part of the airfoil.

The profile also shows a significant camber. The maximum camber is equal to 13.1% of the chord and is located at approximately 38% of the chord from the LE. This value indicates that the profile is not symmetric but instead presents a marked curvature of the mean camber line.

Another important geometric feature is the LE radius, measured at 15.26 mm. The value confirms the presence of a relatively rounded front section, which is consistent with the visual appearance of the reconstructed profile. In addition, the blade exhibits an overall geometric twist of 70° along its span, showing that the blade section changes its orientation from one end to the other.

The main geometric parameters measured for this representative section are summarized in Table 1.

Chord length (mm)	193.5	
t/c % max	15.27	At 35% c
Camber/c % max	13.1	At 38% c

LE radius (mm)	15.26	
Airfoil twist (°)	70	

Table 1: Important dimensions of the airfoil

Overall, the reconstructed geometry can be described as thick, highly cambered, and twisted blade airfoil with both rounded LE and TE. These characteristics show that the blade does not correspond to a conventional symmetric airfoil typically used in many Darrieus rotor configurations. Instead, the reconstructed section presents a more complex geometry, which must be directly characterized before being implemented in the numerical model.

3.3. Comparison with Closest Standard Airfoil

A comparison with standard airfoil geometries showed that the reconstructed blade section does not correspond to a standard NACA profile. In order to identify whether a similar reference geometry existed, the reconstructed profile was compared with the airfoils available in the Airfoil Tools database [24]. Among the profiles considered, the closest standard geometry was found to be the USA 32 airfoil. According to Airfoil Tools, this profile has a maximum thickness of 14.7% located at 19.8% of the chord and a maximum camber of 9.3% located at 39.8% of the chord.

Although the maximum thickness of the USA 32 airfoil is relatively close to that of the reconstructed blade, the position of the maximum thickness is significantly different. In the reconstructed profile, the maximum thickness is located at 35% of the chord, whereas in the USA 32 airfoil it is located much closer to the leading edge, at 19.8% of the chord. Moreover, the reconstructed blade presents a higher maximum camber, equal to 13.1% of the chord, compared with 9.3% for the USA 32 airfoil. These differences indicate that the two profiles have different thickness and camber distributions, even if some global parameters appear partially similar.

For this reason, the USA 32 airfoil (Figure 3-6) cannot be considered a reliable substitute for the real blade geometry. Using the aerodynamic coefficients of the USA 32 profile would introduce an additional approximation that may not correctly represent the aerodynamic behavior of the turbine blade. Therefore, the reconstructed profile was retained as the reference geometry for the numerical model, while the comparison with the USA 32 airfoil was used only to highlight the geometric differences between the real blade and available standard profiles.

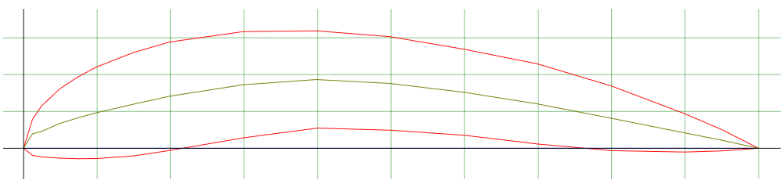

Figure 3-6: USA 32 airfoil

4 2D CFD Airfoil Simulation

The aim of this chapter is to present the numerical methodology adopted to analyze the aerodynamic behavior of the reconstructed blade profile in two dimensions. As discussed in Chapter 3, the blade section was obtained through a reverse engineering process, since the available rotor was a physical model and no original aerodynamic data were available. Therefore, a dedicated two-dimensional CFD analysis was necessary in order to obtain the aerodynamic coefficients of the reconstructed airfoil.

The lift and drag coefficients obtained from these simulations are required as input data for the actuator line model used in Chapter 5. In this modelling approach, the blade is represented through actuator points or lines, and the aerodynamic forces are computed from tabulated airfoil data as a function of the local angle of attack and relative velocity. For this reason, reliable C_L and C_D curves are necessary to correctly estimate the forces generated by the blade during the rotation.

The simulations were performed over a range of angle of attack representative of the operating conditions experienced by the blade. This is particularly important for VAWTs, since the relative velocity and the angle of attack vary continuously during each revolution. As a consequence, the aerodynamic response of the blade must be known over a wide angular range rather than at a single operating condition.

The numerical analysis was carried out using OpenFOAM, considering incompressible turbulent flow around the airfoil. The governing flow concepts introduced in Chapter 2 provide the theoretical basis for the simulation, while the present chapter focuses on the numerical setup, including the computational domain, mesh generation, boundary conditions, solver settings, turbulence models, and case matrix. The final objective is therefore to generate an aerodynamic database of lift and drag coefficients suitable for the actuator line model employed in turbine simulations.

4.1. Mesh and Boundary Conditions

4.1.1. Mesh Generation Strategy

Mesh generation is one of the most important steps in a CFD simulation, since the numerical solution is obtained by solving the governing equations over the discretized computational domain. The quality of the mesh directly affects the accuracy, stability and convergence of the simulation. Poorly generated grids can introduce high discretization errors, produce non-physical gradients, and in some cases prevent the solver from reaching convergence. For this reason, particular attention was given to the mesh generation process adopted for the two-dimensional simulations of the reconstructed airfoil.

Before generating the mesh, the blade profile reconstructed in Autodesk Inventor was imported into FreeCAD in order to create a B-spline representation of the airfoil geometry. A B-spline is a mathematical curve commonly used in computer-aided designs to represent smooth geometries by means of control points. This step was necessary because the blade profile was obtained through a reverse engineering procedure and therefore consisted initially of discrete coordinate points. Directly using these points for mesh generation could lead to irregularities along the surface, especially in regions where the curvature changes rapidly. By constructing the airfoil as a smooth spline, the surface definition becomes more suitable for mesh generation and allows a more regular distribution of mesh points along the airfoil boundary.

The mesh was generated using Pointwise, which allows the construction of structured grids around complex aerodynamic geometries. A structured mesh was preferred because it provides a high degree of control over the cell distribution, especially in the near-wall region. For airfoil simulation, the near-wall mesh must be sufficiently refined to resolve the boundary layer and to correctly evaluate lift and drag coefficients. In addition, structured grids generally provide smoother cell transition and better alignment with the expected flow direction compared with fully unstructured grids.

The mesh generation strategy was defined by considering both the geometry of the reconstructed airfoil and the expected flow behavior around it. In external aerodynamic simulations, the regions requiring the highest mesh resolution are generally the LE, the airfoil surface, the TE and the wake region. These are the zones where the largest gradients of velocity, pressure and turbulence quantities are expected. Mesh refinement is a compromise between accuracy and computational cost, with the highest resolution concentrated in the most relevant aerodynamic regions rather than uniformly applied to the whole domain [9].

4.1.2. Mesh Quality Criteria

Before selecting the mesh topology, the main mesh quality parameters were considered, such as non-orthogonality, skewness, aspect ratio and smoothness. (Figure 4-1)

Non orthogonality measures the deviation between the face-normal direction and the line connecting the centroids of two adjacent cells. A low value of non-orthogonality is desirable because finite volume discretization is more accurate when fluxes are evaluated across nearly orthogonal cell faces.

Skewness describes how much a cell deviates from an ideal regular shape. For a quadrilateral cell, the ideal configuration corresponds to angles close to 90°. Highly skewed cells, especially those with very acute angles, can negatively affect the interpolation of flow variables and may lead to convergence problems. This parameter was particularly important in the present work because the preliminary C-type grid generated highly skewed cells near the blunt trailing edge.

The aspect ratio is defined as the ratio between the largest and the smallest cell dimensions. In general, values close to one are preferable. However, high aspect ratio cells are acceptable and often necessary inside the boundary layer, where the cells are intentionally stretched along the airfoil surface and made very thin in the wall-normal direction. This allows the steep velocity gradient near the wall to be resolved while keeping a reasonable number of cells.

Another important requirement is mesh smoothness. This refers to the gradual variation of cells size between neighboring cells. Sudden jumps in cell dimensions should be avoided because they can introduce numerical errors and reduce the stability of the solution. Therefore, the cell size was increased progressively from the refined near-wall region toward the outer domain.

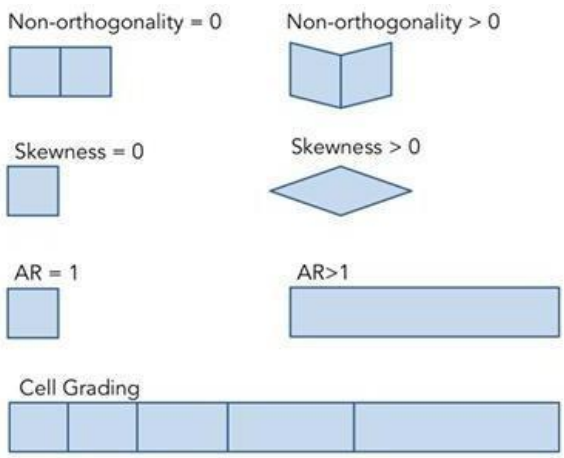

Figure 4-1:Skewness; Aspect Ratio; Smoothness

4.1.3. Choice of Mesh Topology

After defining the main mesh quality parameters, two different structured grid arrangements were tested in Pointwise: a C-type grid and an O-type grid. The purpose of this comparison was to identify the topology that could provide the best cell quality around the reconstructed airfoil, with particular attention to the leading edge, trailing edge and near-wall region.

The first attempt was based on a C-type grid, shown in Figure 4-2. This type of mesh is commonly used in airfoil simulations because it allows the grid to be refined around the airfoil and extended downstream in the wake direction. This arrangement is commonly advantageous because the cells behind the trailing edge can be aligned with the expected flow direction, improving the resolution of the wake region. Moreover, a C-type topology usually provides good control of the mesh distribution along the airfoil surface and in the downstream region.

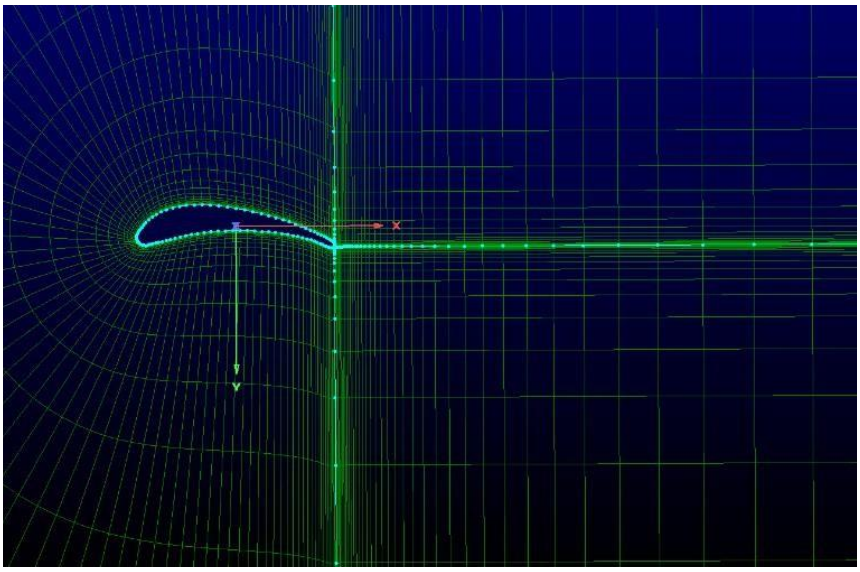

Figure 4-2:C-grid

However, in the present case, the C-type grid showed important limitations in the trailing-edge region. The reconstructed airfoil does not present a sharp trailing edge; instead, it has a blunt edge with a finite thickness. As a consequence, the mesh lines were forced to adapt to a geometrically abrupt region, where the upper and lower surfaces are connected by a short nearly vertical segment. This produced strongly distorted cells near the trailing edge, with poor skewness and smoothness, as shown in Figure 4-3. Since this region is aerodynamically relevant, the local mesh distortion could affect the evaluation of pressure gradients, wake formation and the resulting aerodynamic coefficients. In a finite volume method, strongly skewed cells reduce the accuracy of the interpolation between neighboring cell centers and of the flux evaluation across cell faces. For this reason, although the C-type grid was initially attractive for wake alignment, it was not selected as the final mesh.

To overcome these problems, an O-type grid was generated. In this topology, the mesh lines surround the airfoil forming closed curves around the profile. The O-grid was constructed by first generating a structured boundary-layer block around the airfoil surface. This block was then expanded outward in a circular manner, creating concentric layers of increasing cell size. The final result is shown in Figure 4-4

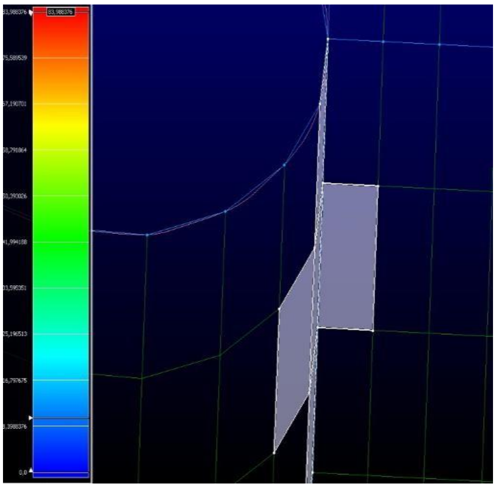

Figure 4-3: Skewness problem at trailing edge

The O-type grid provided a more regular cell distribution around the entire airfoil. In particular, the cell quality near the sharp trailing edge improved significantly compared with the C-grid. Since the mesh lines wrap around the profile instead of reconnecting abruptly downstream of the trailing edge, the formation of highly skewed cells was reduced. This improved the smoothness of the mesh and avoided the negative cell-quality issues observed in the preliminary C-grid.

Another advantage of the O-type grid is that it gives a more uniform refinement around both sides of the airfoil. This is important for the present work because the reconstructed profile is later used for a vertical-axis wind turbine application. During turbine rotation, the blade can experience a wide range of angles of attack, and both sides of the profile may become aerodynamically relevant. Therefore, it is useful to have a mesh that treats the pressure and suction sides with similar quality.

The main disadvantage of an O-grid is that it is not naturally aligned with the wake as well as a C-grid. Since the mesh lines close around the airfoil, the downstream region may not follow the wake direction as directly. However, in the present study, the priority was to obtain accurate and stable aerodynamic coefficients from the airfoil surface. Therefore, the quality of the near-wall region and the trailing edge was considered more important than the perfect alignment of the far wake. For this reason, the O-type grid was selected as the final topology.

Overall, the comparison between the two grids showed that the final O-type grid provided a better compromise between mesh quality, near-wall resolution and numerical stability. The C-type grid was useful as a preliminary attempt, but it generated excessive skewness near the trailing edge. The O-type grid avoided this issue and allowed a smoother transition from the boundary-layer region to the outer domain. Therefore, it was adopted for all the two-dimensional CFD simulations presented in this chapter.

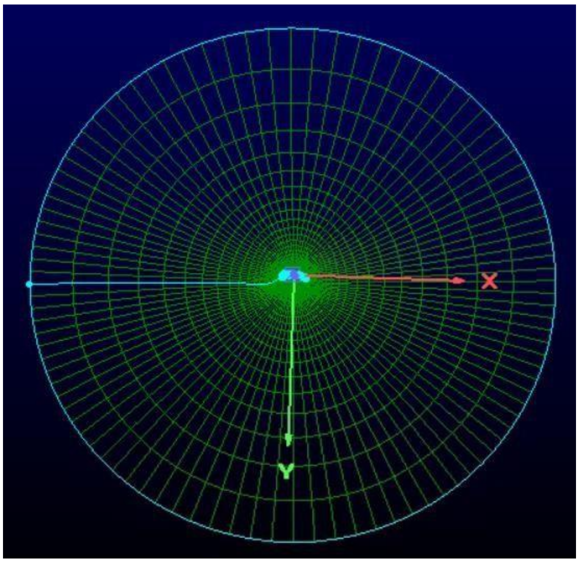

Figure 4-4: O-type grid

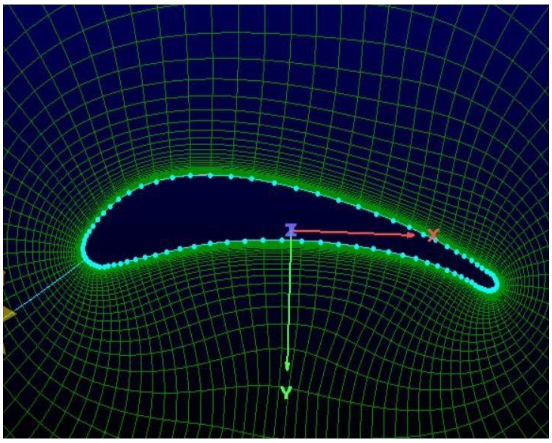

Figure 4-5: close-up of the airfoil

The main geometrical and numerical parameters of the final O-grid are summarized in Table 2.

Domain size in chord length	29c x 27c
Total number of cells	13720
Total number of points	27636
Max skewness	0.578827
Max aspect ratio	40.4806
Max non-orthogonality	3.21034
Growth rate	1.05

Table 2: important numerical parameters

4.1.4. Mesh Boundary Conditions

After the final O-grid mesh was generated, the grid was exported to OpenFOAM and the computational boundaries were defined through five patches: inlet, outlet, walls, front and back.

The inlet patch represents the boundary where the undisturbed flow enters the computational domain. In all the simulations, the inlet velocity field was set to a constant value of $U_\infty = 10\ m/s$. Therefore, a uniform velocity field was prescribed at the inlet, while the pressure was allowed to adjust inside the domain. The outlet patch represents the downstream boundary, where the flow leaves the domain. At this boundary, a reference pressure is imposed, while the velocity gradient is usually set to zero in order to avoid prescribing the outlet velocity profile artificially

The walls patch corresponds to the airfoil surface. It is defined as a wall-type boundary and contains 98 faces. On this patch, the no-slip condition is imposed for the velocity, meaning that the fluid velocity at the airfoil surface is equal to the solid-wall velocity. Since the airfoil is fixed in the two-dimensional simulations, the wall velocity is zero.

The front and back patches are both defined as empty boundaries. This condition is used in OpenFOAM for two-dimensional simulations. Although the mesh is technically extruded in the third direction, the empty condition removes the solution variation in that direction and forces the problem to be solved only in $x - y$ plane. The fact that both front and back patches contain 13720 faces, equal to the total number of cells, confirms that the mesh consists of a single layer of cells in the extrusion direction.

A summary of the important details is shown below in Table 3.

Patch	**Type**	**Number of faces**	**Physical meaning**
inlet	Patch	49	Uniform incoming flow
outlet	Patch	49	Downstream flow boundary
walls	Wall	98	Airfoil surface
front	Empty	13720	Front plane for 2D simulation
back	Empty	13720	Back plane for 2D simulation

Table 3: Summary of boundary conditions

4.2. Solver Theory

The numerical simulations were performed in OpenFOAM using incompressible finite volume solvers. As discussed in chapter 2, OpenFOAM uses a collocated finite volume arrangement, where the main flow variables are stored at the cell centers and the fluxes are evaluated through the cell faces. In this framework, the governing equations are integrated over each control volume and converted into a system of algebraic equations.

For incompressible flow, the coupling between velocity and pressure represents one of the main numerical issues. Unlike compressible flows, where pressure can be related to density through an equation of state, in incompressible flows the pressure field is not obtained from a thermodynamic relation. Instead, pressure acts as a constraint that enforces mass conservation. Therefore, the velocity field obtained from the momentum equation must also satisfy the continuity equation. This problem is known as pressure-velocity coupling. In OpenFOAM, segregated solvers commonly use pressure-correction algorithms to solve this coupling. The momentum equation is first solved using an estimated pressure field, producing an intermediate velocity field. This predicted velocity field does not necessarily satisfy continuity. A pressure correction equation is then derived from the continuity equation and used to correct both the pressure and the velocity fields. This procedure is repeated until the solution satisfies both momentum and mass conservation [9].

In the present work, two pressure-velocity coupling algorithms were considered: SIMPLE and PIMPLE. The SIMPLE algorithm was used for steady-state simulations, while the PIMPLE algorithm was used when the time-dependent evolution of the flow had to be resolved.

4.2.1. SIMPLE Algorithm

The acronym SIMPLE stands for Semi-Implicit Method for Pressure-Linked Equations. The algorithm was originally proposed by Patankar and Spalding [25] and is one of the most widely used pressure-velocity coupling methods for steady incompressible flows. In incompressible simulations, pressure is not obtained from an equation of state but acts as a constraint that ensures that the velocity field satisfies the continuity equation. Therefore, the pressure and velocity fields must be solved in a coupled way.

The SIMPLE algorithm is based on a guess-and-correct procedure. First, an initial pressure field p^* is assumed. The discretized momentum equations are then solved using this guessed pressure field, producing an estimated velocity field U^*. However, this predicted velocity field does not necessarily satisfy the continuity equation. For this reason, pressure and velocity are introduced:

$$p = p^* + p' \tag{4.1}$$

$$U = U^* + U' \tag{4.2}$$

Where p' is the pressure correction and U' is the velocity correction. The velocity correction is related to the pressure correction through the discretized momentum equation. By substituting the corrected velocity into the continuity equation, a pressure-correction equation is obtained. Solving this equation provides the correction required to update the pressure and velocity fields.

The procedure can be summarized as follows. A pressure field is guessed, the momentum equations are solved to obtain an intermediate velocity field, the pressure-correction equation is assembled from the continuity equation, and the pressure and velocity fields are corrected. This sequence is repeated iteratively until the residuals decrease and the velocity field satisfies mass conservation.

A key approximation of the SIMPLE algorithm is that some neighboring velocity-correction terms are neglected when deriving the pressure-correction equation. This simplification reduces the computational cost and makes the algorithm practical for steady-state CFD simulations, although several iterations are required before convergence is achieved.

In the present work, the SIMPLE algorithm was used through the OpenFOAM solver simpleFoam, which is designed for steady incompressible turbulent flows. Each airfoil case was solved iteratively for a fixed angle of attack until the residuals and aerodynamic coefficients reached stable values. The lift and drag coefficients were then extracted from the converged pressure and velocity fields.

4.2.2. PIMPLE Algorithm

The PIMPLE algorithm is a pressure–velocity coupling method used in OpenFOAM for transient incompressible flow simulations. Its name derives from the combination of the PISO and SIMPLE algorithms [26]. While SIMPLE is mainly used for steady-state calculations, PIMPLE is designed for time-dependent problems, where the flow field evolves at each time step and the pressure–velocity coupling must be satisfied during the temporal advancement of the solution.

In a transient simulation, the momentum equation includes the time derivative term and can be written in simplified form as:

$$\frac{\partial \mathbf{U}}{\partial t} + \nabla \cdot (\mathbf{U}\mathbf{U}) = -\frac{1}{\rho}\nabla p + \nu\nabla^2\mathbf{U} \tag{4.3}$$

where $\mathbf{U}$ is the velocity vector, p is the pressure, ρ is the density and ν is the kinematic viscosity. After time discretization, the solution is advanced from the previous time level n to the new time level n+1. The pressure and velocity fields at the new time level are not known in advance, so an iterative correction procedure is required.

The PIMPLE algorithm first solves the momentum equation using the available pressure field, obtaining a predicted velocity field. As in the SIMPLE algorithm, this predicted velocity does not necessarily satisfy continuity. A pressure equation is then solved to correct the pressure field and the mass fluxes through the cell faces. The velocity field is subsequently corrected using the updated pressure gradient. This procedure is repeated inside each time step until the desired level of pressure–velocity coupling is achieved.

The main feature of PIMPLE is the presence of outer corrector loops. These loops allow the solver to repeat the solution of the momentum and pressure equations several times within the same time step. This makes the algorithm more robust than a purely explicit transient procedure and allows larger time steps to be used compared with a standard PISO approach. The number of outer correctors controls how strongly the equations are coupled within each time step.

In addition to the outer correctors, PIMPLE also uses pressure correctors. These are internal pressure-correction steps used to improve the satisfaction of the continuity equation. Increasing the number of pressure correctors can improve the accuracy of the pressure–velocity coupling but also increases the computational cost.

Another parameter that may be used is the number of non-orthogonal correctors. These corrections are introduced when the mesh presents significant non-orthogonality. They improve the pressure equation solution when the face-normal direction is not well aligned with the line connecting neighboring cell centers. In the present mesh, the maximum non-orthogonality was only 3.2°, which indicates a very good cell alignment. Therefore, the influence of non-orthogonality on the solution is expected to be limited.

For transient simulations, the time step must also be selected carefully. A common stability indicator is the Courant number:

$$Co = \frac{U\Delta t}{\Delta x} \tag{4.4}$$

where U is a characteristic velocity, Δt is the time step and Δx is a characteristic cell size. The Courant number represents the distance travelled by the flow during one time step relative to the local cell size. If the Courant number is too large, the solution may become unstable or inaccurate. Therefore, the time step must be chosen to ensure a stable temporal evolution of the flow [27].

In the present work, the PIMPLE algorithm was used through the OpenFOAM transient solver when unsteady effects were considered important. This is particularly relevant at high angles of attack, where flow separation and vortex shedding may occur around the airfoil. In these conditions, the aerodynamic coefficients do not necessarily converge to constant values but may oscillate with time. Therefore, the lift and drag coefficients must be evaluated from the time history of the solution, generally after the initial transient phase has passed.

Compared with SIMPLE, the PIMPLE algorithm is more suitable for capturing the time-dependent behavior of separated flows. While SIMPLE provides a steady solution for each angle of attack, PIMPLE allows the development of unsteady structures in the wake and around the airfoil surface. This makes it useful for cases where the flow cannot be accurately represented by a single steady-state field.

In summary, the PIMPLE algorithm was adopted when the aerodynamic response of the airfoil required a transient treatment. Its combination of time advancement, pressure correction and outer iterative loops provides a robust framework for solving incompressible unsteady flows in OpenFOAM.

4.3. Turbulence Models

Turbulence modeling is one of the most important aspects of CFD simulations involving external aerodynamic flows. The flow around the airfoil is characterized by strong velocity gradients close to the wall, pressure variations between the suction and pressure sides, possible boundary-layer separation, and wake formation downstream of the trailing edge. These phenomena directly affect the aerodynamic coefficients obtained from the simulation. Therefore, the choice of turbulence model can significantly influence the predicted lift and drag curves.

Direct numerical resolution of all turbulent scales is not practical for the number of airfoil simulations required in this work. Therefore, a Reynolds-averaged Navier–Stokes approach was adopted. The averaging process introduces additional unknown terms, known as Reynolds stresses. These stresses represent the effect of turbulent fluctuations on the mean flow. Since the Reynolds stresses are not known directly, the system of equations becomes unclosed. A turbulence model is therefore required to relate the Reynolds stresses to mean flow quantities. This is usually done through the Boussinesq hypothesis, where the Reynolds stresses are modelled by introducing a turbulent or eddy viscosity [25].

The eddy-viscosity concept assumes that the effect of turbulence on the mean flow can be represented in a way similar to molecular viscosity, but with an additional turbulent viscosity μ_t. Therefore, the turbulence model mainly provides a method to calculate this turbulent viscosity from local flow quantities. Different turbulence models use different transport equations and assumptions to estimate μ_t, and this is why their predictions can differ, especially in separated-flow regions.

In the present work, two turbulence models were used: the Spalart–Allmaras model and the k-ω SST model. Both models are widely used for aerodynamic applications, but they have different levels of complexity. The Spalart–Allmaras model is a one-equation model that solves a transport equation for a modified turbulent viscosity. The k-ω SST model is a two-equation model that solves transport equations for the turbulent kinetic energy k and the specific dissipation rate ω. The comparison between these two models allows the sensitivity of the predicted aerodynamic coefficients to the turbulence closure to be evaluated.

The importance of turbulence modelling in airfoil simulations is particularly high because the lift and drag coefficients are strongly affected by the boundary-layer behavior. If the boundary layer remains attached, the pressure distribution around the airfoil is generally smooth and the aerodynamic forces may converge to steady values. However, when the angle of attack increases, the adverse pressure gradient becomes stronger, and the flow may separate from the surface. In this condition, the prediction of separation onset and wake development depends strongly on the turbulence model. For this reason, both a simpler model and a more advanced two-equation model were considered.

4.3.1. Spalart-Allmaras Model

The Spalart-Allmaras model [28] is a one-equation turbulence model developed mainly for aerodynamic applications. It belongs to the family of eddy-viscosity models and is commonly used for external flows around airfoils, wings and other streamlined bodies. Compared with two-equation models, it has a lower computational cost because it solves only one additional transport equation. For this reason, it is often adopted when several simulations must be performed, as in the generation of lift and drag coefficient curves over a range of angles of attack.

The transported variable of the model is not directly the turbulent viscosity, but a modified turbulent kinematic viscosity, usually denoted as $\tilde{\nu}$. The turbulent kinematic viscosity ν_t, which is used in the RANS momentum equations, is then obtained from this variable through a damping function:

$$\nu_t = \tilde{\nu} f_{v1} \tag{4.5}$$

where f_{v1} is a near-wall damping function. This correction is necessary because the turbulent viscosity must decrease close to solid walls, where viscous effects dominate and the no-slip condition strongly influences the flow.

The transport equation for the modified turbulent viscosity can be written in the following general form:

$$\frac{\partial \tilde{\nu}}{\partial t} + U_j \frac{\partial \tilde{\nu}}{\partial x_j} = c_{b1} \tilde{S} \tilde{\nu} + \frac{1}{\sigma} \left[\frac{\partial}{\partial x_j} \left((\nu + \tilde{\nu}) \frac{\partial \tilde{\nu}}{\partial x_j} \right) + c_{b2} \frac{\partial \tilde{\nu}}{\partial x_j} \frac{\partial \tilde{\nu}}{\partial x_j} \right] - c_{w1} f_w \left(\frac{\tilde{\nu}}{d} \right)^2 \tag{4.6}$$

In this equation, U_j is the mean velocity component, ν is the molecular kinematic viscosity, d is the distance from the closest wall, and c_{b1}, c_{b2}, c_{w1} and σ are model constants. The terms f_w and $\tilde{S}$ are auxiliary functions used to control the behavior of the model, especially in the near-wall region.

The left-hand side of the equation represents the unsteady and convective transport of $\tilde{\nu}$. On the right-hand side, the first term represents the production of turbulent viscosity due to the mean velocity gradients. The terms inside the square brackets represent diffusion, which accounts for the spatial redistribution of $\tilde{\nu}$ through molecular and turbulent effects. The last term is the destruction term and is particularly important close to solid walls. Since this term depends on the wall distance d, it reduces the turbulent viscosity near the airfoil surface and helps the model reproduce the near-wall behavior of boundary layers.

For airfoil simulations, the Spalart–Allmaras model is attractive because it is relatively robust and computationally efficient. It generally performs well for attached boundary layers and mildly separated aerodynamic flows. This makes it suitable for the initial evaluation of the reconstructed airfoil, especially at low and moderate angles of attack where the flow is expected to remain mostly attached.

However, the model also presents limitations. Since it solves only one transport equation, it does not explicitly compute the turbulent kinetic energy or a separate turbulence length scale. As a consequence, its prediction of strong separation, stall and complex wake structures may be less accurate than that of more advanced two-equation models. This limitation is relevant for the present work because the aerodynamic coefficients are required over a range of angles of attack, including conditions where separation may occur.

In this thesis, the Spalart–Allmaras model was used as one of the turbulence closures for the two-dimensional simulations of the reconstructed airfoil. Its results were compared with those obtained using the k-ω SST model in order to evaluate the influence of the turbulence model on the predicted lift and drag coefficients. This comparison is important because the resulting aerodynamic coefficients will later be used as input data for the actuator line model of the vertical-axis wind turbine.

4.3.2. K-ω SST Model

The k-ω SST model [29] is a two-equation eddy-viscosity turbulence model widely used in external aerodynamic simulations. The acronym SST stands for Shear Stress Transport. This model was developed by Menter to combine the advantages of the standard k-ω model near solid walls with the advantages of the k-ε model in the free-stream region. For this reason, it is commonly adopted for flows involving boundary layers, adverse pressure gradients and possible flow separation.

Unlike the Spalart–Allmaras model, which solves one transport equation for a modified turbulent viscosity, the k-ω SST model solves two transport equations. The first one is for the turbulent kinetic energy k, which represents the intensity of the turbulent velocity fluctuations. The second one is for the specific dissipation rate ω, which is related to the rate at which turbulent kinetic energy is dissipated. The turbulent kinetic energy can be defined as:

$$k = \frac{1}{2}(u'^2 + v'^2 + w'^2) \tag{4.7}$$

where u', v', and w' are the fluctuating velocity components. Physically, k gives a measure of the energy contained in the turbulent fluctuations. The variable ω, instead, provides information about the turbulence time scale and can be interpreted as a frequency associated with the dissipation of turbulence.

In the standard k-ω formulation, the turbulent viscosity is obtained from the two transported variables as:

$$\mu_t = \rho \frac{k}{\omega} \tag{4.8}$$

where ρ is the fluid density. This turbulent viscosity is then introduced into the RANS momentum equations to model the effect of turbulent fluctuations on the mean flow.

The transport equation for the turbulent kinetic energy may be written in general form as:

$$\frac{\partial \rho k}{\partial t} + \frac{\partial \rho U_j k}{\partial x_j} = P_k - \beta \rho k \omega + \frac{\partial}{\partial x_j}\left[(\mu + \sigma_k \mu_t)\frac{\partial k}{\partial x_j}\right] \tag{4.9}$$

where P_k is the production of turbulent kinetic energy due to mean velocity gradients, $\beta^* \rho k \omega$ is the dissipation term, and the last term represents diffusion.

The transport equation for the specific dissipation rate can be expressed as:

$$\frac{\partial \rho \omega}{\partial t} + \frac{\partial \rho U_j \omega}{\partial x_j} = P_k - \beta \rho \omega^2 + \frac{\partial}{\partial x_j}\left[(\mu + \sigma_\omega \mu_t)\frac{\partial \omega}{\partial x_j}\right] \tag{4.10}$$

where P_ω is the production term of ω, ^{2} is the destruction term, and the last term represents diffusion. In the SST formulation, additional blending and limiter functions are introduced to improve the model behavior in wall-bounded and separated flows.

The main characteristic of the SST model is the use of blending functions. Close to the wall, the model behaves like a k-ω model, which is well suited for resolving the near-wall region of boundary layers. Far from the wall, the formulation gradually changes toward a k-ε-type behavior, reducing the sensitivity of the standard k-ω model to the prescribed free-stream value of ω. This makes the model more robust for external aerodynamic applications, where the free-stream turbulence conditions may not be known exactly.

Another important feature of the k-ω SST model is the shear-stress transport limiter. This limiter improves the prediction of separated flows by limiting the turbulent viscosity in regions with adverse pressure gradients. This is particularly relevant for airfoil simulations because, as the angle of attack increases, the boundary layer may separate from the surface and the aerodynamic coefficients become strongly dependent on the ability of the turbulence model to predict separation onset and wake development.

For the present work, the k-ω SST model was selected because the reconstructed airfoil may experience adverse pressure gradients and separated-flow conditions over part of the angle-of-attack range. This is especially important because the lift and drag coefficients obtained from the two-dimensional simulations are later used as data input for the actuator line model. Since the relative velocity and angle of attack of a vertical-axis wind turbine blade vary continuously during rotation, the aerodynamic database must be reliable not only in attached-flow conditions, but also close to stall and separation.

Compared with the Spalart–Allmaras model, the k-ω SST model has a higher computational cost because it solves two additional transport equations instead of one. However, this cost remains acceptable for two-dimensional airfoil simulations and is justified by the improved treatment of near-wall turbulence and adverse pressure-gradient effects. Therefore, the comparison between Spalart–Allmaras and k-ω SST provides useful information about the sensitivity of the computed aerodynamic coefficients to the selected turbulence closure.

4.3.3. Turbulence Model Implementation in OpenFOAM

In OpenFOAM, the turbulence model is selected through the turbulence properties dictionary of the case. For the present simulations, incompressible RANS turbulence modelling was activated, and the selected closure model was changed according to the case being analyzed. Two turbulence models were considered: Spalart–Allmaras and k-ω SST.

For the Spalart–Allmaras simulations, the model was set as:

```
simulationType  RAS;

RAS
{
    RASModel         SpalartAllmaras;
    turbulence       on;
    printCoeffs      on;
}
```

For the *k*-*ω* SST simulations, the same dictionary was modified by selecting:

```
simulationType  RAS;

RAS
{
    RASModel         kOmegaSST;
    turbulence       on;
```

```
    printCoeffs      on;
}
```

The initial and boundary condition files were also adapted according to the selected turbulence model. For Spalart–Allmaras, the transported turbulence variable is $\tilde{\nu}$, which is defined in OpenFOAM through the nuTilda field. For the k-ω SST model, the required transported variables are the turbulent kinetic energy k and the specific dissipation rate ω. In both cases, the turbulent viscosity field nut is calculated by the turbulence model and used in the momentum equations.

The same computational mesh, inlet velocity and numerical settings were used for both turbulence models. This allowed the differences in the resulting lift and drag coefficients to be attributed mainly to the turbulence closure rather than to changes in the mesh or boundary conditions.

4.4. Case Matrix

The numerical campaign was organized progressively. The cases were not treated as independent simulations, but as a sequence of steps used to build and refine the final setup. Each group of simulations was introduced either to verify the OpenFOAM workflow or to address a limitation observed in the previous configuration.

All simulations were performed using the blade profile described in Chapter 3, the final O-grid mesh type presented in section 4.1, and a constant inlet wind velocity of $U_\infty = 10$m/s. The main output quantities were the lift coefficients and the drag coefficients, that are required later as aerodynamic input data for the actuator line model used in the turbine simulations.

The first numerical setup was based on the OpenFOAM airfoil2D tutorial and used the steady-state solver simpleFoam with the Spalart-Allmaras turbulence model. This case allowed the OpenFOAM workflow, boundary conditions, force coefficient calculation and airfoil orientation to be tested. However, the results obtained with this steady formulation shower important limitations for the prediction of stall and separated flow behavior. For this reason, the study was extended to the transient solver pimpleFoam.

The second group of simulations used pimpleFoam with the same Spalart-Allmaras turbulence model. This transient formulation allowed the flow field to evolve in time and made it possible to monitor the temporal behavior of the aerodynamic coefficients. The simulations were performed for different Reynolds numbers in order to evaluate the sensitivity of the airfoil response to the flow regime. After this step, some numerical parameters of the transient solver were adjusted to improve the stability of the force signals.

Finally, the turbulence model was changed from Spalart-Allmaras to K-ω SST. This final case group was introduced because the Spalart-Allmaras model, although computationally efficient and suitable for attached aerodynamic flows, may be less accurate in the presence of strong adverse pressure gradients and separation. The K-ω SST was tested to evaluate whether a two-equation turbulence closure could improve the prediction of stall behavior, especially for negative angles of attack.

4.4.1. Case A: simpleFoam + Spalart-Allmaras

The first case group was performed using the steady-state OpenFOAM solver simpleFoam together with the Spalart–Allmaras turbulence model. This setup was adapted from the OpenFOAM airfoil2D tutorial, which is designed for incompressible flow around a two-dimensional airfoil. The purpose of this initial case was not only to obtain preliminary aerodynamic coefficients, but also to verify that the reconstructed geometry, mesh, boundary conditions and force coefficient settings were correctly implemented in OpenFOAM.

This first case was performed at a Reynolds number of 10^6, with angles of attack ranging from -40° to 40°. The use of simpleFoam allowed a steady solution to be obtained for each angle of attack. Since simpleFoam is based on the SIMPLE pressure–velocity coupling algorithm, the solver iterates until the residuals and monitored quantities reach a stable value. The lift and drag coefficients were then extracted from the converged solution.

The Spalart–Allmaras model was selected for this first setup because it is commonly used for external aerodynamic applications and has a relatively low computational cost. As a one-equation model, it provides an efficient way to estimate the turbulent viscosity while keeping the numerical setup simple. This made it suitable for the initial phase of the OpenFOAM implementation.

This case was used as a preliminary steady-state reference and as a verification step for the OpenFOAM workflow, including the force-coefficient calculation and the implementation of the reconstructed airfoil mesh. The results obtained from this case are discussed in Section 4.5, where the limitations of the steady formulation are evaluated.

4.4.2. Case B: pimpleFoam + Spalart-Allmaras

The second case group was introduced to overcome the limitations observed with the steady solver. The same airfoil geometry, mesh, inlet velocity and Spalart–Allmaras turbulence model was kept, but the solver was changed from simpleFoam to pimpleFoam. This allowed the simulations to be performed in transient form.

The use of pimpleFoam is important because the flow around an airfoil at high angles of attack may not converge to a single steady solution. When separation occurs, vortices may be generated and shed into the wake, causing the lift and drag coefficients to oscillate with time. In this situation, an instantaneous value of C_L or C_D is not representative of the aerodynamic behavior. Instead, the coefficients must be analysed after the initial transient phase and, when necessary, averaged over a suitable time interval.

The simulations were carried out for Reynolds numbers of 10^4, 10^5, and 10^6. The AoA range was limited to -40°≤ α ≤40°. This interval was selected because simulations performed at angles further away from this range showed strong numerical instability and highly oscillatory force coefficients, making the results difficult to interpret. Therefore, the -40° to 40° range represented a compromise between covering the relevant aerodynamic behavior of the airfoil and maintaining acceptable numerical stability. The objective was to evaluate whether the transient solver could provide more realistic aerodynamic trends than the steady case and to observe the sensitivity of the coefficients to Reynolds number.

In this group of simulations, the aerodynamic coefficients were monitored as functions of time. At the beginning, the coefficient presents strong initial transients, with large spikes caused by the adjustment of the flow field from the initial condition. After this initial phase, the signal reaches a more stable oscillatory behavior. This confirms that the transient solver does not provide a single converged value like simpleFoam, but a time-dependent coefficient history from which representative values must be extracted after the initial transient has passed. An example of the lift coefficient vs time can be seen in Figure 4-6.

The influence of the transient numerical settings, including the maximum Courant number and the number of outer correctors, is discussed in Section 4.5.

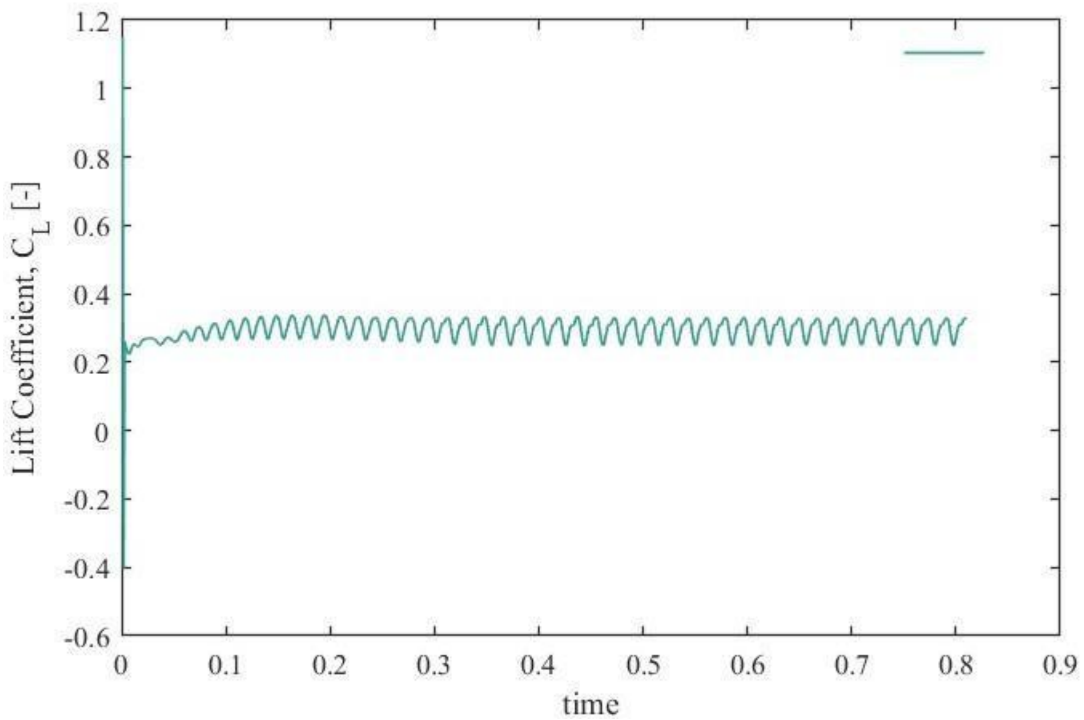

Figure 4-6: Lift coefficient as a function of time for an AoA of 10°

4.4.3. Case C: pimpleFoam + k- ω SST

The final case group was introduced after the transient simulations with pimpleFoam and the Spalart–Allmaras model still showed limitations in the prediction of stall behavior. Although the use of pimpleFoam allowed the flow field to evolve in time, the turbulence closure remained an important factor in the accuracy of the aerodynamic coefficients, especially in separated-flow conditions. For this reason, the solver was kept unchanged, while the turbulence model was modified from Spalart–Allmaras to k-ω SST.

The k-ω SST model was selected because it is generally more suitable for flows involving adverse pressure gradients and separation. This is important for the present airfoil because the simulations cover a wide range of angles of attack, where the flow may separate from the surface and the lift coefficient may no longer follow a linear trend. Compared with Spalart–Allmaras, which is a one-equation model, k-ω SST solves two transport equations and can provide a more detailed representation of the turbulent behavior near the wall and in separated regions.

In this case, the same reconstructed airfoil geometry, O-type mesh and inlet velocity of $U_\infty = 10\ m/s$ were maintained. Therefore, the differences observed between the Spalart–Allmaras and k-ω SST results can be mainly attributed to the turbulence model rather than to changes in the computational domain or boundary conditions. The objective of this case was to evaluate whether the k-ω SST model could improve the prediction of the aerodynamic response of the reconstructed airfoil, particularly at negative angles of attack where the previous simulations still presented uncertainties.

This case was especially relevant because the final purpose of the two-dimensional CFD analysis is to generate lift and drag coefficient curves for the actuator line model. Since the actuator line method calculates the aerodynamic forces from tabulated airfoil data, the reliability of the C_l and C_d curves directly affect the turbine simulation. For this reason, the turbulence model comparison was necessary before selecting the aerodynamic database to be used in the following stage of the work.

The results obtained with pimpleFoam and k-ω SST are discussed in Section 4.5, where they are compared with the Spalart–Allmaras results in terms of lift coefficient behavior, stall prediction and suitability for the final aerodynamic database.

4.5. Results and Discussion

This section discusses the results of the numerical campaign described in Section 4.4. The discussion focuses on the influence of the solver formulation, Reynolds number, transient numerical settings and turbulence model on the aerodynamic coefficients of the reconstructed airfoil. Since the final objective is to generate $C_L$and $C_D$curves for the actuator line model, the results are evaluated mainly in terms of physical consistency and suitability for the turbine simulations.

The discussion follows the same progression as the numerical campaign. First, the steady simpleFoam results are compared with the transient pimpleFoam simulations in order to evaluate the importance of resolving the time-dependent behavior of the flow. Then, the influence of Reynolds number is discussed. Finally, the effect of changing the turbulence model from Spalart-Allmaras to k-ω SST is analyzed, with particular attention to stall prediction and separated-flow behavior. The flow field visualizations obtained in ParaView are used to support the interpretation of the aerodynamic coefficient curves.

4.5.1. Steady vs. Transient Solver Behavior

The first comparison concerns the difference between the steady and transient solver formulations. The initial simulations were performed using simpleFoam with the Spalart-Allmaras turbulence model. This case was useful as a preliminary numerical test because it allowed the OpenFOAM workflow, boundary conditions and force coefficient calculation to be verified. However, the aerodynamic trends obtained from this setup showed important limitations.

As can be seen from Figure 4-7, the lift coefficient obtained with simpleFoam remained almost linear over the AoA range investigated and did not show a clear stall behavior. This result is not fully realistic for an airfoil operating at high AoA, where flow separation should cause a reduction or change in the lift trend. The absence of a clear stall region can be related to the steady nature of the solver. Since simpleFoam searches for a stationary solution, it may force the flow to remain steady even when the physical flow should become unsteady due to separation and vortex shedding.

The drag coefficient also showed non-physical behavior for part of the AoA range (Figure 4-8). In particular, negative drag values appeared in some cases. Since drag is defined as the component of the aerodynamic force opposing the incoming flow direction, negative values are not physically meaningful for the present configuration. This indicated that the steady simulation was not suitable for generating the final aerodynamic database.

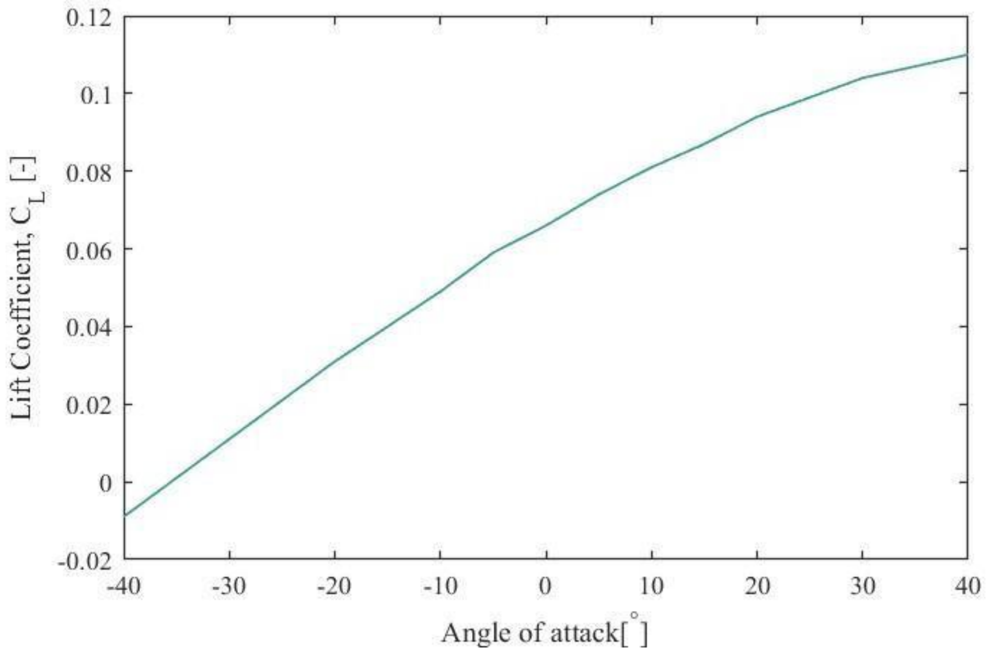

Figure 4-7: Cl(α) using simpleFoam and Spalart-Allmaras turbulence model

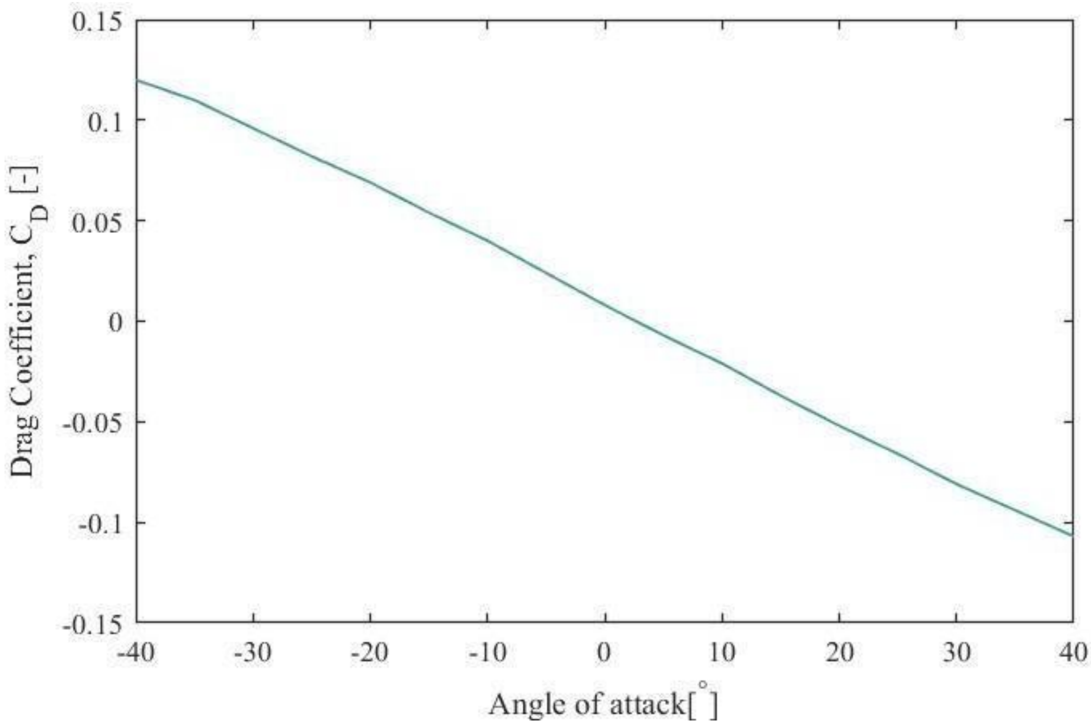

Figure 4-8: Cd(α) using simpleFoam and Spalart-Allmaras turbulence model

For this reason, the numerical analysis was extended to the transient solver pimpleFoam, keeping the same airfoil geometry, mesh, inlet velocity and Spalart-Allmaras turbulence model. The use of a transient solver is more appropriate when the flow around the airfoil may separate and generate time-dependent aerodynamic loads. Unlike simpleFoam, pimpleFoam does not provide a single steady coefficient value, but a time history of the aerodynamic forces.

4.5.2. PimpleFoam with Spalart-Allmaras Results

After the limitations observed with the steady simpleFoam simulations, the transient solver pimpleFoam was adopted while maintaining the Spalart–Allmaras turbulence model. This setup allowed the flow field and aerodynamic forces to evolve in time, making it more suitable for conditions where separation and vortex shedding may occur.

The aerodynamic coefficients obtained with pimpleFoam were analyzed for three Reynolds numbers: 10^4, 10^5, and 10^6. The Reynolds number is an important parameter because it expresses the ratio between inertial and viscous forces in the flow. Therefore, changing Re affects the boundary-layer behavior, the tendency of the flow to separate, and the resulting lift and drag coefficients. In the present work, the Reynolds-number comparison was used to evaluate the sensitivity of the reconstructed airfoil response to different flow regimes.

The comparison was performed over the angle-of-attack range -40° ≤ α ≤40°, since simulations outside this interval showed stronger numerical instability and highly oscillatory force coefficients. Figure 4-9 and Figure 4-10 show the resulting $C_l(\alpha)$ and $C_d(\alpha)$ curves.

From the lift coefficient curves, it can be observed that the Reynolds number influences both the magnitude and regularity of the predicted aerodynamic response. At lower Reynolds numbers, viscous effects are more important, and the coefficient trends tend to be less smooth, especially at higher angles of attack. At $Re = 10^6$, the lift curve presents a more coherent trend and is closer to the operating range expected for the turbine application. For this reason, the higher Reynolds-number case was considered more representative for the subsequent turbulence-model comparison.

The drag coefficient is also affected by Reynolds number. In general, changes in Re modify the relative importance of viscous drag and pressure drag, especially when the flow begins to separate. Larger differences between the curves are expected at higher angles of attack, where separation and wake formation dominate the aerodynamic behavior. Therefore, the Reynolds number comparison confirms that the airfoil polar data are sensitive to the selected flow regime.

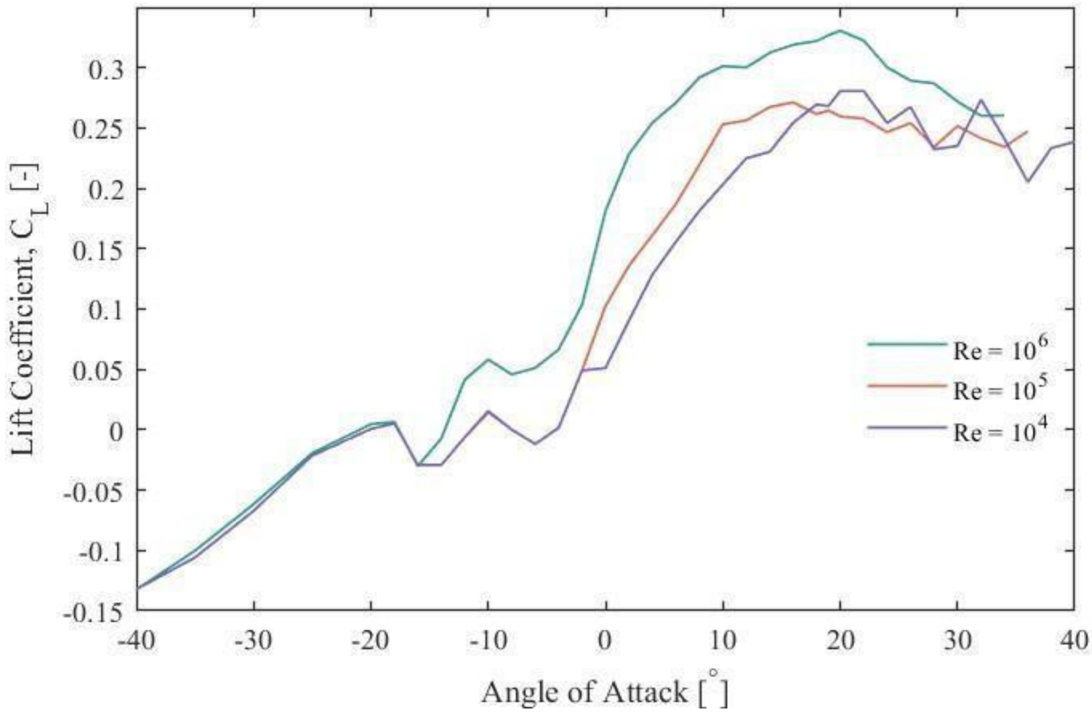

Figure 4-9: Cl (α) for three different Reynolds number using pimpleFoam with Spalart-Allmaras turbulence model

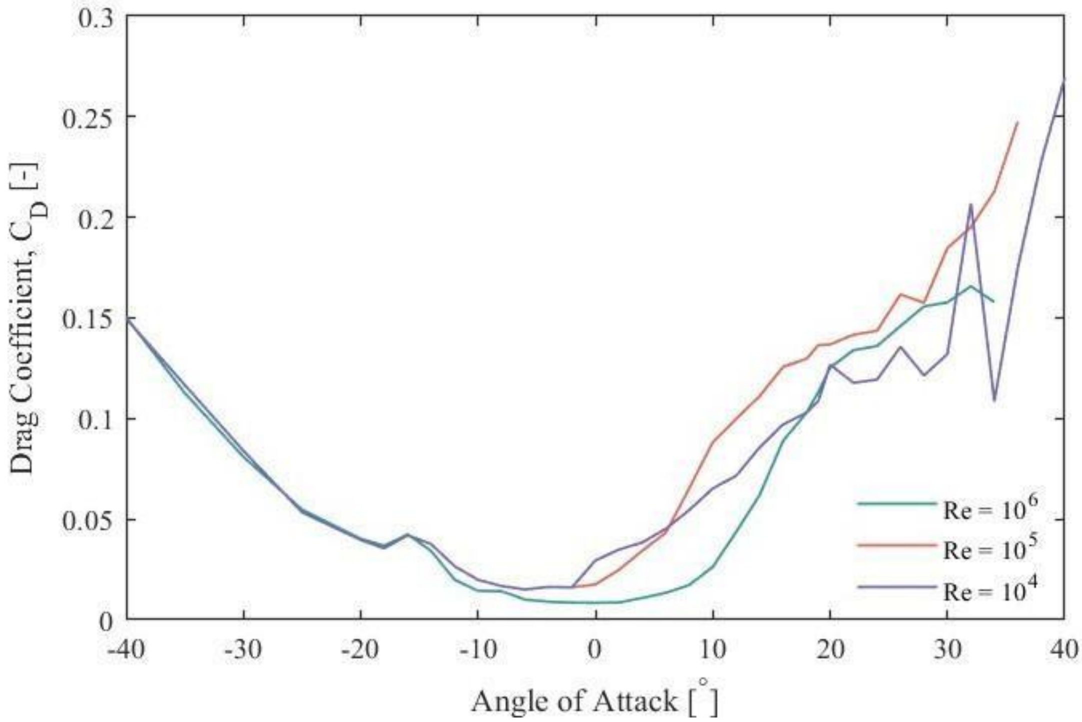

Figure 4-10:C_d (α) for three different Reynolds number using pimpleFoam with Spalart-Allmaras turbulence model

4.5.3. Influence of Transient Numerical Settings

After the first pimpleFoam simulation with the Spalart-Allmaras model, the numerical settings of the transient solver were adjusted to improve the stability of the aerodynamic coefficient curves. In transient CFD simulations, the time step has a direct influence on the solution because it controls how the flow field evolves from one time level to the next. If the time step is too large, the force coefficient might show excessive oscillations or numerical instability.

For this reason, the maximum Courant number was reduced from 0.75 to 0.25. This reduced the distance travelled by flow information during each time step and improved the temporal resolution of the simulation. In addition, the number of outer correctors was changed from 5 to 3. This value was sufficient to maintain pressure-velocity coupling inside each time step while reducing unnecessary computational cost.

Figure 4-11 shows the effect of these changes on the lift coefficient curve. After modifying the transient settings, the $C_l(\alpha)$ curve became more stable. This indicates that part of the irregular behavior observed in the first transient simulation was related to numerical settings rather than only to physical flow unsteadiness.

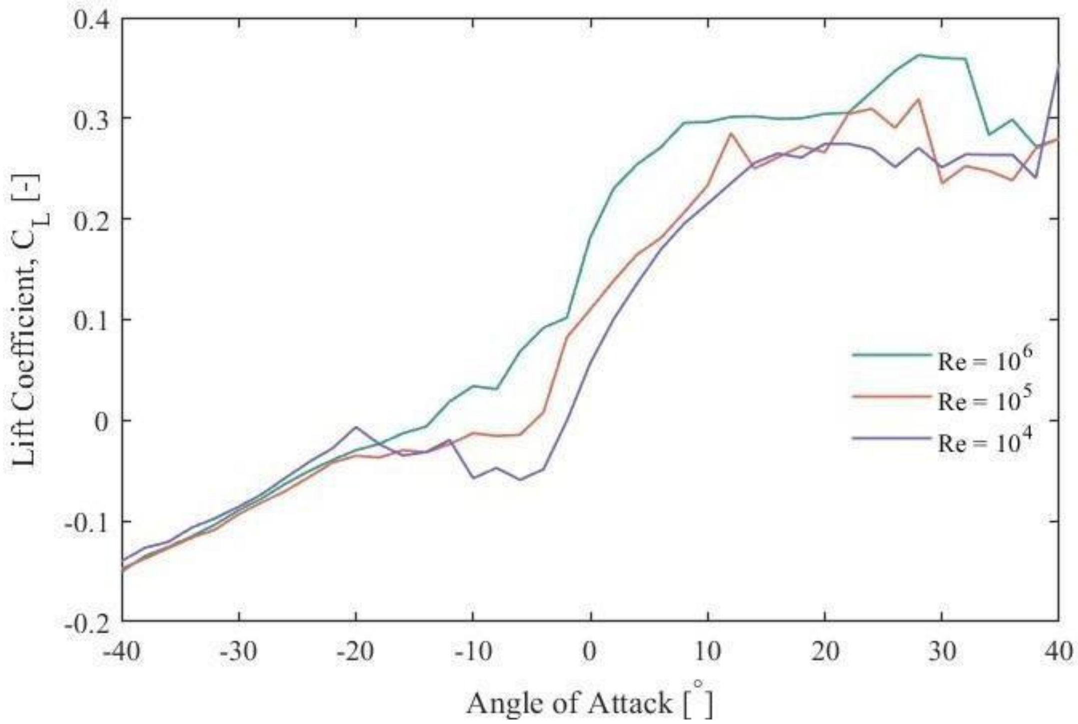

Figure 4-11: Cl(α) after changing maxCo and nOuterCorrector

Nevertheless, the adjustment of the solver settings did not completely solve the limitations related to stall prediction, especially for negative AoA. Therefore, the next step was to investigate the influence of the turbulence model by replacing Spalart-Allmaras with k-ω SST.

4.5.4. PimpleFoam with k-ω SST Results

The final set of simulations was performed using the transient solver pimpleFoam with the k-ω SST turbulence model. This model was introduced to improve the prediction of separated-flow behavior and stall, especially because the previous simulations with Spalart-Allmaras still showed limitations in the negative AoA region.

Figure 4-12 presents the raw lift coefficient values obtained directly from the pimpleFoam simulations with the k-ω SST turbulence model. These data have not yet been smoothed or interpolated, and therefore some local oscillations are visible, especially at high angles of attack where the flow is more separated and the aerodynamic forces are more unsteady.

Compared with the previous Spalart-Allmaras results, the k-ω SST produces a more pronounced variation of the lift coefficient at negative AoA. In particular, the lift decreases for large negative angles and reaches a minimum between approximately -50° and -40°, depending on Reynolds number. This indicated that the model is more sensitive to adverse pressure gradients and separated-flow effects.

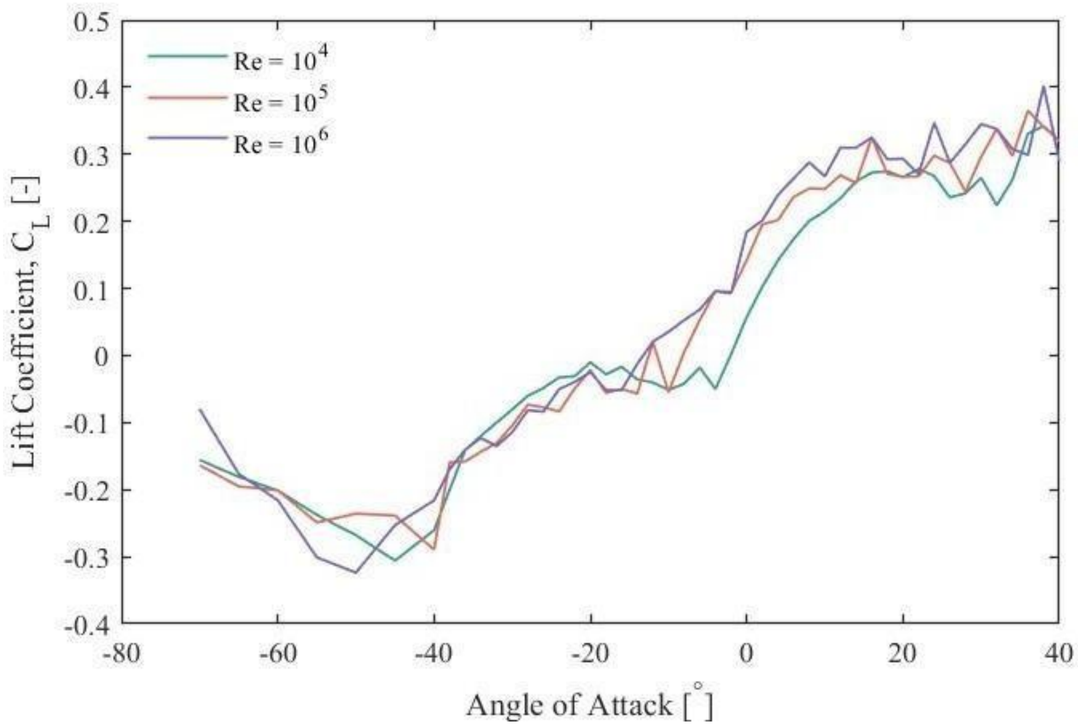

Figure 4-12:Raw lift coefficient values obtained with pimpleFoam and the k-ω SST turbulence model for different Reynolds numbers

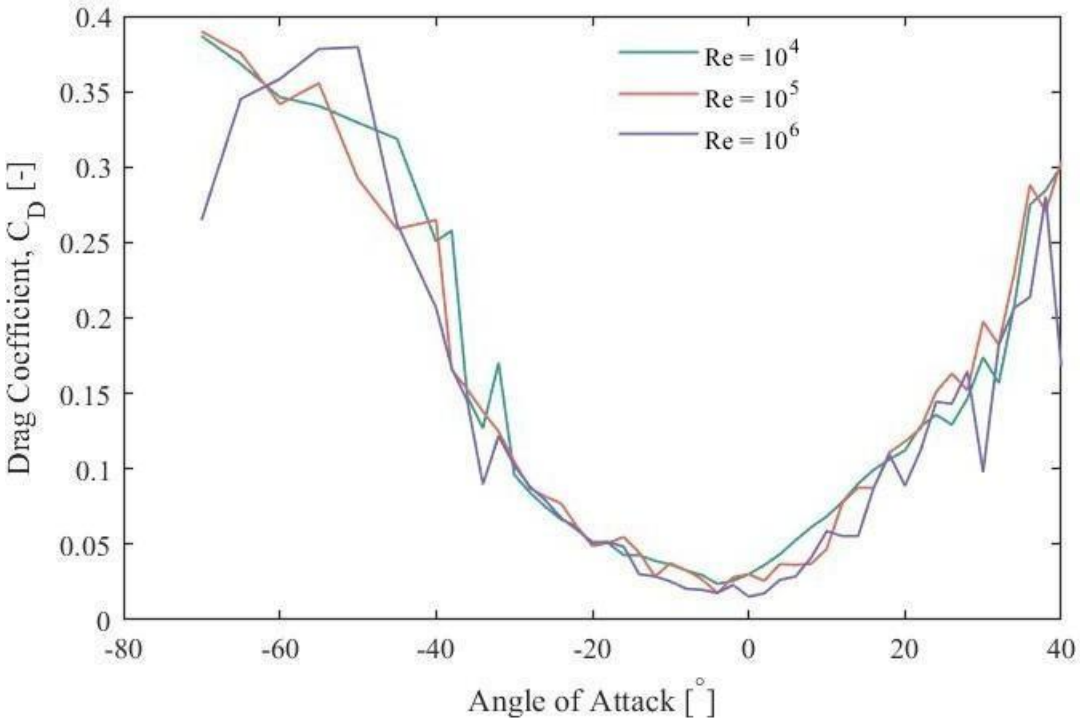

Figure 4-13:Raw drag coefficient values obtained with pimpleFoam and the k-ω SST turbulence model for different Reynolds numbers

Figure 4-13 shows the raw drag coefficient values obtained from this simulation. Its minimum value is at a slightly negative angle of attack because of the cambered geometry of the reconstructed airfoil. As the AoA increases in either the positive or negative direction away from the minimum drag region, $C_d(\alpha)$ increases progressively. This is expected because larger AoA increases the effective frontal resistance of the profile and promotes flow separation, both of which contribute to higher pressure drag.

4.5.5. Flow Field Visualization

The flow field visualizations obtained in ParaView were used to support the interpretation of the aerodynamic coefficient curves. Figure 4-14 shows instantaneous flow fields for five representative angles of attack: 40°, 20°, 0°, −20° and −40°. For each angle of attack, three frames were extracted from the transient simulation after the initial transient phase. Each column corresponds to the same time instant, allowing the temporal evolution of the flow field to be compared consistently between the different angles. The last column reports the velocity legend associated with each AoA. Therefore, the colour scale is not the same for all rows, and the figure should be interpreted mainly as a qualitative comparison of the flow structure.

The maximum velocity shown in the legend changes with angle of attack. The maximum value is approximately 2.1×10^1 m/s for $\alpha = 40°$, 1.8×10^1 m/s for $\alpha = 20°$,

1.3×10^1 m/s for $\alpha = 0°$, and 2.3×10^1 m/s for both $\alpha = -20°$and $\alpha = -40°$. These values indicate that the highest local accelerations occur for the large negative-angle cases, while the lowest maximum velocity is observed at the geometric zero angle.

The results show that the flow behavior changes significantly with angle of attack. At $\alpha = 0°$, the flow remains relatively attached to the airfoil surface and the wake is limited. However, the field is not perfectly symmetric, which is consistent with the cambered geometry of the reconstructed profile. This agrees with the aerodynamic coefficient curves, where the airfoil does not behave as a symmetric profile and the minimum drag is not located exactly at zero angle of attack.

At positive angles of attack, especially for $\alpha = 20°$and $\alpha = 40°$, larger separated regions and stronger wake structures are visible downstream of the airfoil. The flow becomes increasingly unsteady as the angle of attack increases. This behavior is consistent with the increase in drag observed in the $C_d(\alpha)$curve and with the reduced regularity of the lift coefficient at high positive angles. The case at $\alpha = 40°$shows a highly disturbed wake, indicating that the airfoil is operating in a strongly separated-flow regime.

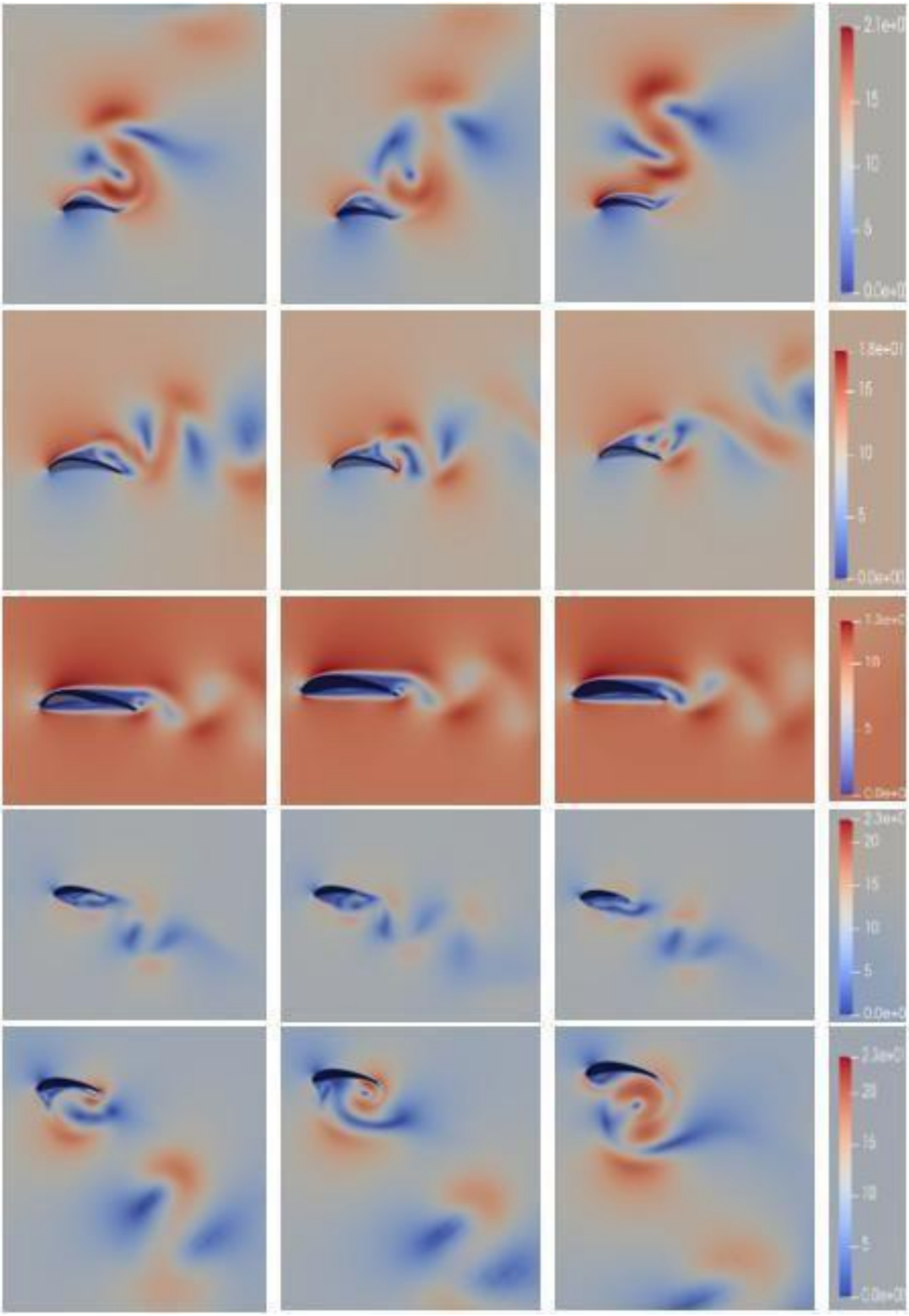

Figure 4-14: Flow field visualization for angles of attack of 40°, 20°, 0°, -20°, -40° (top to bottom)

For negative angles of attack, the flow separation develops on the opposite side of the airfoil. At $\alpha = -20°$, the wake is already more pronounced than at 0°, while at $\alpha = -40°$ the flow field shows large-scale separated structures and strong unsteadiness. This is consistent with the lift coefficient curve, where large negative angles correspond to a stronger negative aerodynamic response and increased drag.

The comparison between the frames at the three different times also confirms that the transient solver is necessary for these simulations. The separated structures in the wake change position and intensity with time, especially at high positive and negative angles of attack. Therefore, the aerodynamic coefficients cannot be interpreted as purely steady quantities. Instead, representative C_l and C_d values must be extracted from the developed part of the transient signal, after the initial numerical transient has passed.

Overall, the flow-field visualization supports the conclusions obtained from the coefficient curves. Low angles of attack are associated with a more attached and regular flow, while high positive and negative angles produce larger separated regions, stronger wake development and greater temporal variability. These features explain the increase in drag and the irregularities observed in the raw lift coefficient data.

4.5.6. Final Aerodynamic Database for ALM

The final objective of the two-dimensional CFD simulation was to generate an aerodynamic database suitable for the actuator line model used in the turbine simulations. In the ALM, the aerodynamic forces are computed as actuator points along the blade using tabulated airfoil data. For this reason, the lift and drag coefficients obtained in this chapter represent a fundamental input for the following stage of the numerical work.

The comparison between the different numerical cases showed that not all the computed datasets were suitable for this purpose. The steady simpleFoam results were useful as a preliminary OpenFOAM implementation and verification step, but the lift coefficient obtained with this solver did not show a clear stall behavior, while the drag coefficient presented non-physical values over part of the AoA range. Since the ALM requires physically consistent aerodynamic coefficients, the steady results were considered inadequate for the final polar definition.

The simulation with the Spalart-Allmaras turbulence model and the solver pimpleFoam represented a useful intermediate step. It improved the physical consistency of the results compared with the steady formulation and allowed the

Reynolds number influence to be evaluated. However, some limitations remained, especially in the negative AoA region, where stall behavior was not clearly captured. This suggested that the turbulence closure had a significant influence on the final airfoil polar.

For this reason, the k-ω SST model was tested with the transient solver. The resulting lift and drag curves showed a more pronounced response in the separate flow region, especially at negative AoA. The drag coefficient also remained positive over the analyzed range, which is physically consistent. Therefore, the pimpleFoam simulation with the k-ω SST turbulence model was considered the most suitable basis for the aerodynamic database.

Nevertheless, the raw CFD data still require further processing before being used in the ALM. The coefficient curves contain local oscillations, especially at high positive and negative AoA where the flow is separated and unsteady. These oscillations are expected because the values come from some transient CFD simulations and are influenced by time averaging, solver settings and turbulence modelling. For ALM implementation, however, the aerodynamic database must be continuous and sufficiently smooth, because abrupt variations in Cl and Cd can introduce numerical instabilities in the force calculation.

5 ALM Simulation

This chapter presents the numerical simulations performed using the Actuator Line Method to evaluate the power prediction of the vertical-axis wind turbine at low tip speed ratios. The two-dimensional CFD simulations described in the previous chapter were used to characterize the aerodynamic behavior of the reconstructed blade profile and to generate the aerodynamic coefficient database required by the actuator line model. However, two-dimensional airfoil simulations alone cannot provide the global power output of the complete rotating turbine. For this reason, a rotor-level numerical model is required.

The Actuator Line Method was selected because it allows the aerodynamic action of the rotating blades to be introduced into the flow field without explicitly resolving the full three-dimensional blade geometry. This reduces the computational cost compared with fully blade-resolved CFD while still allowing the unsteady blade loading to be evaluated during the turbine rotation. This aspect is particularly relevant for the present turbine, which operates in a low-TSR regime where the angle of attack varies significantly during each revolution and dynamic stall effects may influence the instantaneous aerodynamic forces.

In the present work, the ALM simulations are therefore used to estimate the turbine torque, power and power coefficient for the selected low-TSR operating conditions. The focus of the chapter is the numerical prediction of the rotor power response and its dependence on tip speed ratio. The chapter first introduces the theoretical formulation of the Actuator Line Method, then describes the aerodynamic coefficient database, the numerical setup implemented in OpenFOAM/turbinesFoam, the low-TSR operating conditions considered, and finally the resulting power predictions.

5.1. Introduction to the Actuator Line Method

The Actuator Line Method is a reduced order numerical approach originally developed by Sørensen and Shen [30] for the simulation of wind turbine wakes. The method was first introduced for horizontal axis wind turbines, when it became widely used because it allowed the aerodynamic action of rotating blades to be included in the CFD simulations without explicitly resolving the blade geometry. Later, the method was extended and adapted by Bachant et al. [31] to vertical-axis and cross flow turbines, for which the aerodynamic conditions are more strongly unsteady due to the cyclic variation of relative velocity and angle of attack during each revolution.

The ALM can be interpreted as an intermediate fidelity approach between simple momentum models, such as actuator disk models, and fully blade-resolved CFD simulations. Compared with an actuator disk model, the ALM preserves the individual blade position and time-dependent loading. Compared with blade-resolved CFD, it avoids the need for a body-fitted moving mesh around the blades, reducing the computational cost. For this reason, it is particularly useful when the objective is to estimate rotor-level quantities such as torque, power and power coefficient, rather than to resolve the detailed boundary-layer flow around the blade surface [31].

5.1.1. Blade Representation

In the ALM, the real blade geometry is replaced by a set of actuator elements distributed along the blade span. Each actuator element represents a finite portion of the blade and carries the aerodynamic information of the corresponding airfoil section(Figure 5-1). Therefore, the blade is not modelled as a solid surface inside the computational domain, but through a line of points where the aerodynamic forces are evaluated and later transferred to the surrounding flow field.

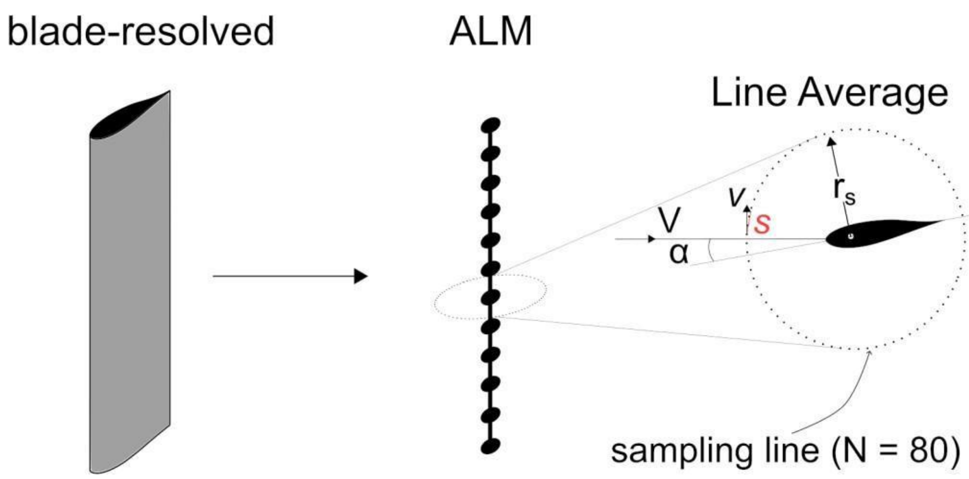

Figure 5-1: Visualization of actuator line and points

For the present vertical-axis wind turbine, each blade is represented by one actuator line extending along the blade height. Since the turbine has three blades, the numerical model consists of three actuator lines placed around the rotor axis and separated by 120 degrees in the azimuthal direction. During the simulation, these actuator lines rotate with the imposed angular velocity, reproducing the motion of the physical rotor.

The actuator elements are commonly defined at the quarter-chord location of the blade section. This location is used as the reference point for evaluating the local flow quantities and applying the aerodynamic loading. In this way, the blade is represented by its main geometrical and aerodynamic properties: spanwise position, chord length, airfoil coefficient database and rotational motion [31].

This representation avoids the need to generate a computational mesh that follows the exact shape and motion of the blade surface. As a result, the computational domain does not need to resolve the boundary layer or the exact blade shape during rotation.

This is suitable for the objective of the present chapter, which is the prediction of rotor power at low tip speed ratios rather than the detailed resolution of the local blade flow.

The aerodynamic behavior of the real blade is introduced through the lift and drag coefficients of the reconstructed airfoil profile, while the effect of rotation is represented by the motion of the actuator lines. The evaluation of the local velocity and angle of attack at each actuator element is described in the following subsection.

5.1.2. Local Velocity and Angle of Attack

After the blade has been represented as a set of actuator elements, the aerodynamic state of each element must be evaluated at every time step. This requires the calculation of the local relative velocity and the corresponding angle of attack. These quantities are fundamental in the actuator line formulation because they determine which lift and drag coefficients are selected from the aerodynamic database.

For each actuator element, the local inflow velocity is obtained from the CFD velocity field at the position of the actuator point. Since the actuator point generally does not coincide exactly with a cell center, the velocity must be interpolated from the surrounding computational cells. In the actuator line formulation described by Bachant, Goude and Wosnik, the inflow velocity is sampled at the quarter-chord location of each actuator element, using an interpolation procedure in OpenFOAM in order to obtain a smoother velocity value than would be obtained by using only the velocity of the cell containing the actuator point.

The actuator element also has a velocity due to the rotation of the turbine. This velocity depends on the angular velocity of the rotor and on the position of the actuator element with respect to the axis of rotation. It can be expressed as:

$$\vec{U}_{blade} = \vec{\omega} \times \vec{r} \tag{5.1}$$

where ω is the angular velocity vector and r is the position vector of the actuator element relative to the turbine axis.

The local relative velocity is then obtained by combining the sampled inflow velocity with the blade motion:

$$\vec{U}_{rel} = \vec{U}_{loc} - \vec{U}_{blade} \tag{5.2}$$

where U_{local} is the velocity interpolated from the CFD field and U_{blade} is the velocity of the actuator element due to rotation. The relative velocity represents the velocity effectively experienced by the blade section. Its magnitude is used in the aerodynamic force calculation, while its direction is used to determine the local angle of attack. A graphical representation can be seen in Figure 5-2.

The angle of attack α is evaluated as the angle between the relative velocity direction and the local chord line of the blade section. Once α is known, the corresponding aerodynamic coefficients are obtained by interpolation from the prescribed airfoil database. In this way, the instantaneous aerodynamic response of each blade section is linked to the local flow conditions computed by the CFD solver.

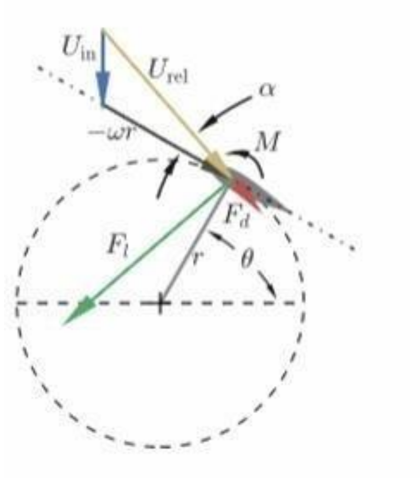

Figure 5-2: Visualization of ALM with vector diagram

For a vertical-axis wind turbine, the local velocity and angle of attack vary continuously during one rotor revolution. As the blade moves through different azimuthal positions, the relative contribution of the incoming flow and the blade rotational velocity changes. Consequently, both the magnitude and direction of U_{rel} change with time. This produces a cyclic variation of the angle of attack, which is one of the main sources of unsteady aerodynamic loading in vertical-axis turbines.

This aspect is especially important in the present work because the turbine is analyzed at low tip speed ratios. In this operating range, the rotational velocity is relatively small compared with the incoming wind velocity, and the blade can experience large instantaneous angles of attack during part of the revolution. Therefore, the correct evaluation of the local velocity and angle of attack is essential for the prediction of the aerodynamic forces and, consequently, for the estimation of torque and power.

5.1.3. Aerodynamic Forces Calculation and Projection

Once the local relative velocity and angle of attack have been evaluated for each actuator element, the aerodynamic forces acting on the corresponding blade section can be calculated. In the actuator line formulation, this calculation is based on two-dimensional aerodynamic coefficient data. The local angle of attack is used to interpolate the lift and drag coefficients from the aerodynamic database, while the magnitude of the relative velocity determines the dynamic pressure acting on the blade section.

The lift and drag forces acting on each actuator element are calculated as:

$$F_L = \frac{1}{2}\rho A_{elem} C_L \left|\vec{U}_{rel}\right|^2 \tag{5.3}$$

$$F_D = \frac{1}{2}\rho A_{elem} C_D \left|\vec{U}_{rel}\right|^2 \tag{5.4}$$

where F_L is the lift force, F_D is the drag force, ρ is the air density, A_{elem} is the area associated with the actuator element, C_L and C_D are the lift and drag coefficients, and $|\vec{U}_{rel}|$ is the local relative velocity. The area of each actuator element is obtained from the local chord and the spanwise length represented by the element.

The lift force is defined as perpendicular to the relative velocity, while the drag force acts in the direction opposite to the relative velocity. These forces are first computed in the local blade reference frame and are then transformed into the rotor coordinate system. This transformation is necessary because the aerodynamic forces must be related to the rotor motion in order to determine their contribution to the instantaneous torque and, consequently, to the predicted power output.

After the aerodynamic forces have been calculated at the actuator elements, they must be transferred to the surrounding flow field. The force is not applied directly to a single computational cell, because this would create a highly concentrated momentum source and could lead to numerical instabilities. Instead, the force is distributed smoothly over the neighboring cells using a projection function. A common choice is a Gaussian smoothing function, which distributes the actuator force according to the distance between the actuator element and the cell center [31].

The Gaussian projection function can be written as:

$$\eta = \frac{1}{\epsilon^3 \pi^{\frac{3}{2}}} exp\left[-\left(\frac{|\vec{r}^2|}{\epsilon}\right)\right] \tag{5.5}$$

where η is the projection function, ϵ is the smoothing width, and $|r|$ is the distance between the actuator element and the cell center. The parameter ϵ controls how widely the force is spread over the mesh. A small value produces a more concentrated force distribution, while a larger value spreads the force over a wider region of the computational domain.

The distributed actuator force is then introduced into the momentum equation as a source term. For incompressible flow, the momentum equation can be written as:

$$\frac{D\mathrm{u}}{Dt} = -\frac{1}{\rho}\nabla p + \upsilon \nabla^2 u + F_{turbine} \tag{5.6}$$

where u is the velocity field, p is the pressure, υ is the kinematic viscosity, and $F_{turbine}$ represents the actuator-line momentum source term introduced into the flow equations. Through this source term, the aerodynamic effect of the rotating blades is imposed on the CFD solution without explicitly resolving the blade surface.

In the present work, this procedure provides the connection between the two-dimensional aerodynamic database obtained from the airfoil simulations and the rotor-level power prediction. Since the turbine is investigated at low tip speed ratios, the relative velocity and angle of attack vary significantly during each revolution. Therefore, the accuracy of the calculated actuator forces depends strongly on the aerodynamic database, the force projection strategy and the treatment of unsteady aerodynamic effects.

5.2. Aerodynamic Database for ALM

The Actuator Line Method requires an aerodynamic database containing the airfoil coefficients used to compute the forces at each actuator element. In particular, the lift and drag coefficients must be provided as functions of the AoA. During the ALM simulation, the local angle of attack is evaluated at every actuator element, and the corresponding aerodynamic coefficients are obtained by interpolation from this database. This database is based on the two-dimensional CFD simulations described in Chapter 4. These simulations provide the aerodynamic coefficients of the reconstructed blade profile over the simulated range of angles of attack. However, this range is not sufficient for the ALM simulation of a VAWT. Unlike a conventional airfoil operating at a nearly fixed AoA, a VAWT blade experiences a large variation of AoA during one revolution, especially at low TSR. Therefore, the airfoil database must cover a much wider range of angles of attack than the one obtained from the 2D CFD simulations.

For this reason, the computed aerodynamic coefficients were post-processed before being introduced into turbinesFoam. The objective of this post-processing step was to generate a continuous and complete polar database suitable for the actuator line model. In particular, the lift and drag coefficients had to be extended to cover the full AoA range required by the ALM calculation.

5.2.1. Viterna-Corrigan Extrapolation

The ALM requires aerodynamic coefficients over the complete angle-of-attack range from −180° to +180°. In the present work, the two-dimensional CFD simulations described in Chapter 4 provide the lift and drag coefficients only over a limited angle-of-attack interval. However, during the operation of a vertical-axis wind turbine, especially at low tip speed ratios, the blade can experience large positive and negative instantaneous angles of attack during one revolution. Therefore, the aerodynamic database must be extended to cover the full range $-180° \leq \alpha \leq +180°$ before being used in the ALM simulations [32].

For this purpose, the Viterna-Corrigan [33] extrapolation method was applied. This method is commonly used in wind turbine aerodynamic calculations to extend airfoil polar data into the post-stall and deep-stall regions. The method assumes that, at large angles of attack, the airfoil behavior approaches that of a flat plate, allowing the lift and drag coefficients to be estimated beyond the available polar data.

The method requires the selection of an initial stall angle, α_{stall} , together with the corresponding lift and drag coefficients, C_{Lstall} and C_{Dstall}.. It also requires the blade aspect ratio AR, which is used to estimate the maximum drag coefficient at 90 degrees. According to the Viterna formulation, the maximum drag coefficient is calculated as:

$$C_{DMAX} = 1.11 + 0.018\ AR \tag{5.7}$$

The post-stall drag coefficient is then expressed as:

$$C_D = B_1 sin^2\alpha + \ B_2 cos\alpha \tag{5.8}$$

where:

$$B_1 = C_{DMAX} \tag{5.9}$$

$$B_2 = \frac{C_{Dstall} - C_{DMAX} sin^2\alpha_{stall}}{cos\alpha_{stall}} \tag{5.10}$$

The post-stall lift coefficient is calculated as:

$$C_L = A_1 sin\ 2\alpha + \ A_2 \frac{cos^2\alpha}{\sin\alpha} \tag{5.11}$$

where:

$$A_1 = \frac{C_{DMAX}}{2} \tag{5.12}$$

$$A_2 = (C_{Lstall} - C_{DMAX}\ sin\alpha_{stall}\ cos\alpha_{stall})\frac{sin\alpha_{stall}}{cos^2\alpha_{stall}} \tag{5.13}$$

These equations are applied in the post-stall region between the selected stall angle and 90°. The remaining parts of the polar are then completed by applying the same extrapolation logic and symmetry relations in order to obtain a continuous database over the complete range from −180° to +180°. In this way, the final polar contains coefficient values for every angle of attack that may be requested by the actuator line model.

This step is particularly important for the present turbine because the simulations are performed at low tip speed ratios. In this operating range, the relative velocity direction changes significantly during the blade revolution, and the actuator elements may reach angles of attack far outside the range directly simulated in Chapter 4. The extrapolated database therefore ensures that the aerodynamic force calculation remains defined and continuous throughout the full rotor motion.

5.2.2. Final ALM Input Database

After the Viterna-Corrigan extrapolation, the final aerodynamic database was obtained for the complete angle-of-attack interval from −180° to +180°. The final input database consists of tabulated values of lift coefficient, (C_L), and drag coefficient, (C_D), as functions of the angle of attack. These values are required by turbinesFoam to compute the aerodynamic forces at the actuator elements during the rotor simulation.

Figure 5-3 and Figure 5-4 show the final lift and drag coefficient distributions used as ALM input. The curves are reported for three Reynolds numbers, (10^4), (10^5), and (10^6), in order to provide the actuator line model with aerodynamic data over the range of Reynolds numbers expected during the simulations. During the calculation, the local angle of attack and Reynolds number evaluated at each actuator element are used to interpolate the corresponding aerodynamic coefficients from the database.

The lift coefficient curves show the expected change of sign between positive and negative angles of attack, with maximum and minimum values occurring in the post-stall region. The drag coefficient curves remain positive over the entire angle-of-attack range and reach their maximum values close to α = 90°, which is consistent with the flat-plate behavior assumed in the Viterna-Corrigan extrapolation. This behavior is important because, at very high angles of attack, the airfoil behaves more like a bluff body than an attached-flow lifting surface.

The final database was therefore obtained by combining the aerodynamic coefficients computed from the two-dimensional CFD simulations with the extrapolated values required to complete the full polar. The directly simulated CFD dataset provides the reference aerodynamic behavior in the available angle-of-attack range, while the extrapolated regions ensure that the ALM solver can always retrieve a defined value of (C_L) and (C_D) during the turbine rotation.

This complete database is essential for the low-TSR simulations, where the local angle of attack can reach values outside the directly simulated CFD range.

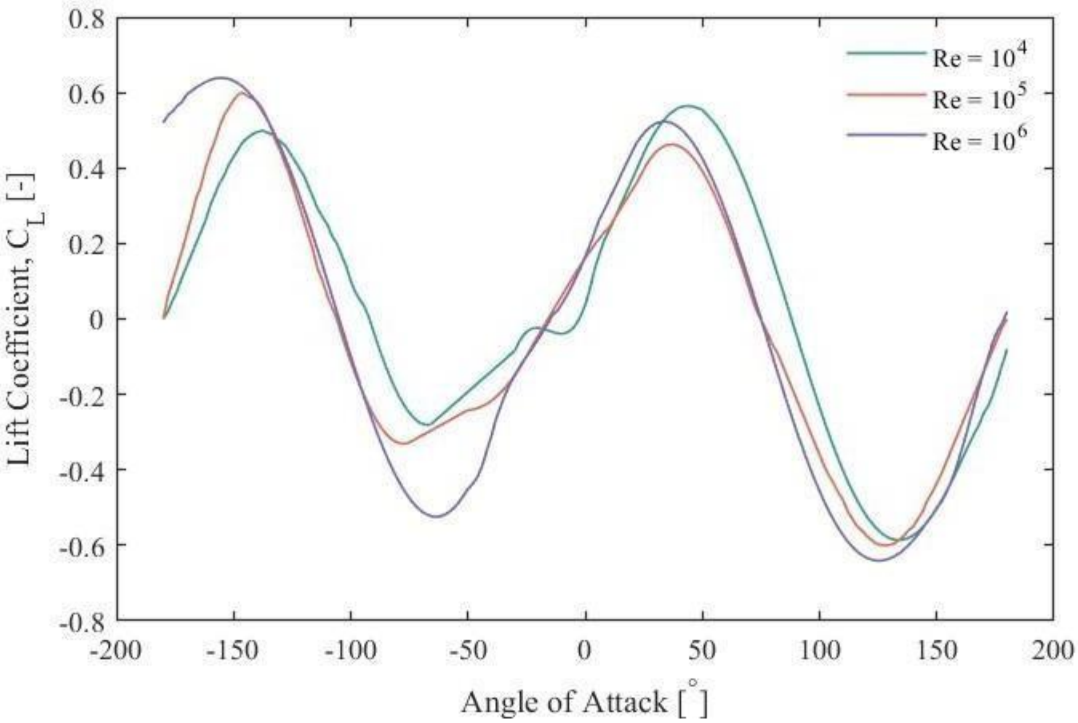

Figure 5-3: Final lift coefficient database used as ALM input for Reynolds numbers 10^4, 10^5 and 10^6 after Viterna-Corrigan extrapolation to the full angle-of-attack range

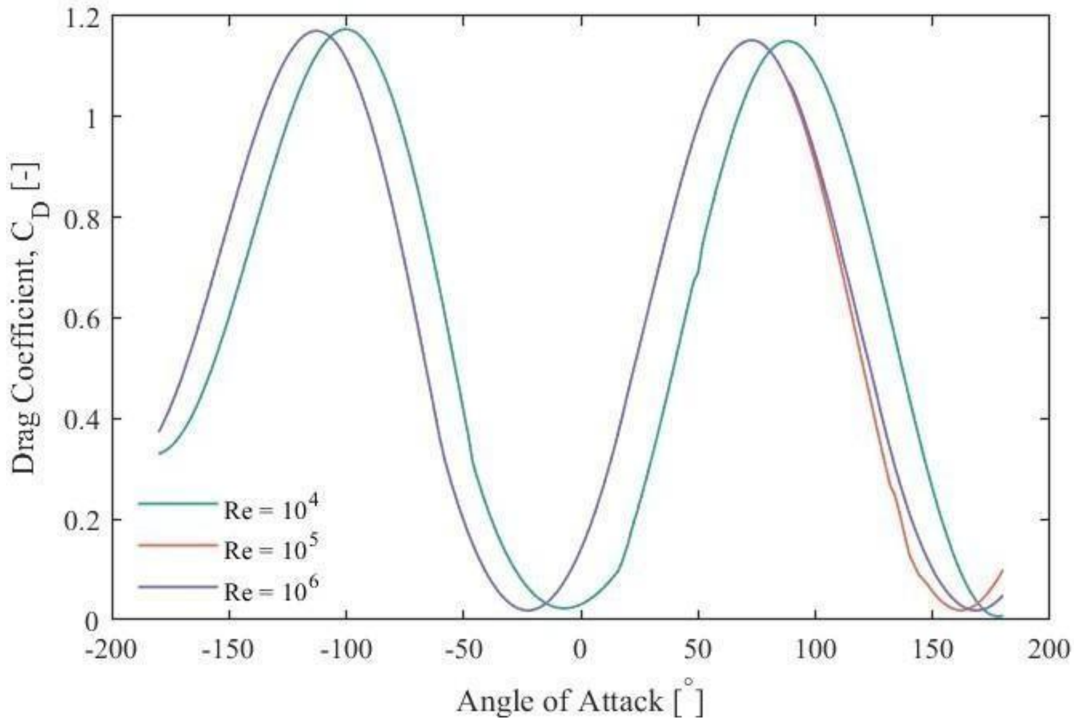

Figure 5-4: Final drag coefficient database used as ALM input for Reynolds numbers 10^4, 10^5 and 10^6 after Viterna-Corrigan extrapolation to the full angle-of-attack range

5.3. Numerical Setup in OpenFOAM/turbinesFoam

The actuator line simulations were performed in OpenFOAM using the turbinesFoam/crossFlowTurbine implementation. This section describes the numerical setup adopted to simulate the rotor at the selected low-TSR conditions. The setup includes the actuator line implementation, rotor geometry, computational domain, mesh, solver settings and post processing procedure used to extract the turbine power.

5.3.1. turbinesFoam/crossFlowTurbine implementation

The ALM was implemented using turbinesFoam, an open-source library developed for OpenFOAM by P. Bachant [31]. The library was designed to model both axial-flow and cross-flow turbines. In turbinesFoam, the aerodynamic forces calculated at the actuator elements are introduced into the OpenFOAM solver as a source term added to the governing equations. This allows the turbine loading to be coupled with the surrounding flow field without explicitly meshing the rotating blade surfaces.

In this work, the multiRe option was used. This option allows the ALM to read airfoil polar data for multiple Reynolds numbers instead of using a single fixed-Reynolds-number table. During the simulation, the local Reynolds number at each actuator element is evaluated from the local relative velocity, the blade chord and the fluid kinematic viscosity. The aerodynamic coefficients are then interpolated as a function of both angle of attack and Reynolds number.

This option is useful for the present low-TSR VAWT simulations because the local relative velocity, and therefore the local Reynolds number, varies during the blade revolution.

5.3.2. Rotor geometry and actuator line definition

The rotor geometry was defined in the fvOptions dictionary through the crossFlowTurbineALSourceCoeffs entry. This entry contains the main parameters required by turbinesFoam/crossFlowTurbine, including the rotor position, rotation axis, free stream velocity, rotor area, blade definition and aerodynamic profile assignment.

The actuator line model was applied to the Darrieus part of the vertical-axis wind turbine. The Savonius component of the original hybrid configuration was not included in the numerical model, since the objective of the present chapter is to evaluate the power prediction associated with the lift-based rotor at low tip speed ratios. The geometrical parameters assigned in the actuator-line setup reflect the main dimensions of the original turbine used in the experimental campaign, so that the numerical model preserves the rotor radius, blade height, chord length and number of blades of the physical system.

The rotor origin was defined at the point (0 0 0.45). The rotation axis was aligned with the z-direction and specified as axis (0 0 -1) in the fvOptions dictionary. The negative sign defines the orientation of the rotation axis used by the ALM and determines the sign convention for the rotor motion. The rotor radius was set equal to 0.25 m, while the free-stream velocity was imposed as (10 0 0), corresponding to a wind speed magnitude of 10 m/s in the x-direction.

The geometry of the first blade was defined through a set of spanwise reference points in the elementData list. Each row specifies the axial position of the actuator point, the rotor radius, the azimuthal position, the chord length, the chord-mounting position and the local pitch angle. The second and third blades were obtained from the same definition by applying azimuthal offsets of 120° and 240°, respectively.

Table 4reports the reference values used to define Blade 1. Although the actuator line was discretized into 18 elements, the blade geometry was prescribed using 10 reference points. These values were interpolated by turbinesFoam to generate the complete actuator-line discretization used during the simulation.

axialDistance [m]	**radius [m]**	**azimuth[°]**	**chord [m]**	**chordMount [-]**	**pitch [°]**
-0.4	0.25	157	0.19	0.5	-42
-0.311	0.25	149.5	0.19	0.5	-33.89
-0.222	0.25	142.1	0.19	0.5	-25.78
-0.133	0.25	134.6	0.19	0.5	-17.67
-0.044	0.25	123.2	0.19	0.5	-9.56
0.044	0.25	119.8	0.19	0.5	-1.44
0.133	0.25	112.4	0.19	0.5	6.67
0.222	0.25	104.9	0.19	0.5	14.78
0.311	0.25	97.5	0.19	0.5	22.89
0.4	0.25	90	0.19	0.5	31

Table 4: Reference values for blade 1

The axial distance varies from −0.40 m to +0.40 m, corresponding to the total blade height of 0.80 m. The rotor radius and chord length remain constant along the blade, while the azimuthal position and pitch angle vary along the span. The azimuthal position varies by approximately 67°, while the pitch angle varies by approximately 73° along the blade height. These relatively large variations indicate that the blade has a pronounced helical and twisted geometry, which must be included in the actuator-line definition in order to preserve the main geometrical characteristics of the original turbine.

5.3.3. Computational Domain, Mesh and Boundary Conditions

The computational domain was generated using the OpenFOAM blockMesh utility. A rectangular three-dimensional domain was defined with dimensions of 2m (8R) into the streamwise direction, 1m (4R) in the cross-stream direction and 1m (4R) in the vertical direction. The domain extends from x = - 1 m to x = + 1 m, from y = - 0.5 m to y = 0.5 m, and from z = 0 m to z = 1 m. The turbine was positioned inside this domain with the rotor origin located at (0 0 0.45), as defined in the fvOptions dictionary.

The base mesh was generated as a single structured hexahedral block with 32 × 32 × 24 cells and uniform grading in all directions. Since the actuator line method does not require the blade surfaces to be explicitly meshed, this structured background mesh provides the base discretization on which the actuator forces are later applied as source terms.

The incoming flow direction was aligned with the x-axis. Therefore, the inlet boundary was located at x = -1 m and the outlet boundary at x = 1 m. The free-stream velocity was imposed as 10 m/s in the x-direction, consistently with the velocity vector defined in the actuator-line setup.

The boundary patches were defined in the blockMeshDict as inlet, outlet, walls, top and bottom. The inlet and outlet were defined as patch boundaries, while the remaining external surfaces were defined as wall boundaries. The top and bottom faces correspond to the limits in the z-direction, while the lateral surfaces define the cross-stream limits of the computational domain.

After the base mesh generation, snappyHexMesh was used to refine the region surrounding the turbine. In the snappyHexMeshDict, a cylindrical geometry named turbine was defined with a radius of 0.30 m and extending from z = 0 m to z = 1 m. This cylinder represents the rotor swept region and is useful for identifying the physical area occupied by the rotating actuator lines. However, the active mesh refinement was applied through a larger box-shaped region named turb_zone, defined from (-0.55 -0.55 0) to (0.55 0.55 1). The cells inside this box were refined to level 2. Since the turbine cylinder is fully contained inside the turb_zone box, the rotor swept region is also refined to the same level. A visual qualitative representation can be seen in Figure 5-5.

The use of the larger refinement box ensures that not only the blade path, but also the surrounding cells affected by the actuator-force projection, are refined. This is important in ALM simulations because the aerodynamic forces are distributed from the actuator elements to the nearby computational cells rather than applied at a single point. The refined box therefore provides a buffer region around the rotor, improving the resolution of the force projection while avoiding refinement of the entire computational domain.

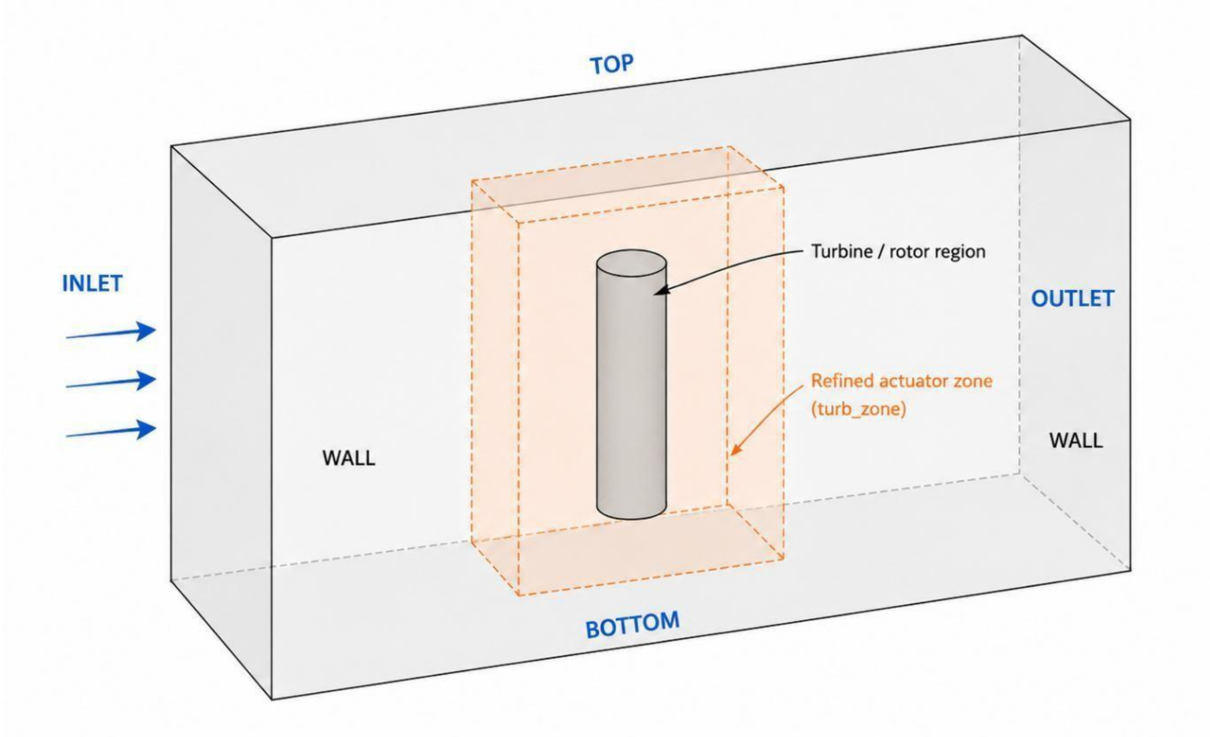

Figure 5-5:Three-dimensional representation of the computational domain and actuator refinement region

5.3.4. Solver and Numerical Schemes

The transient flow field was solved using pimpleFoam because the AL rotates inside the computational domain and the aerodynamic loading changes continuously with the azimuthal position of the blades. As a consequence, the torque and power predicted by the ALM are quantities that depend on time and therefore must be evaluated during the rotor motion. At each time step, the crossFlowTurbine model updates the blade-element positions, evaluates the local velocity and angle of attack, calculates the aerodynamic forces from the airfoil database, and applies the resulting force distribution to the flow field.

The simulations were performed over a transient time interval using an adjustable time step. The time-step control was based on the Courant number, which was limited to a maximum value of 0.2 in order to maintain numerical stability during the rotation of the actuator lines. This strategy allowed the solver to automatically reduce or increase the time step depending on the local flow conditions, while keeping the transient solution stable. The same time-step control settings were used for all simulated operating conditions.

The pressure–velocity coupling was handled using the PIMPLE algorithm. The standard correction settings adopted in the case setup were maintained, with one outer corrector, two pressure correctors and no non-orthogonal correctors. The same settings were used for all simulated tip speed ratios, ensuring that the comparison between cases was not affected by changes in the pressure–velocity coupling procedure.

The flow was modelled using a Reynolds-averaged turbulence approach. The simulation type was set to RAS, and the selected turbulence model was k-ω SST. This choice is consistent with the two-dimensional airfoil simulations presented in Chapter 4, where the combination of pimpleFoam and the k-ω SST turbulence model provided the most suitable results for the reconstructed blade profile. For this reason, the same solver and turbulence-model combination was adopted in the actuator line simulations in order to maintain consistency between the aerodynamic database generation and the rotor-level ALM calculations.

The discretization schemes were defined in the fvSchemes dictionary. A first-order Euler scheme was used for the temporal derivative, while Gauss-based finite volume schemes were used for the spatial terms. The convective term in the velocity equation was treated with a bounded linear-upwind scheme, while the turbulence quantities were discretized using upwind schemes. Limited corrected schemes were used for the Laplacian and surface-normal gradient terms in order to improve stability on the refined mesh.

The linear solver settings were defined in the fvSolution dictionary. The pressure equation was solved using a GAMG solver, while the velocity and turbulence equations were solved using a smooth solver with a Gauss-Seidel smoother. Relaxation factors were applied to improve numerical stability during the transient calculations.

The same solver settings and numerical schemes were used for all simulated low-TSR cases. Therefore, differences in the predicted torque and power are associated with the imposed operating condition and the actuator-line response rather than with changes in the numerical discretization.

5.3.5. Simulated Low TSR Cases

The operating conditions of the ALM simulations were defined in terms of tip speed ratio, already introduced in Chapter 2. In the present chapter, the TSR is used only as the input parameter controlling the imposed angular velocity of the rotor.

The simulations were performed in the low TSR range from 0.4 to 1.0, with an increment of 0.1. This range was chosen because the experimental turbine operates mainly at low rotational speeds, and the objective of the numerical model is to evaluate the power prediction in this operating region rather than to investigate high-TSR performance.

The free-stream velocity was kept constant at 10 m/s for all simulations. The different operating conditions were obtained by changing the prescribed tip speed ratio in the fvOptions dictionary. Since the rotor radius was fixed at 0.25 m, each value of tip speed ratio defines the corresponding rotational speed used internally by turbinesFoam.

5.3.6. Power Extraction and Time Averaging

In turbinesFoam, the time dependent aerodynamic quantities were written using the writePerf option activated for the blades. In addition, writeElementPerf was enabled in order to store the contribution of the individual actuator elements. This output makes it possible to analyze both the global rotor performance and the spanwise distribution of the aerodynamic loading. However, in the present work, the main quantity of interest is the rotor-level power prediction at low tip speed ratios.

The instantaneous torque obtained from the actuator-line forces was converted into mechanical power using the definition introduced in Chapter 2:

$$P = T\omega \tag{5.15}$$

where P is the mechanical power, T is the rotor torque and ω is the imposed angular velocity. The corresponding power coefficient was then calculated by normalizing the mechanical power with respect to the available wind power:

$$C_P = \frac{P}{\frac{1}{2}\rho A U_\infty^3} \tag{5.16}$$

where ρ is the air density, A is the rotor swept area and U_∞ is the free-stream velocity.

Since the instantaneous power varies during the rotor motion, a time-averaged value was computed for each operating condition. The initial part of the simulation was excluded from the averaging procedure in order to reduce the influence of the start-up transient. The mean torque, power and power coefficient were then evaluated over the selected quasi-periodic portion of the simulation.

This averaging procedure allows the unsteady AL output to be converted into a representative mean power coefficient for each simulated tip speed ratio. The resulting mean values are used in Section 5.5 to construct the numerical C_P-TSR curve and to evaluate the power prediction of the ALM model in the low-TSR operating range.

5.4. Dynamic Stall

Dynamic stall is one of the most relevant aerodynamic phenomena affecting the present actuator line simulations. This is because the numerical study focuses on the low tip speed ratio operating range, where the blades of a vertical-axis wind turbine experience large cyclic variations of relative velocity and angle of attack during each revolution. Under these conditions, the blade sections may exceed the static stall angle for part of the rotation, so the aerodynamic loads cannot be described only by steady airfoil coefficients [34].

Melani et al. [35] highlight that VAWT blades are characterized by an unsteady aerodynamic behavior due to their cycloidal motion. In particular, the continuous variation of angle of attack makes the estimation of airfoil performance difficult, especially when the blade operates in post-stall conditions. This is directly relevant for the present work, where the simulated TSR range is intentionally limited to low values.

The objective of this section is therefore to describe why dynamic stall is relevant for the present simulations and how it is treated in the numerical model. First, the physical mechanism of dynamic stall in VAWTs is introduced. Then, its importance at low TSR is discussed. Finally, the dynamic stall implementation in turbinesFoam and the main limitations of this correction are presented.

5.4.1. Dynamic Stall in VAWT and Relevance at Low TSR

Dynamic stall occurs when an airfoil is subjected to an unsteady variation of angle of attack and exceeds the static stall limit. In steady conditions, stall is usually associated with flow separation and a reduction of lift after the static stall angle is reached. In dynamic conditions, however, the separation process is delayed, and the airfoil can temporarily reach higher angles of attack before massive separation occurs [36].

Mulleners and Raffel [36] describe dynamic stall as a process characterized by delayed massive separation and by the formation of a large-scale dynamic stall vortex. The development of dynamic stall is commonly described through a sequence of flow stages. At first, the flow remains attached while the angle of attack increases. Then, flow reversal begins to appear near the airfoil surface, followed by the development of a separated shear layer. As the instability of this shear layer grows, it rolls up into a coherent vortical structure, known as the dynamic stall vortex. After this vortex detaches and is shed into the wake, the airfoil enters a fully stalled state, followed eventually by flow reattachment during the recovery part of the motion.

Mulleners and Raffel [36] also emphasize the importance of the shear layer in the development of the dynamic stall vortex. According to their analysis, the primary dynamic stall vortex originates from the growth of a recirculation region and from the instability of the associated shear layer. This is important because vortex formation is not instantaneous; it depends on the previous flow history and on the characteristic time scales of the unsteady separation process.

For a vertical-axis wind turbine, dynamic stall is more complex than for a single pitching airfoil. A VAWT blade does not oscillate around a fixed mean angle of attack. Instead, it moves along a circular trajectory, and the relative velocity experienced by the blade results from the combination of the incoming wind velocity and the rotational velocity of the blade. Therefore, the angle of attack varies continuously with the azimuthal position during each revolution.

Dyachuk and Goude [37] explain that simulation models for VAWTs must account for the continuous variation of angle of attack, since this is a natural feature of vertical-axis turbine operation. They also state that the amplitude of the angle-of-attack variation increases as the tip speed ratio decreases, and that dynamic stall is present at low TSR. This means that dynamic stall is not an exceptional condition for VAWTs, but a recurring aerodynamic phenomenon when the turbine operates in the low-TSR range.

The dynamic stall process affects both the local blade forces and the global turbine performance. During the formation and convection of the dynamic stall vortex, the blade may experience a temporary increase in lift. However, after vortex shedding, the flow can become deeply separated, producing a rapid variation of the aerodynamic forces. For a VAWT, this affects the tangential force responsible for torque generation, as well as the normal force associated mainly with structural loading. Therefore, dynamic stall contributes to torque oscillations, fatigue loading and uncertainty in power prediction.

Castelein et al. [38] specifically studied a VAWT in dynamic stall in order to create experimental benchmark data for numerical model validation. Their work compares two tip speed ratios, with the lower TSR used to identify dynamic stall effects and the higher TSR representing a condition where dynamic stall is not dominant. This distinction shows that dynamic stall in VAWTs is strongly connected to the operating condition and that low-TSR cases are particularly important for numerical validation.

This behavior is important for the present thesis because the actuator line simulations are focused on power prediction at low TSR. The simulated range, from TSR = 0.4 to TSR = 1.0, corresponds to an operating condition in which large angle-of-attack variations are expected. Even though the detailed vortex dynamics are not analyzed, the aerodynamic forces computed at the actuator elements are directly influenced by whether the model can represent the unsteady response of the blade sections.

Therefore, dynamic stall must be considered in the ALM setup in order to obtain a more physically consistent prediction of torque and power. In this thesis, the dynamic stall correction is not used to validate the detailed vortex formation and shedding process, but to improve the aerodynamic force calculation in the operating range where the turbine is expected to be most affected by unsteady stall effects.

In summary, dynamic stall in a VAWT is the result of the cyclic and unsteady aerodynamic environment experienced by the rotating blades. It involves delayed separation, vortex formation, vortex shedding and reattachment, and its effect is particularly significant at low tip speed ratios. For this reason, the dynamic stall correction was included in the ALM setup to improve the force prediction in the low-TSR operating range.

5.4.2. Dynamic Stall Implementation in turbinesFoam

In the present simulation dynamic stall was activated in the airfoil model definition used by turbinesFoam. The selected model was LeishmanBeddoesSGC, which belongs to the Leishman–Beddoes family of semi-empirical dynamic stall models. This type of model is commonly used because it allows unsteady aerodynamic effects to be included in blade-element or actuator-line calculations without explicitly resolving the boundary layer and the separated vortex structures around the blade surface [37].

Bachant, Goude and Wosnik implemented a Leishman–Beddoes-type dynamic stall model in their actuator line formulation for cross flow turbines. They explain that cross flow turbine blades experience unsteady conditions in both angle of attack and relative velocity, and that the encountered angles of attack can be high enough to require dynamic stall modelling. In their implementation, the dynamic stall model is used to augment the static airfoil characteristics and improve the prediction of unsteady blade loading [31].

The Leishman–Beddoes approach is based on the idea that the aerodynamic response of an airfoil under unsteady conditions does not depend only on the instantaneous angle of attack. Instead, it also depends on the previous aerodynamic state of the section. For this reason, the model introduces time-lag effects associated with unsteady attached flow, pressure response, boundary-layer development, flow separation and leading-edge vortex effects [39].

In turbinesFoam, the dynamic stall correction is applied at the actuator-element level. At every time step, the local velocity field is sampled at the actuator element, the relative velocity and angle of attack are evaluated, and the static aerodynamic coefficients are obtained from the prescribed airfoil database. The dynamic stall model then modifies the aerodynamic response in order to account for unsteady effects before the resulting forces are projected onto the CFD mesh as momentum source terms.

The dynamic stall setup used in this work is reported in the dynamicStall sub-dictionary of the airfoil model. The model was activated by setting active on, and the selected model was defined as LeishmanBeddoesSGC. The main coefficients used in the simulations are summarized in Table 5: Dynamic stall parameters used in the LeishmanBeddoesSGC model. These parameters control the characteristic time delays and empirical constants associated with pressure lag, boundary-layer response, stall onset and vortex convection.

Parameter	**Value**
Tp	2.5
Tf	6

TAlpha	3
alphaDS0DiffDeg	12
r0	0.02
Tv	8
Tvl	6
B1	0.5
eta	0.7
E0	0.12
ReList	1e6
CNAlphaList	2
CD0List	0.06
CN1List	1.4
alpha1List	14
S1List	0.8
S2List	1.2

Table 5: Dynamic stall parameters used in the LeishmanBeddoesSGC model

The parameters Tp, Tf and TAlpha control the time delay associated with the unsteady aerodynamic response. In particular, these constants influence how quickly the model responds to changes in angle of attack and flow separation. The parameters Tv and Tvl are associated with the vortex contribution, including vortex lift decay and convection over the airfoil. These terms are important because the leading-edge vortex is one of the main features responsible for the load overshoot observed during dynamic stall [39].

The parameters CNAlphaList, CD0List, CN1List, alpha1List, S1List and S2List define airfoil-dependent quantities used by the dynamic stall formulation. These values are related to the static normal-force slope, the drag level, the critical normal-force coefficient and the curve used to represent the separation-point behavior. Since the present blade profile is not a standard airfoil, these parameters were adjusted in order to obtain a stable and physically reasonable dynamic stall response for the reconstructed blade geometry.

In this setup, the dynamic stall parameter list was defined for ReList = 1e6. Therefore, while the static aerodynamic database described in Section 5.2 was prepared for multiple Reynolds numbers, the dynamic stall correction itself used one parameter set.

This means that the static lift and drag coefficients could vary with the local Reynolds number, whereas the empirical dynamic stall constants were kept fixed. This is an important modelling choice and should be considered when interpreting the final power predictions.

The use of the Leishman–Beddoes-type model is appropriate for the present work because the simulations are focused on low-TSR conditions, where large angle-of-attack variations and unsteady separation are expected. However, the model should be interpreted as an engineering correction rather than as a direct resolution of the dynamic stall vortex. The objective is to improve the actuator-line force calculation and the resulting prediction of torque and power, not to reproduce the detailed separated-flow structure around the blade.

5.4.3. Limitations of the Dynamic Stall Correction

Although the dynamic stall correction is necessary for the present low-TSR simulations, it must be interpreted as an engineering model rather than as a complete physical resolution of the stall process. The Leishman–Beddoes-type model used in turbinesFoam is semi-empirical, meaning that it represents the main effects of unsteady aerodynamics through simplified equations and calibration parameters. These parameters control phenomena such as pressure lag, separation delay, vortex formation and vortex convection, but they do not directly resolve the boundary layer or the dynamic stall vortex around the blade surface [37].

The first limitation is related to the calibration of the model parameters. Melani et al. point out that the implementation and calibration of Beddoes–Leishman-type models are still affected by uncertainty, especially because many parameters depend on the airfoil shape, Reynolds number and operating conditions. In the present thesis, this issue is particularly important because the blade profile is not a standard NACA airfoil, but a reconstructed and strongly cambered section. Therefore, the dynamic stall parameters available in the literature may not perfectly describe the unsteady aerodynamic behavior of the actual blade [40].

A second limitation concerns the dimensionality of the phenomenon. Dynamic stall is often introduced using two-dimensional airfoil concepts, but recent studies have shown that the process can have a strongly three-dimensional nature. Khalifa et al. show that three-dimensional simulations are more capable than two-dimensional simulations of capturing the stages of dynamic stall and the associated lift behavior. This means that a sectional dynamic stall correction can reproduce the main influence on the aerodynamic coefficients, but it cannot fully represent the three-dimensional separated-flow structures that may develop on a real rotating blade [41].

Another limitation is associated with the actuator line formulation itself. In ALM simulations, the local angle of attack is not obtained from a resolved blade surface, but from the velocity field sampled near the actuator element. Melani et al. highlight that, for VAWT ALM simulations, the sampled angle-of-attack signal can be affected by numerical noise, local disturbances and previously shed vortices. This is especially relevant for dynamic stall models because they depend on the time history of the aerodynamic state, and any disturbance in the AoA signal may influence the predicted unsteady loads.

The dynamic stall correction also depends on the quality of the static aerodynamic database used as input. In the present work, the aerodynamic database was obtained by combining two-dimensional CFD results with Viterna-Corrigan extrapolation in order to cover the full angle-of-attack range from -180° to +180°. Since the dynamic stall model acts on this database, uncertainties in the static lift and drag coefficients, especially in the post-stall and deep-stall regions, can propagate into the corrected unsteady forces. This is particularly important at low TSR, where the actuator elements may frequently operate far outside the attached-flow range.

An additional modelling limitation is that the static aerodynamic database was prepared using the multiRe option, while the dynamic stall parameter set was defined for a single Reynolds number. As a result, the static aerodynamic coefficients can vary with the local Reynolds number, but the empirical constants of the dynamic stall model remain fixed. This simplification was adopted to obtain a stable and usable numerical setup, but it may reduce the accuracy of the unsteady correction when the local Reynolds number changes significantly during the rotor revolution.

Finally, the validation performed in this thesis is based mainly on rotor-level power prediction. The comparison with experimental data is therefore focused on the mean power coefficient, not on phase-resolved blade loads or detailed vortex structures. A dynamic stall model may improve the predicted mean Cp while still producing errors in the instantaneous torque waveform or in the timing of the aerodynamic loads. For this reason, the results must be interpreted as a power-performance validation of the ALM setup, rather than as a complete validation of the dynamic stall physics.

In summary, the dynamic stall correction is essential for the present simulations because the turbine operates in a low-TSR range where large angle-of-attack variations are expected. However, the correction introduces uncertainty related to model calibration, non-standard blade geometry, angle-of-attack sampling, Reynolds-number dependence and the simplified actuator-line representation. These limitations must be considered when discussing the final Cp–TSR results.

5.5. ALM Results

This section presents the results obtained from the actuator line simulations performed with turbinesFoam/crossFlowTurbine. The analysis focuses on the prediction of rotor power in the low tip speed ratio range, from TSR = 0.4 to TSR = 1.0. This range was selected because it corresponds to the operating region of interest for the experimental turbine.

The main quantity analyzed is the power coefficient, Cp, obtained from the time-averaged torque predicted by the ALM. Attention is given to the numerical trend of the predicted power coefficient, the effect of the dynamic stall correction, and the interpretation of the aerodynamic behavior obtained from the ALM simulations.

At this stage, the results are discussed only in terms of the numerical model. The comparison with wind tunnel measurements is introduced later, after the experimental post processing procedure and the corresponding experimental power coefficient data have been processed.

5.5.1. Numerical Power Coefficient Curve

Figure 5-6 shows the power coefficient predicted by the ALM simulations as a function of tip speed ratio. The simulations were performed in the low-TSR range, from TSR = 0.4 to TSR = 1.0. The curve shows that the model predicts positive power production for the lower part of the investigated range, with the maximum value occurring around TSR
= 0.5.

The predicted power coefficient is approximately constant between TSR = 0.4 and TSR = 0.5, with values close to C_P = 0.16. After this point, the power coefficient progressively decreases as the tip speed ratio increases. At TSR = 0.6, the predicted C_P is still positive but lower than the maximum value. The decrease continues for TSR = 0.7 and TSR = 0.8, and the curve approaches zero around TSR = 0.9.

At TSR = 1.0, the ALM predicts a negative value of C_P. This means that, for this operating condition, the mean aerodynamic torque has the opposite sign with respect to the imposed direction of rotation. In other words, the rotor is no longer producing useful power in the numerical model but is instead extracting mechanical energy from the imposed rotation.

The overall trend indicates that, according to the ALM prediction, the turbine operates more effectively at very low tip speed ratios, with the best numerical performance around TSR = 0.4–0.5. The reduction of C_P at higher TSR suggests that the aerodynamic force distribution becomes less favorable for torque production as the rotational speed increases. This behavior is consistent with the highly non-standard blade geometry and with the strong 3D orientation of the blade, which may cause different spanwise sections to operate under different aerodynamic conditions during the same revolution.

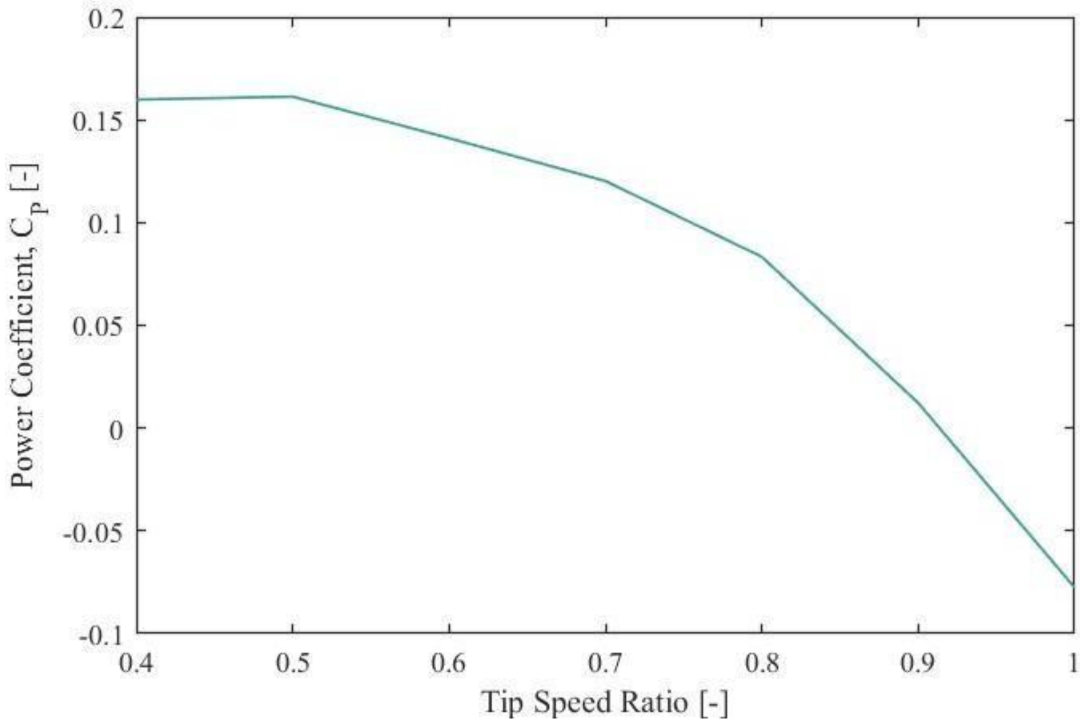

Figure 5-6: Power coefficient predicted by the ALM simulations as a function of tip speed ratio

5.5.2. Influence of Dynamic Stall on Power Prediction

The influence of the dynamic stall correction was evaluated by comparing the numerical behavior of the ALM with and without the dynamic stall model activated. This comparison is important because the simulated operating range is characterized by low tip speed ratios, where the blade sections experience large cyclic variations of angle of attack during each revolution. Dyachuk and Goude [37] state that, for VAWTs, the amplitude of the AoA variation increases as TSR decreases, and that dynamic stall is present at low TSR. Therefore, the activation of a dynamic stall model is expected to have a significant influence on the predicted blade forces and rotor power.

When the dynamic stall correction was deactivated, the ALM predicted negative values of the power coefficient in the investigated low-TSR range. This indicates that the quasi-steady aerodynamic response alone was not able to generate a positive mean torque for the imposed direction of rotation. In this case, the static polar database produced an aerodynamic force distribution that opposed the rotor motion on average, leading to negative power production.

This result suggests that, for the present turbine, unsteady stall effects play an essential role in the generation of useful torque at low TSR. The dynamic stall model introduces effects such as stall delay and vortex-induced load variation, which can increase the tangential force during part of the rotor revolution. Without this correction, the model relies only on the static aerodynamic database and may fail to represent the transient aerodynamic contribution associated with dynamic stall. This is consistent with the observations of Persico et al. [34], who identify dynamic stall as one of the main sources of uncertainty in VAWT performance prediction because of its influence on power coefficient and torque exchange.

However, the activation of the dynamic stall correction does not eliminate all numerical limitations. Although the model allows positive power prediction over most of the investigated range, the Cp curve still decreases as TSR increases and becomes negative at TSR = 1.0. This indicates that, even with dynamic stall activated, the aerodynamic force distribution predicted by the ALM becomes progressively less favorable for power production at the upper end of the investigated range.

The sensitivity of the predicted power to the dynamic stall correction confirms that the low TSR behavior of the turbine is governed by highly unsteady aerodynamics. At the same time, the result must be interpreted with caution. Melani et al. [35] highlight that implementing dynamic stall models in ALM simulations of VAWTs is challenging because the AoA signal is obtained from the resolved CFD field and can be affected by numerical disturbances. Therefore, the dynamic stall correction is essential for the present setup, but it remains a semi-empirical modelling component whose parameters and input data influence the final power prediction.

5.5.3. Interpretation of the Low TSR ALM Behavior

The ALM results show that the predicted power coefficient reaches its maximum in the lower part of the TSR range investigated and then decreases progressively as TSR increases. Since the inlet velocity, rotor geometry, mesh and solver settings were kept constant for all cases, the variation of Cp is mainly associated with the change in operating condition. In particular, the imposed TSR modifies the blade relative velocity, the AoA history and the resulting dynamic stall response.

The dynamic stall correction appears to be essential for the present operating range because it allows the model to include delayed separation and vortex-induced load variations. These effects can temporarily increase the aerodynamic loading during part of the blade revolution and improve the tangential force contribution. Therefore, the positive Cp values predicted between TSR = 0.4 and TSR = 0.9 should not be interpreted as the result of purely steady airfoil behavior, but as the combined effect of the static aerodynamic database and the dynamic stall correction.

The progressive decrease of Cp with increasing TSR suggests that the phase and direction of the aerodynamic forces become less favorable for power production. In a VAWT, useful power depends on the tangential component of the aerodynamic force, not only on the magnitude of lift. Therefore, even if the blade sections generate significant aerodynamic loads, these loads may not always contribute positively to torque. At some azimuthal positions, or along some spanwise sections, the force component may be weak, poorly aligned with the direction of rotation, or even opposite to the imposed motion.

This aspect is particularly important for the present turbine because the blade has a strongly three-dimensional geometry, with large spanwise variations of azimuthal position and pitch angle. As discussed in Section 5.3.2, the blade geometry is characterized by a pronounced helical and twisted configuration. Therefore, different blade sections do not necessarily operate under the same local aerodynamic conditions at the same azimuthal position. Some sections may contribute positively to torque while others may produce reduced or opposing tangential force, limiting the mean power extracted by the rotor.

The negative Cp predicted at TSR = 1.0 indicates that, according to the ALM model, the mean aerodynamic torque becomes opposite to the imposed direction of rotation. This does not necessarily mean that the instantaneous torque is negative during the entire revolution. Rather, it means that, after time averaging, the negative torque contributions exceed the positive ones. In this condition, the numerical model predicts that the rotor would require mechanical input to maintain the imposed rotational speed instead of producing useful power.

The magnitude of the predicted power coefficient is also relatively low when compared with other lift-based VAWT cases reported in the literature. In the present ALM simulations, the maximum predicted Cp is approximately 0.16. Other Darrieus and H-rotor studies report higher optimal values; for example, Alqurashi and Mohamed [42] discuss previous H-rotor configurations with optimal power coefficients around 0.36. This comparison suggests that the present rotor has a lower aerodynamic efficiency than more conventional or optimized Darrieus-type turbines.

However, this comparison must be interpreted with caution because the operating conditions are not equivalent. Most published VAWT studies focus on operating regions closer to the usual peak-efficiency range of lift-based Darrieus turbines, often at TSR values around 2 or higher. For example, Castelein et al. [38] investigated a low-TSR dynamic-stall case at TSR = 2 and a higher-TSR case at TSR = 4.5, while Persico et al. [34] analyzed a small H-shaped VAWT around TSR = 2.4. In contrast, the present ALM simulations are restricted to TSR = 0.4–1.0, which is substantially lower than the range most commonly reported in the literature.

Therefore, the relatively low Cp values predicted in this work should be interpreted within the context of a very low TSR regime. In this range, dynamic stall, deep separation and unfavorable force orientation are expected to have a stronger influence on the mean power output. The scarcity of directly comparable literature data at TSR values below 1 also makes it difficult to determine whether the predicted trend is mainly a numerical limitation, a consequence of the specific rotor geometry, or a combination of both.

Another possible explanation for the decreasing trend is the non-standard aerodynamic character of the reconstructed blade profile. The airfoil used in the ALM database is strongly cambered and differs from conventional Darrieus turbine profiles.

This may lead to asymmetric aerodynamic behavior between positive and negative angles of attack and to a force distribution that is not optimal for lift-based power extraction. Since the turbine geometry was reconstructed from an existing physical prototype rather than designed through an aerodynamic optimization procedure, the ALM results may reflect the limited aerodynamic efficiency of the original blade configuration.

The predicted behavior also confirms the sensitivity of ALM simulations to the aerodynamic database and to the dynamic stall model. Melani et al. [35] highlight that ALM simulations of VAWTs are sensitive to the sampling of the angle of attack and to the implementation of dynamic stall models, because the force calculation depends on local flow quantities extracted from the resolved CFD field. In the present case, the predicted reduction of Cp at higher TSR may therefore be influenced not only by the physical behavior of the rotor, but also by modelling choices such as the dynamic stall parameters, the static polar extrapolation and the actuator-line representation of the blade.

Overall, the low-TSR ALM behavior suggests that the turbine can generate positive power only in a limited portion of the investigated operating range. The predicted maximum occurs around TSR = 0.4–0.5, followed by a continuous reduction of Cp and a negative value at TSR = 1.0. This trend indicates that the numerical model is highly sensitive to unsteady aerodynamic effects and to the orientation of the blade forces. Therefore, the results should be interpreted as a low-TSR power prediction for a non-standard VAWT geometry, rather than as the performance curve of an optimized Darrieus turbine.

5.5.4. Pressure-Field Visualization

The sequence highlights the unsteady character of the ALM solution. During the rotation, regions of lower pressure develop and move around the rotor, while higher-pressure regions appear downstream and around the actuator zone. This behavior is consistent with the periodic variation of aerodynamic loading expected in a vertical-axis wind turbine, where the blades continuously experience changing relative velocity and angle of attack. The alternating low- and high-pressure regions indicate that the rotor does not interact with the flow in a steady manner but produces a time-dependent disturbance that evolves during the rotation.

Figure 5-7 shows nine pressure-field snapshots obtained during a partial rotor rotation. The frames are ordered from left to right and from top to bottom, and the same pressure scale is used for all images, ranging from approximately −11 Pa to 35 Pa.

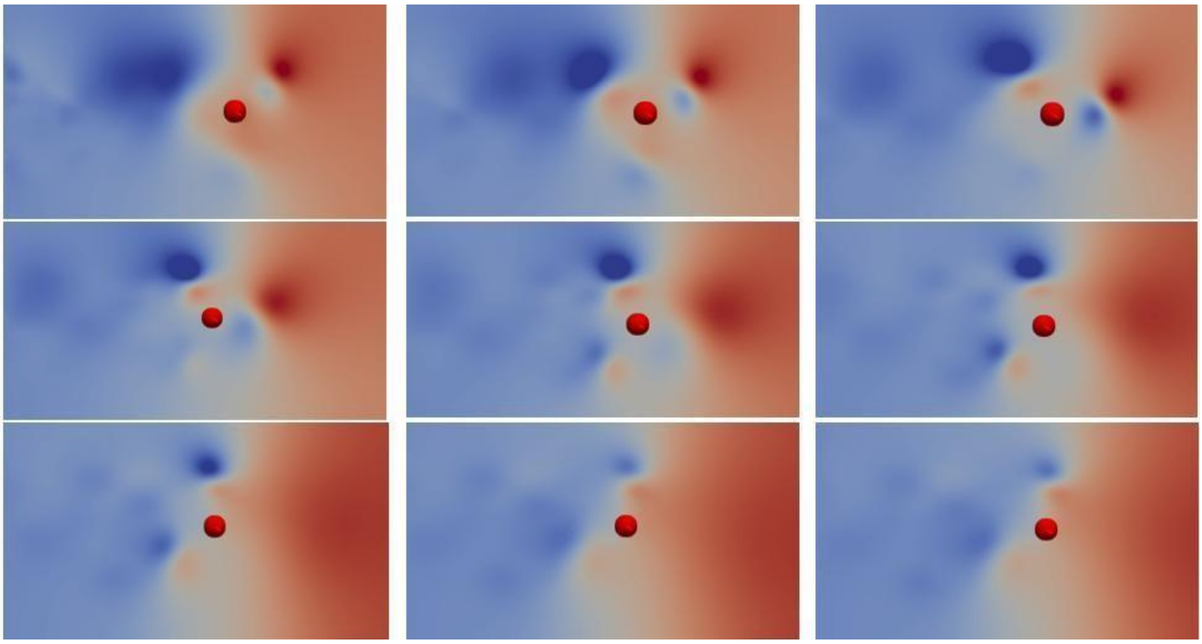

Figure 5-7: Pressure-field visualization from the ALM simulation over a partial rotor rotation

6 Wind Tunnel Experiment

This chapter presents the wind tunnel experiment carried out to obtain the experimental performance curve of the vertical-axis wind turbine. The objective of the experiment was to measure the mechanical response of the rotor under controlled flow conditions and to derive the power coefficient as a function of the tip speed ratio. These data are used as the experimental reference for the validation of the actuator line model presented in Chapter 5.

6.1. Experimental Setup

The experimental procedure was designed to cover the low tip speed ratio range investigated numerically. For this reason, two approaches were considered for the torque estimation. The first approach uses the resisting torque imposed by the mechanical brake, while the second estimates the torque from the rotor dynamics measured by the encoder. The use of both methods allows a broader reconstruction of the operating curve, since the brake-based measurements provide controlled loading conditions, whereas the encoder-based approach makes it possible to analyze the rotor response during transient acceleration or deceleration phases. In this way, the experimental campaign attempts to cover the widest possible range of TSR values for comparison with the numerical simulations.

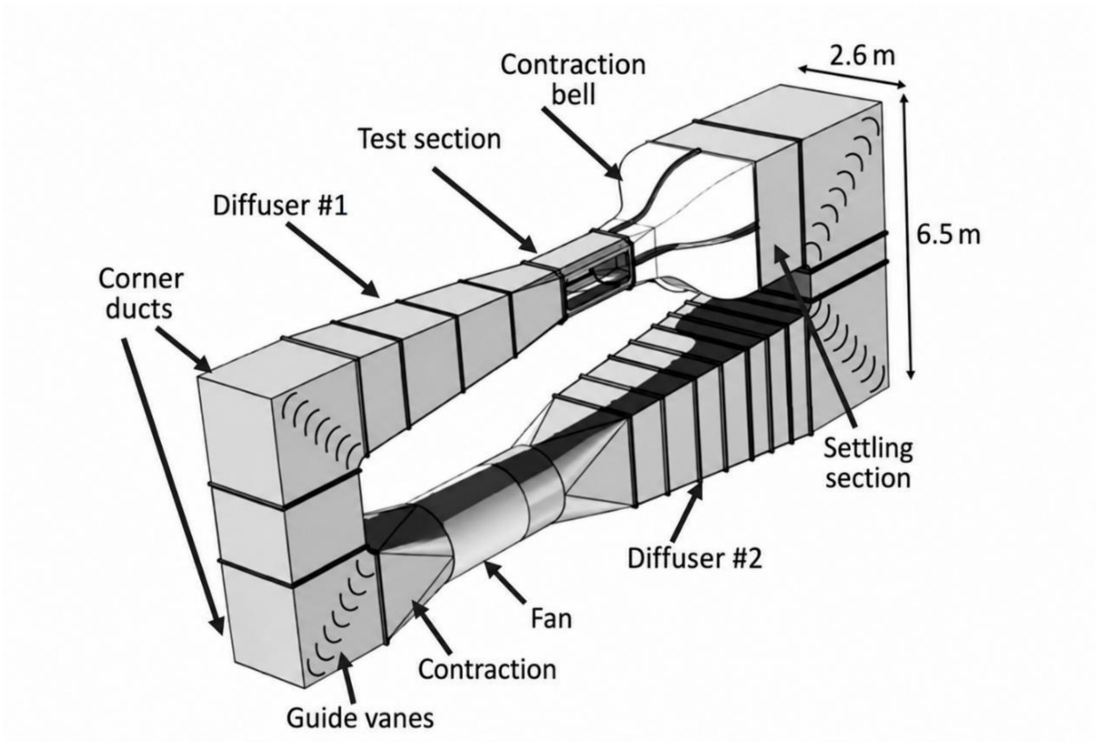

Figure 6-1: Wind tunnel TVIM-49-60-1x1

The experiment was performed using the wind tunnel infrastructure of the University of the Andes (Figure 6-1) and the turbine support system previously developed by Molano Otálora [43] for the characterization of the same commercial small-scale hybrid Savonius-Darrieus turbine. In the previous work, the complete turbine was adapted for wind tunnel testing through the redesign of the support structure and the replacement of the original generator with an external braking system. The present thesis continues from that experimental basis but focuses only on the Darrieus part of the turbine, consistently with the actuator line model implemented in Chapter 5.

The test section has dimensions of 1 m x 2 m x 1 m (Figure 6-2), which allowed the installation of the small-scale VAWT inside the flow region. During the experiment, the incoming flow was directed horizontally across the rotor, while the turbine rotational axis was aligned vertically.

Figure 6-2: Test section

6.2. Instrumentation

After the complete installation of the turbine inside the wind tunnel, the experimental procedure was carried out using the instrumentation previously implemented for the mechanical characterization of the turbine. This instrumentation allowed the measurement of the flow conditions, the rotational response of the rotor, and the resisting torque applied during the tests.

Before each measurement, the wind tunnel velocity was adjusted to the desired value, and the flow was allowed to stabilize for a sufficient period of time. This step was necessary to ensure that the turbine operated under approximately steady and repeatable inflow conditions. Once the flow was stabilized, the air properties inside the test section were recorded.

The atmospheric properties were measured using a Vaisala PTB330TS barometer, which provided the pressure, temperature, and relative humidity of the air inside the wind tunnel. These quantities were required to determine the air density, which is necessary for the calculation of the available wind power and the power coefficient. The free-stream velocity was measured using an Extech AN100 CFM/CMM thermo-anemometer. This value was used as the reference velocity for the calculation of the tip speed ratio and the aerodynamic power available in the flow.

The rotational speed of the turbine shaft was measured using an Extech RPM10 optical tachometer. In order to obtain a stable optical signal, a portion of the rotating shaft was covered with black tape, and a reflective strip was placed on the surface. This contrast allowed the tachometer to detect each revolution of the shaft and provide the rotational speed in revolutions per minute. The measured RPM was later converted into angular velocity during the data processing stage.

The mechanical loading system consisted of a hysteresis brake connected to the lower part of the turbine shaft. The brake was used to apply controlled loading conditions during the experiment and to obtain different operating points of the rotor. The torque associated with each braking condition was obtained from the brake calibration curve, as described in Section 6.3.1.

In addition to the brake-based method, an encoder connected to an Arduino-based data acquisition system was used as a complementary method to estimate torque from the rotor motion. The encoder recorded the angular position of the rotor as a function of time, allowing the angular velocity and angular acceleration to be obtained during post-processing. This method is introduced briefly here and described in more detail in Section 6.3.2.

The experimental procedure was repeated for the operating conditions considered in this work. In this way, the instrumentation provided the necessary information to calculate angular velocity, torque, mechanical power, tip speed ratio, and power coefficient. These quantities were then used to construct the experimental performance curve of the Darrieus rotor and to compare it with the numerical actuator line results.

6.3. Torque Measurement

The measurement of torque is one of the most important aspects of the experimental characterization, since the mechanical power extracted by the rotor is obtained from the product between torque and angular velocity. In this work, two different approaches were considered to estimate the torque acting on the rotor. The first approach is based on the resisting torque imposed by the hysteresis brake, while the second approach estimates the torque from the angular motion measured by the encoder.

The brake-based method provides controlled operating points because the resisting torque is imposed externally through the current applied to the brake. This makes it suitable for obtaining the turbine performance under different loading conditions. However, this method is limited by the available brake calibration curve and by the stability of the rotor under each brake condition. For this reason, an additional encoder-based method was also considered. This second approach uses the transient angular response of the rotor to estimate the torque from the rotor dynamics, allowing additional information to be obtained in operating regions that are not fully covered by the brake-based measurements.

The combination of both methods was adopted in order to reconstruct the experimental performance curve over the widest possible range of tip speed ratios. This is particularly relevant in the present thesis because both the experimental and numerical analyses focus on the low-TSR regime, where the power levels are small and the torque measurement is sensitive to experimental uncertainty.

6.3.1. Torque from Brake

The first torque measurement approach was based on the hysteresis brake connected to the lower part of the turbine shaft. This method follows the experimental procedure implemented in the previous work by Molano Otálora, where the brake was selected as the mechanical load because it allows a controlled resisting torque to be applied to the rotor without requiring an electrical generator or battery system. In this configuration, the torque is obtained from the calibration curve of the brake as a function of the applied current (Figure 6-3).

The test started with the turbine rotating freely, with no current supplied to the brake. This condition corresponds to the free-running state of the rotor. Then, the current applied to the brake was progressively increased, producing a gradual increase in the resisting torque. For each braking condition, the rotational speed of the shaft was measured. The corresponding torque value was then determined from the brake calibration curve. This procedure was repeated until the turbine slowed down and eventually stopped.

For each operating point, the measured rotational speed was converted from revolutions per minute to angular velocity:

$$\omega = \frac{2\pi \cdot RPM}{60} \tag{6.1}$$

where ω is the angular velocity in rad/s.

The mechanical power at the shaft was then calculated as:

$$P_{mech} = T\omega \tag{6.2}$$

where T is the resisting torque obtained from the brake calibration curve. Under a quasi-steady operating condition, the resisting torque imposed by the brake is assumed to balance the aerodynamic torque produced by the rotor. Therefore, the product $T\omega$ represents the mechanical power extracted at that operating point.

The power available in the incoming wind was calculated independently from the flow properties:

$$P_{wind} = \frac{1}{2}\rho A U_\infty^3 \tag{6.3}$$

where ρ is the air density, A is the projected rotor area, and U_∞ is the free-stream velocity. This quantity does not represent the turbine output power; it represents the kinetic power available in the airflow passing through the rotor swept area.

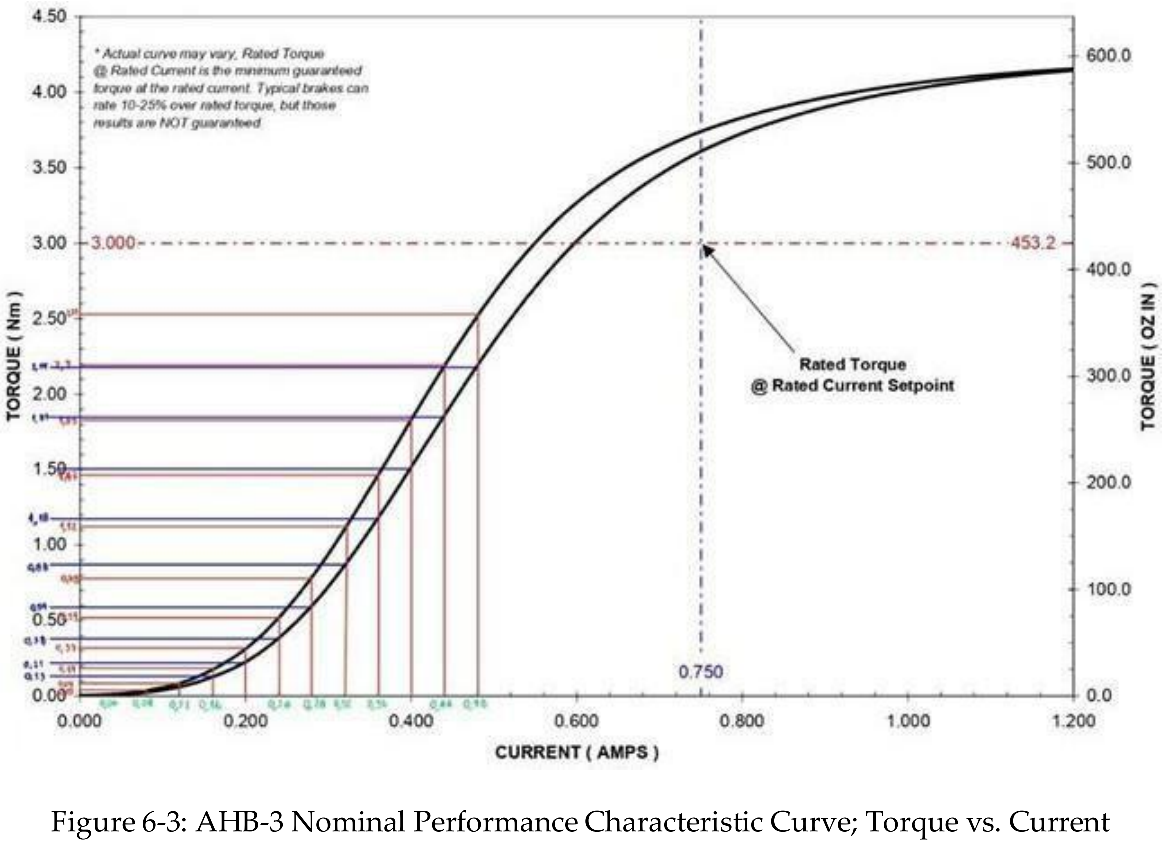

Figure 6-3: AHB-3 Nominal Performance Characteristic Curve; Torque vs. Current

The power coefficient was calculated as the ratio between the mechanical power at the shaft and the available wind power:

$$C_p = \frac{P_{mech}}{P_{wind}} \tag{6.4}$$

The tip speed ratio was calculated as:

$$TSR = \frac{\omega R}{U_\infty} \tag{6.5}$$

where R is the rotor radius. Therefore, each braking condition provides one experimental operating point in the C_p-TSR curve.

6.3.2. Torque from Encoder

As a complementary method, the torque was also estimated from the transient rotational response measured with the encoder. This approach follows the methodology used in previous wind turbine experiments at Universidad de los Andes under the supervision of Prof. Álvaro Pinilla [44], where an encoder was used to measure the rotor response in time. In that work, the encoder was preferred over a DC motor because it introduced little mechanical load on the rotor and produced a less noisy signal. Since the encoder generates pulses after a fixed angular displacement, the time between consecutive pulses can be used to calculate the instantaneous angular velocity of the rotor.

In the present work, the encoder recorded the angular position of the rotor as a function of time during transient operating conditions. From this signal, the angular velocity was obtained as:

$$\omega = \frac{d\theta}{dt} \tag{6.6}$$

and the angular acceleration was calculated as:

$$\alpha = \frac{d\omega}{dt} \tag{6.7}$$

Following the procedure described in the previous experimental work, the angular velocity response can be fitted with a smooth curve and then differentiated to obtain the angular acceleration. The torque is then estimated from the rotational equation of motion:

$$T = I\alpha \tag{6.8}$$

where T is the net torque acting on the rotor, I is the moment of inertia of the rotating system, and α is the angular acceleration. In the referenced work, this same relation was used after fitting the acceleration curve, and the mechanical power was then calculated from the product between torque and angular velocity.

Once the torque was estimated, the mechanical power was calculated as:

$$P_{mech} = Q\omega \tag{6.9}$$

The corresponding power coefficient was obtained using:

$$C_p = \frac{P_{mech}}{\frac{1}{2}\rho A U_\infty^3} \tag{6.10}$$

and the tip speed ratio was calculated as:

$$TSR = \frac{\omega R}{U_\infty} \tag{6.11}$$

This encoder-based method is useful because it allows the rotor behavior to be analyzed during acceleration or deceleration, rather than only at the discrete operating points imposed by the brake. Therefore, it can provide additional information in the low-TSR range where the brake-based measurements may not fully cover the turbine response.

However, the torque obtained from the encoder must be interpreted carefully. The encoder does not directly measure torque; it only measures rotor position or pulses in time. Torque is inferred through the angular acceleration and the moment of inertia of the rotor. Therefore, the method is sensitive to noise, time resolution, and the smoothing or curve-fitting procedure used before differentiating the signal. In addition, the estimated torque corresponds to the net torque acting on the rotating system, so mechanical losses such as bearing friction and any external braking torque must be considered when interpreting the result.

6.4. Data Processing

The brake-based measurements required less signal post-processing than the encoder data, since the torque values were obtained directly from the brake calibration curve. Therefore, the data processing stage focused mainly on the encoder measurements.

The encoder signal was acquired using an Arduino-based system. The cumulative encoder count was first converted into angular position using the encoder resolution:

$$\theta = \frac{2\pi N}{CPR} \tag{6.12}$$

where N is the encoder count and CPR is the number of counts per revolution. In this work, the encoder resolution was $CPR = 1000$.

The angular position signal was then processed using a Kalman filter implemented in the acquisition code. This filter was used to obtain a smoother estimation of the angular velocity of the rotor and reduce the effect of noise in the measured signal.

From the filtered angular velocity, the angular acceleration was calculated between consecutive time steps as:

$$\alpha = \frac{\omega_i - \omega_{i-1}}{\Delta t} \tag{6.13}$$

The encoder-based torque was then estimated with eq. (6.8).

A low-pass filter was applied to the calculated torque signal in order to reduce high-frequency fluctuations:

$$Q_{filt,i} = 0.05 Q_{enc,i} + 0.95 Q_{filt,i-1} \tag{6.14}$$

The sign convention was adjusted so that positive torque corresponds to torque generated by the rotor in the direction of rotation. The filtered torque values were then used, together with the angular velocity, to calculate the mechanical power, tip speed ratio, and power coefficient according to the equations introduced in Section 6.3.

6.5. Results

6.5.1. Flow and Environmental Conditions

Before analyzing the turbine performance, the flow and environmental conditions inside the wind tunnel were characterized. Although the validation of the actuator line model in this thesis is carried out using the experimental data at U_∞=10 m/s, additional measurements were taken for wind speeds between 7 and 12 m/s. These additional values were included for completeness and to document the operating range of the experimental setup.

For each wind speed, the temperature, pressure, and relative humidity were measured in order to determine the air density. The air density is required for the calculation of the available wind power, and therefore directly affects the value of the power coefficient. The free-stream velocity was also measured inside the test section and used as the reference velocity for the calculation of the tip speed ratio. The measured conditions are summarized in Table 6.

Wind tunnel fan speed [RPM]	**Nominal wind speed [m/s]**	**Temperature [°C]**	**Pressure [kPa]**	**Density [kg/m^3]**	**Kinematic viscosity [m^2/s]**
250	7	18.75	74.747	0.8924	2.033×10^{-5}
270	8	19.82	74.740	0.8888	2.047×10^{-5}

310	10	20.35	74.491	0.8910	2.039×10^{-5}
420	12	20.47	74.679	0.8861	2.060×10^{-5}

Table 6: Flow and environmental conditions

6.5.2. Power Coefficient Obtained from Brake Method

The brake-based results in Figure 6-4 show the variation of the power coefficient as a function of tip speed ratio for the tested wind speeds. Each point corresponds to a braking condition, where the torque was obtained from the brake calibration curve and the rotational speed was measured experimentally. The dotted curves represent polynomial trendlines used only to visualize the tendency of the data.

For all wind speeds, the rotor operates in a low TSR range, approximately between:

$$0.6 < TSR < 1.15$$

The curves show that C_p decreases as the tip speed ratio approaches the free-running condition. This behavior is expected because, at high TSR values in the brake test, the applied torque becomes small, and the extracted mechanical power tends to zero. In contrast, when braking torque is applied, the rotor slows down but produces useful shaft power, leading to a higher value of C_p.

For the reference case used for numerical validation, U_∞ = 10 m/s, the maximum brake-based power coefficient is approximately 0.076 at TSR = 0.63. After this point, the power coefficient decreases as TSR increases. Near TSR≈0.9, the power coefficient approaches zero, corresponding to operating conditions with very low extracted mechanical power.

The results for 7 and 8 m/s show a similar trend to the 10 m/s case, with maximum C_p values around 0.07–0.08. The 12 m/s case reaches a significantly higher maximum value, close to C_p 0.16. This difference may indicate that the rotor performs better at higher Reynolds number or that the brake measurement is more effective at higher mechanical power levels. However, since the numerical validation in this thesis is performed at 10 m/s, the 12 m/s case is mainly used to document the broader experimental behavior of the turbine.

Although the brake method provides calibrated torque values, the resulting performance curve is limited to the operating points reached during the progressive braking procedure. For the reference case U_∞=10 m/s, the brake-based data mainly covers the range between TSR≈0.63 and TSR≈0.91. Therefore, the lower-TSR region is not fully described by this method.

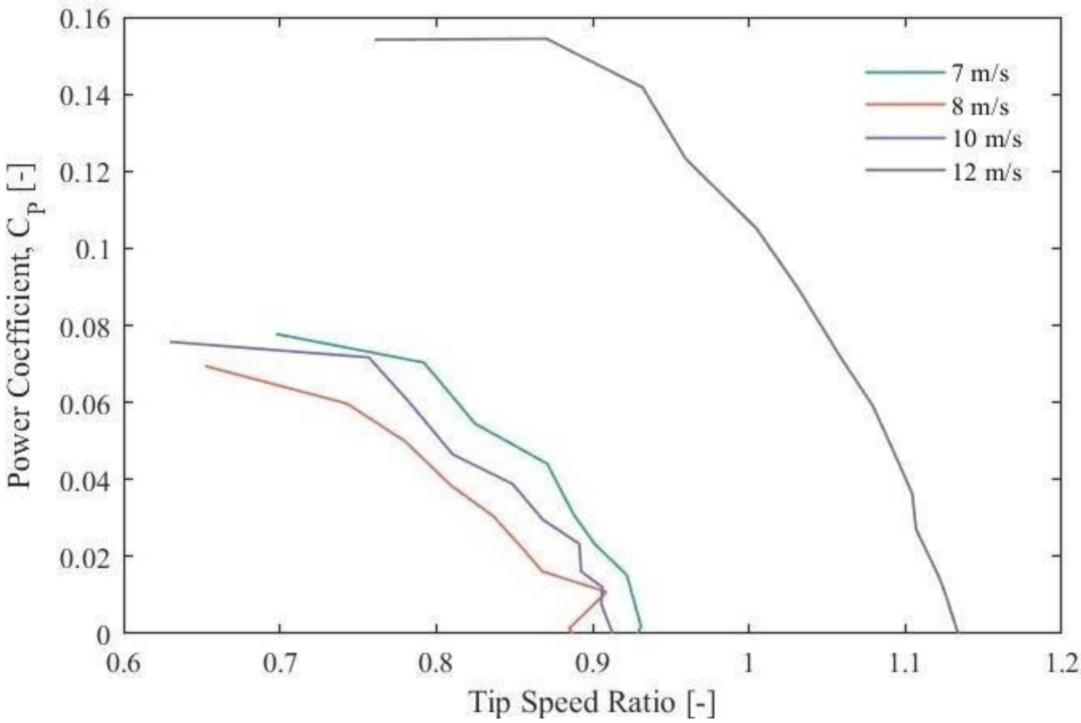

Figure 6-4: Brake-based power coefficient as a function of TSR for different wind speeds

In order to obtain additional information in this region, the brake-based measurements were complemented with encoder-based torque estimation. Since the encoder records the transient rotor motion, it allows the turbine response to be evaluated over a wider range of TSR values, including points below those reached with the brake method.

For this reason, the following section presents the power coefficient obtained from the encoder-based method.

6.5.3. Power Coefficient Obtained with Encoder Method

The results based on the encoder were obtained for the same wind speed conditions considered in the brake-based measurements: U_∞ =7, 8, 10, and 12 m/s. The encoder recorded the transient rotational response of the rotor, and the corresponding angular velocity was used to estimate the torque, mechanical power, tip speed ratio, and power coefficient according to the procedure described in Section 6.4.

Figure 6-5 shows the rotor speed response measured with the encoder. For all wind speeds, the rotor accelerates from rest until reaching a quasi-steady rotational speed. As expected, higher wind speeds produce higher final rotational speeds. The lowest stabilized speed is observed for the 7 m/s case, while the 12 m/s case reaches the highest rotational speed, close to 480 rpm.

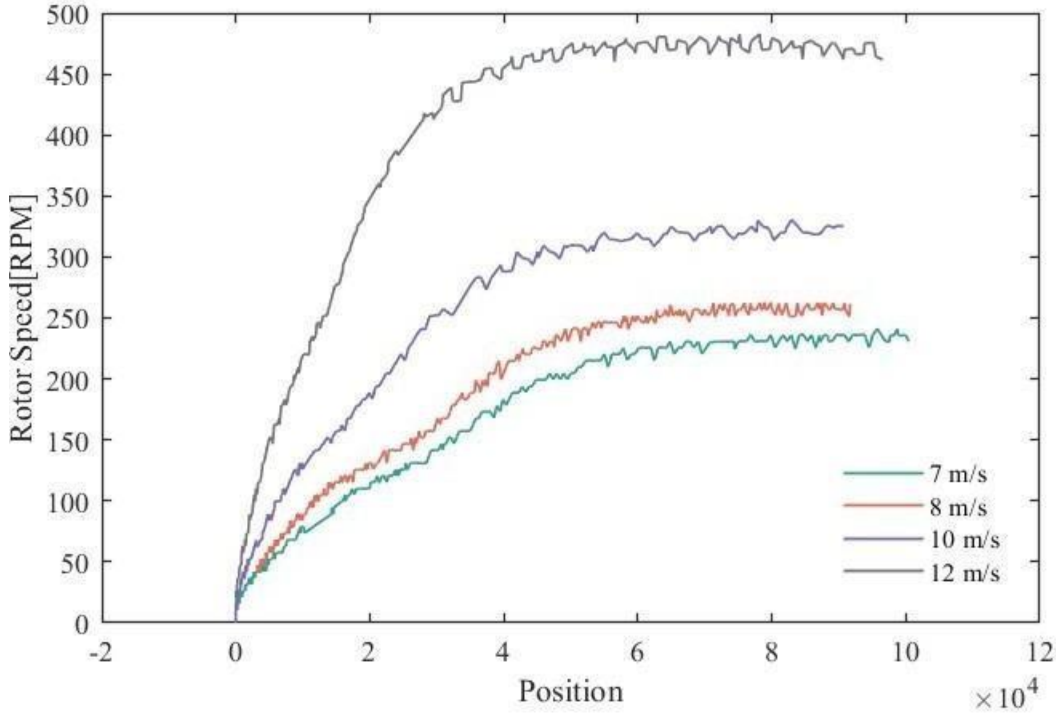

Figure 6-5: Rotor speed response measured with the encoder

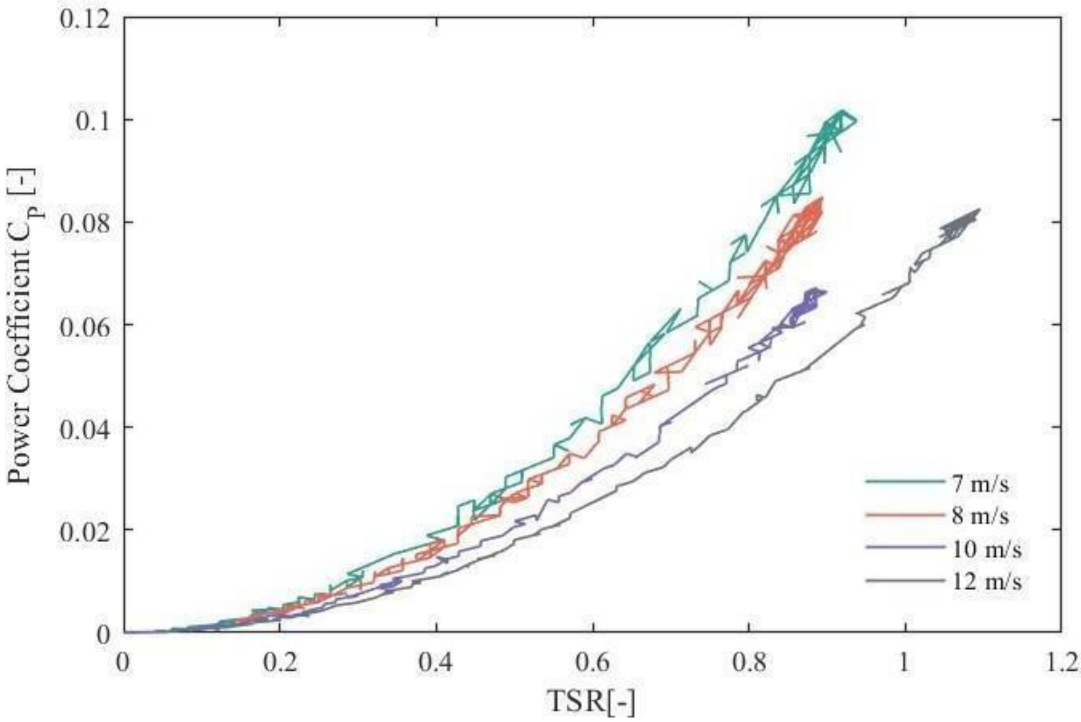

Figure 6-6: Encoder-based power coefficient as a function of TSR

Figure 6-6 presents the corresponding encoder-based C_p-TSR curves. The results show an increasing trend of C_p with TSR over the measured range. For the 10 m/s case, which is the reference condition used for comparison with the actuator line simulations, the maximum encoder-based value is approximately C_p=0.065, occurring near TSR=0.9. The remaining wind speeds show a similar increasing behavior, with the highest values reached near the upper end of the measured TSR range.

These results provide a complementary description of the turbine performance obtained from the transient rotor response. A more detailed comparison between the encoder-based and brake-based curves is presented in Section 6.5.4.

6.5.4. Comparison and Discussion

The results based on the brake and encoder provide complementary information about the performance of the Darrieus rotor. Both methods were applied to the same wind speed range, from 7 to 12 m/s, but they are based on different physical measurements. The brake method estimates the torque from the calibration curve of the hysteresis brake, while the encoder method estimates the torque from the transient rotor response using the angular acceleration and the moment of inertia of the rotating system.

The brake-based curves represent loaded operating points. In this method, the resisting torque is progressively increased, and the rotor speed decreases accordingly. For this reason, the brake method is more appropriate for obtaining calibrated values of mechanical power and power coefficient under controlled loading conditions. In the brake results, the power coefficient reaches a maximum at intermediate low values of TSR and then decreases as the rotor approaches the free-running condition. This behavior is expected because, near the free-running condition, the applied braking torque is small and therefore the useful mechanical power extracted from the shaft tends to zero.

For the reference case U_∞ =10 m/s, the brake-based curve gives a maximum power coefficient of approximately C_{pmax}≈0.076 at approximately TSR≈0.63.

The encoder-based curves show a different trend. In this case, the power coefficient increases with TSR over the measured range. This difference occurs because the encoder method does not represent the same type of operating condition as the brake method. Instead of measuring steady loaded points, the encoder records the transient acceleration of the rotor from rest toward its free-running speed. Therefore, the torque is not measured directly but inferred from the angular acceleration. As a result, the encoder-based torque and power coefficient are more sensitive to the filtering procedure, the time resolution of the acquisition system, and the assumed moment of inertia.

Despite these differences, the encoder results are still useful because they provide a continuous description of the rotor response and help complete the low-TSR region that is not fully covered by the brake data. The brake-based measurements are limited to the discrete operating points imposed by the braking procedure. In contrast, the encoder data provides additional information during the transient acceleration phase, allowing the rotor behavior to be observed over a wider range of operating points.

For the 10 m/s case, the encoder-based curve reaches a value close to: C_p≈0.065 near TSR≈0.9.

This value is of the same order of magnitude as the brake-based result, although the maximum occurs at a different TSR. The difference in the location of the maximum should not be interpreted as a contradiction, since the two methods do not measure identical operating conditions. The brake method corresponds to externally loaded points, while the encoder method corresponds to the transient dynamic response of the rotor.

Overall, both methods confirm that the Darrieus rotor operates with relatively low power coefficients in the investigated range. For the wind speeds between 7and 10 m/s, the measured $C_p$values remain below approximately 0.1. The 12 m/s brake-based curve reaches a higher value, close to 0.16, suggesting improved performance at higher wind speed. However, since the numerical simulations were carried out at 10 m/s, the comparison with the actuator line model focuses on the 10 m/s experimental data.

Therefore, the brake-based curve is considered the primary experimental reference for quantitative validation, while the encoder-based curve is used as a complementary dataset to support the interpretation of the low-TSR turbine response. The combined results indicate that the turbine operates in a strongly unsteady low TSR regime, where the extracted mechanical power is small and the measurement of torque is sensitive to the selected experimental method.

The experimental data obtained in this chapter provides the reference performance curve used to assess the numerical actuator line simulations. In particular, the 10 m/s brake-based result is used as the main validation case, while the encoder-based data provides additional information on the transient rotor behavior and the low-TSR operating range.

7 Conclusion and Future Work

7.1. Comparison between Computational and Experimental Results

The main objective of this thesis was to evaluate whether an actuator line model could be used to predict the aerodynamic performance of a small VAWT and to compare the numerical results with wind tunnel measurements. The study focused on the low TSR range, since this was the operating region of interest for both the numerical simulations and the experimental campaign. In this sense, the work was not intended to obtain a complete high TSR performance map, but rather to assess the ability of the numerical model to reproduce the low TSR power behavior of the turbine.

The comparison between the computational and experimental results shows that both approaches lead to the same general conclusion: the turbine produces low power coefficients under the investigated operating conditions. The wind tunnel results showed that the turbine is able to generate positive mechanical power, but the measured values of C_p remain limited. For the reference case at 10 m/s, the brake-based measurements produced a maximum power coefficient of approximately 0.076 at a TSR close to 0.63, followed by a reduction of C_p as the TSR increased toward values close to 1. The encoder-based results were used to complement the brake measurements in the low-TSR region, where the brake method alone did not provide complete information.

The actuator line simulations also predicted low power production in the investigated low-TSR range. The numerical C_p curve showed positive values mainly at the lower tip-speed ratios, with the maximum occurring around TSR = 0.4–0.5. As TSR increased, the predicted power coefficient decreased progressively, approached zero, and became negative at TSR = 1.0. Therefore, the ALM captured the general low-performance behavior of the turbine, but it did not reproduce the experimental C_p -TSR curve exactly. In particular, the numerical maximum occurred at a lower TSR than the experimental maximum, and the decrease of C_p at higher TSR was stronger in the numerical model. This indicates that the model was able to reproduce the qualitative behavior of the turbine, but not the precise position of the experimental maximum or the exact magnitude of the power coefficient at all operating points.

From this comparison, the ALM can be considered a useful engineering tool for preliminary global performance prediction. Its main advantage is that it avoids the need to explicitly mesh the rotating three-dimensional blade geometry, reducing the computational cost. However, it cannot be considered a complete substitute for a full 3D blade-resolved simulation. The ALM depends on the aerodynamic coefficient database, the dynamic stall correction, and the force projection method, so it is better suited to estimating mean torque and power trends than to resolving the detailed unsteady flow physics around the real turbine.

7.2. Interpretation of the Discrepancies

The quantitative differences between the ALM simulations and the wind tunnel measurements can be attributed to the combined effect of aerodynamic, numerical, and experimental factors. These differences are expected because the turbine operates in a low TSR range, where the flow is highly unsteady and the mean power coefficient depends strongly on the instantaneous direction and timing of the aerodynamic forces.

The first factor is the low TSR operating regime itself. In this range, the blade relative velocity and angle of attack vary significantly during each revolution. As a consequence, the blades can experience large regions of separated flow and dynamic stall. Under these conditions, the average torque is very sensitive to the timing of stall onset, vortex formation, and force recovery. Therefore, even small differences in the predicted AoA history or in the phase of the aerodynamic loads may shift the C_p–TSR curve or modify the predicted maximum power coefficient.

A second factor is the dynamic stall correction used in the ALM. The numerical results showed that the dynamic stall model is essential for obtaining positive power coefficients in the investigated range. Without this correction, the aerodynamic response predicted negative Cp values. However, the dynamic stall model should be interpreted as an engineering correction rather than a complete physical resolution of the stall process. Its behavior depends on empirical parameters and on the input AoA history, so it can strongly influence the final predicted torque. This explains why the ALM can reproduce the general low power behavior of the turbine while still differing from the experimental curve in the exact value and position of the maximum C_p.

Another important source of difference is the aerodynamic coefficient database used as input for the ALM. Since the blade profile was reconstructed from the real turbine and does not correspond to a standard airfoil, the lift and drag coefficients were obtained from two-dimensional CFD simulations. These coefficients were then extrapolated to the full AoA range using the Viterna–Corrigan method. This procedure was necessary because the actuator line model requires aerodynamic data over the complete rotation, but it introduces uncertainty in the post-stall and deep-stall regions. This uncertainty becomes particularly important at low TSR, where the blade sections may operate far outside the attached-flow range during part of the revolution.

The actuator line approximation itself also contributes to the discrepancy. The ALM is able to represent the global aerodynamic effect of the blades at a relatively low computational cost, but it does not resolve the blade surface or the detailed three-dimensional flow around the real geometry. Therefore, effects such as local separation, tip losses, support and shaft interactions, and detailed blade–wake interaction are simplified or absent. This is especially relevant for the present turbine because the blade has a twisted and helical three-dimensional shape. Different blade sections may therefore experience different local aerodynamic conditions at the same instant, which is difficult to reproduce accurately using sectional aerodynamic coefficients and actuator-line force projection.

Experimental uncertainty must also be considered. The turbine produced low mechanical power, so the calculated power coefficient is sensitive to small variations in measured torque, angular velocity, wind speed, air density, and mechanical losses. The brake-based method provides a direct way to impose load on the turbine, but it depends on the braking process and on the accuracy of the torque estimation. The encoder-based method complements the brake data in the low-TSR region, but it is based on the transient rotational response of the rotor and is therefore affected by inertia, friction, and acceleration effects. For this reason, the experimental C_p curve also contains uncertainty, especially where torque values are small.

For these reasons, the disagreement between the numerical and experimental C_p–TSR curves should not be interpreted only as an error of the ALM. Rather, it reflects the difficulty of modelling and measuring a small, non-standard VAWT operating in a low-TSR dynamic-stall regime. The ALM captures the main qualitative behavior of the turbine, but a fully quantitative match would require a more accurate aerodynamic database, calibrated dynamic stall parameters, improved experimental torque measurements, and possibly a higher-fidelity three-dimensional CFD model.

7.3. Practical Implications of the Low Measured power

The low measured power coefficient has an important practical implication for the evaluation of the turbine as an energy-production device. The initial motivation of this work was related to the need to verify the performance of a turbine that had been presented as capable of producing significant power. However, the wind tunnel results showed that, under the investigated operating conditions, the turbine produces limited mechanical power. For the reference case used for numerical validation, corresponding to a wind speed of 10 m/s, the maximum brake-based power coefficient was approximately 0.076 at TSR = 0.63, and the power coefficient decreased toward very low values near TSR = 1.

This result does not mean that the turbine is unable to extract energy from the wind. The experimental measurements confirm that the rotor can generate positive mechanical power over part of the investigated operating range. However, the measured values of C_p indicate that the fraction of available wind power converted into useful mechanical power is low. Therefore, the turbine should not be evaluated only by its ability to rotate or by its visual association with renewable energy, but by quantitative indicators such as torque, power coefficient, operating TSR range, mechanical losses, and expected annual energy production.

The practical relevance of this result is particularly important for small VAWTs used in architectural, urban, or demonstrative applications. In these contexts, the visual presence of a wind turbine can suggest an important renewable energy contribution, but the actual energy production may be limited if the aerodynamic efficiency is low or if the local wind resource is not favorable. For this reason, claims of high-power generation should be supported by independent measurements performed under controlled conditions and, ideally, by field data representative of the intended installation site.

In the present case, the low experimental C_p values suggest that the turbine, in its current configuration and under the tested conditions, has limited potential as a significant energy-production system. Its role may be more appropriate as a demonstrative or educational renewable energy device unless further optimization or field validation shows higher performance under realistic operating conditions. A complete assessment of this point would require additional information that was outside the scope of this thesis, including electrical conversion efficiency, mechanical losses, annual wind speed distribution, installation effects, lifecycle impact, and comparison with alternative renewable energy technologies.

7.4. Limitations of Present Work

The present work has several limitations that should be considered when interpreting the comparison between the numerical and experimental results. These limitations are related to both the numerical modelling approach and the experimental measurements.

From the numerical point of view, the first limitation is that the simulations were performed only for the Darrieus component of the turbine. The real device corresponds to a hybrid Savonius–Darrieus configuration, but the complete hybrid geometry was not included in the OpenFOAM model because of the complexity of reconstructing and meshing the full turbine. Therefore, the numerical results represent the aerodynamic behavior of the Darrieus rotor only, rather than the complete physical turbine.

A second limitation is associated with the actuator line method itself. The ALM was selected because it provides a computationally efficient alternative to a fully meshed rotating turbine geometry. However, this efficiency is obtained by replacing the real blades with actuator lines and by applying body forces to the flow. As a result, the model does not directly resolve the detailed flow around the blade surface, the local separation process, the dynamic stall vortex, tip effects, support-arm effects, or shaft interactions. For this reason, the ALM results should be interpreted as global performance predictions rather than as a complete description of the three-dimensional flow physics.

Another limitation is the aerodynamic database used as input for the ALM. Since the reconstructed blade profile does not correspond to a standard airfoil, the aerodynamic coefficients had to be obtained from two-dimensional CFD simulations. These data were then extended to the full AoA range using the Viterna–Corrigan extrapolation method. This step was necessary because, at low TSR, the actuator elements may reach angles of attack far outside the range directly simulated in Chapter 4. However, the extrapolated coefficients in the post-stall and deep-stall regions remain a source of uncertainty.

The dynamic stall correction also represents a limitation. Dynamic stall was included because it is essential for low TSR VAWT simulations, where the angle of attack changes significantly during each revolution. Nevertheless, the Leishman–Beddoes-type correction used in turbinesFoam is a semi-empirical model. It improves the representation of unsteady aerodynamic effects, but it does not directly resolve the full dynamic stall process, including vortex formation, vortex shedding, and reattachment. In addition, the model parameters were not independently calibrated using experimental force data for the reconstructed blade profile.

From the experimental point of view, the main limitation is related to the low mechanical power produced by the turbine. Since the measured torque and power are small, the calculated power coefficient is sensitive to uncertainties in torque, angular velocity, wind speed, air density, mechanical friction, and braking procedure. The brake-based method provides calibrated loaded operating points, but it is limited to the TSR range reached during the braking process. The encoder-based method complements the brake data in the low TSR region, but it estimates torque indirectly from the transient rotational response of the rotor and is therefore affected by inertia and acceleration effects.

Finally, the present work did not include a complete uncertainty analysis, a field-performance assessment, or an annual energy production estimate. Therefore, although the results provide useful information about the aerodynamic performance of the turbine under controlled wind tunnel conditions, they cannot alone define the long-term energy contribution of the device in a real installation. These aspects should be addressed in future work.

7.5. Future Work

Future work should first focus on improving the experimental characterization of the turbine. Since the measured power output is low, the calculated power coefficient is sensitive to small errors in torque, angular velocity, wind speed and mechanical losses. For this reason, a dedicated torque sensor should be used to obtain a more direct measurement of the rotor torque. The mechanical losses of the shaft, bearings, brake system and transmission should also be measured separately, so that the aerodynamic torque can be isolated more accurately. In addition, repeated tests should be performed under the same wind conditions in order to evaluate the repeatability of the measurements and to build an uncertainty range for the experimental C_p–TSR curve.

The braking procedure could also be improved. In the present work, the brake-based method provides the main controlled loading reference, while the encoder-based method complements the low-TSR region through the transient rotor response. A more controlled braking system would make it possible to impose stable operating points at selected TSR values and reduce the uncertainty associated with acceleration and deceleration phases. This would allow a clearer comparison with the numerical simulations, where the TSR is imposed directly.

From the numerical point of view, future work should improve the aerodynamic database used by the ALM. The present database was obtained from two-dimensional CFD simulations and then extended to the full AoA range using the Viterna–Corrigan method. Since low-TSR operation involves large angles of attack and separated-flow conditions, the accuracy of the post-stall and deep-stall coefficients has a strong influence on the predicted torque. Future simulations should therefore extend the direct CFD calculation to a wider range of angles of attack and Reynolds numbers, reducing the dependence on empirical extrapolation. Independent verification of the aerodynamic coefficients could be performed using alternative approaches such as XFOIL calculations, additional numerical methods, or dedicated experimental measurements. Such comparisons would help assess the reliability of the reconstructed airfoil data and identify possible sources of uncertainty in the lift and drag coefficients used by the ALM.

A systematic sensitivity analysis of the dynamic stall parameters should also be performed. The results of the present work show that the dynamic stall correction is essential for obtaining physically meaningful ALM predictions in the low TSR range. However, the model parameters were not independently calibrated for the reconstructed blade profile. Future work should therefore evaluate how the predicted C_p–TSR curve changes when the main Leishman–Beddoes parameters are varied. If possible, the model should be calibrated using experimental force or torque data instead of relying only on literature values.

Another important development would be the comparison between the ALM and a higher-fidelity blade-resolved 3D CFD simulation. The ALM is useful because it avoids meshing the rotating blade geometry and reduces the computational cost, but it cannot fully resolve the local flow around the blade, the dynamic stall vortex, or the detailed blade–wake interaction. A full 3D CFD simulation for a limited number of representative TSR values would help identify whether the discrepancies with the experiment are mainly caused by the actuator-line approximation, the aerodynamic database, or the dynamic stall model.

Bibliography

[1] W. Tong, *Wind Power Generation and Wind Design Technology*.: WITPress, 2010.

[2] M. Castiglioni, "ALM Based on Effective Velocity Model for CFD Simulations of VAWT," 2014.

[3] M. D'ambrosio, "Vertical Axis Wind Turbines: History, Technology and Applications," 2010.

[4] Manwell et al., "Wind Energy Explained: Theory, Design and Application," 2006.

[5] Kumara et al., "Review Paper: Overview of the Vertical Axis Wind Turbines," 2017.

[6] Bhutta et al., "Vertical Axis Wind Turbines - A Review of Various Configurations and Design Techniques," 2012.

[7] Fazylova et al., "A Comparative Review of Vertical Axis Wind Turbine Design: Savonius Rotor vs. Darrieus Rotor," 2025.

[8] Ghafoorian et al., "A Systematic Investigation on the Hybrid Darrieus-Savonius Vertical Axis Wind Turbine," 2026.

[9] G. Baldassarra, "Multi-dimensional CFD Simulation of a H-Darrieus Vertical Axis Wind Turbine with OpenFOAM," 2015.

[10] M. Hansen, "Aerodynamics of Wind Turbines," 2008.

[11] K. Hermann, "Panemone Wind Turbine," 1981.

[12] V. Kharede et al., "A Review Study on Vertical Axis Wind Turbines(Lift and Drag Type) for Optimizing the Aerodynamic and Structural Performance," 2019.

[13] S. Gitifar et al., "Review of Different Vertical Axis WInd Turbine Modeling Methods," 2024.

[14] J.H. Ferziger and M. Peri, "Computational Methods for Fluid Dynamics," 2002.

[15] NASA Glenn Research Center,.

[16] J.G. Leishman, "Introduction to Aerospace Flight Vehicles," 2026.

[17] K. Rogowski, "Performance Analysis of a H-Darrieus Wind Turbine for a Series of 4-Digit NACA Airfoils," 2020.

[18] Martinez-Ojeda et al, "Vertical Axis Wind Turbines Using a 2D Hybrid Wake Actuator-Cylinder Model," 2021.

[19] Ali et al., "Effects of Tip Speed Ratio on the Blade Forces of a Small H-Darrieus Wind Turbine," 2021.

[20] Burton et al., *Wind Energy Handbook.*, 2011.

[21] J.G. Leishman, "Challenges in Modeling the unsteady Aerodynamics of Wind," 2002.

[22] E. Dyachuk et al., "Measurements of the Aerodynamic Normal Forces on a 12-kW Straight-Bladed Vertical Axis Wind Turbine," 2015.

[23] M. Caglioni, "Actuator Line Method based on the Effective Velocity Model for CFD Simulations of Vertical Axis Wind Turbines," 2015.

[24] Airfoil Tools. [Online]. http://airfoiltools.com/

[25] W. Malalasekera and H.K. Versteeg, *An Introduction to Computational Fluid Dynamics. The Finite Volume Method*, 2nd ed., 2007.

[26] OpenCFD Ltd. (2023) OpenFOAM Documentation: PIMPLE Algorithm.

[27] CFD Direct. (2025) OpenFOAM v13 User Guide: 4.6 Solution and Algorithm Control.

[28] P.R. Allmaras and S.R. Spalart, "A One Equation Turbulence Model for Aerodynamic Flows," *La Reserche Aerospatiale*, 1994.

[29] F.R. Menter, "Two-Equation Eddy Viscosity Turbulence Model for Engineering Applications," *AIAA Journal*, 1994.

[30] J.N. Sørensen and W. Shen, "Numerical Modeling of Wind Turbine Wakes," *Journal of Fluids Engineering*, 2002.

[31] P. Bachant et al., "Actuator Line Modeling of Vertical Axis Turbines," 2018.

[32] M. Faisal, "The Effect of Flat Plate Theory Assumption in Post-Stall Lift and Drag Coefficients Extrapolation with Viterna Method," *Journal of Subsea and Offshore*, 2016.

[33] L. Viterna and D. Janetzke, "Theoretical and Experimental Power from Large Horizontal Axis Wind Turbines," 1982.

[34] G. Persico et al, "Quantification of the Dynamic-Stall Model Uncertainty in yhe Performance Prediction of Vertical Axis WInd Turbines," *Journal of Physics*, 2020.

[35] P.F. Melani et al., "Tailoring the Actuator Line Theory to the Simulation of Vertical Axis Wind Turbines," *Energy Conversion and Management*, 2021.

[36] K. Mulleners and M. Raffael, "Dynamic Stall Development," 2013.

[37] E. Dyachuk and A. Goude, "Simulating Dynamic Stall Effects for Vertical Axis Wind Turbines Applying a Double Multiple Streamtube Model," *Energies*, 2015.

[38] D. Castelein et al., "Creating a Benchmark of Vertical Axis Wind Turbines in Dynamic Stall for Validating Numerical Models," 2015.

[39] R. Damiani and G. Hayman, "The Unsteady Aerodynamics Module for FAST 8," 2019.

[40] P.F. Melani et al, "The Beddoes-Leishman Dynamic Stall Model: Critical Aspects in Implementation and Calibration," *Rrenewable and Sustainable Energy Reviews*, 2024.

[41] N. Khalifa et al., "On Computational Simulations of Dynamic Stall and its Three Dimensional Nature," 2023.

[42] F. Alquarashi and M.H. Mohamed, "Aerodynamic Forces Affecting the H-Rotor Darrieus Wind Turbine," 2020.

[43] G. Molano, "Caraterización Experimental de una Turbina de Viento Comercial de Pequeña Escala," 2025.

[44] A.F. Sanchez, "Diseño y Caracterización de un rotor éolico para bajo número de Reynolds," 2015.

Appendix A – ALM Setup

A.1 BlockMeshDict

```
vertices
(
    ( -1  0.5 0 ) // 0
    (  1  0.5 0 ) // 1
    (  1 -0.5 0 ) // 2
    ( -1 -0.5 0 ) // 3
    ( -1  0.5 1 ) // 4
    (  1  0.5 1 ) // 5
    (  1 -0.5 1 ) // 6
    ( -1 -0.5 1 ) // 7
);

blocks
(
    hex (0 3 2 1 4 7 6 5)
    (32 32 24)
    simpleGrading (1 1 1)
);


boundary
(
    inlet
    {
        type patch;
        faces
        (
            (0 4 7 3)
        );
    }

    outlet
    {
       type patch;
       faces
        (
            (1 2 6 5)
        );
    }

    walls
    {
       type wall;
        faces
        (
            (0 3 2 1)
            (4 5 6 7)
        );
    }

    top
    {
       type wall;
       faces
        (
            (0 1 5 4)
        );
    }

    bottom
    {
       type wall;
        faces
        (
            (3 7 6 2)
        );
```

```
    }
);
```

A.2 SnappyHexMeshDict

```
geometry
{
    turbine
    {
        type searchableCylinder;
        point1 (0 0 0);
        point2 (0 0 1);
        radius 0.3;
    }

    turb_zone
    {
        type searchableBox;
        min (-0.55 -0.55 0);
        max (0.55 0.55 1);
    }
};

{

    // Refinement parameters
    // ~~~~~~~~~~~~~~~~~~~~~
    maxLocalCells 100000;

    maxGlobalCells 2000000;

    minRefinementCells 0;

    maxLoadUnbalance 0.10;


    nCellsBetweenLevels 1;

    resolveFeatureAngle 30;

    refinementRegions
    {
        //~ turbine
        //~ {
            //~ mode inside;
            //~ levels ((1 1));
        //~ }

        turb_zone
        {
            mode        inside;
            levels      ((1e15 2));
        }
    }


    // Mesh selection
    locationInMesh (0.3124 0 0);

    allowFreeStandingZoneFaces true;

    handleSnapProblems false;

    useTopologicalSnapDetection  false;
}



// Settings for the snapping.
snapControls
{
    // Number of patch smoothing iterations before finding correspondence
    // to surface
```

```
    nSmoothPatch 3;

    tolerance 2.0;

    // Number of mesh displacement relaxation iterations.
    nSolveIter 30;

    // Maximum number of snapping relaxation iterations. Should stop
    // before upon reaching a correct mesh.
    nRelaxIter 5;

    // Feature snapping

        // Number of feature edge snapping iterations.
        // Leave out altogether to disable.
        nFeatureSnapIter 10;

        // Detect (geometric only) features by sampling the surface
        // (default=false).
        implicitFeatureSnap true;

        // Use castellatedMeshControls::features (default = true)
        explicitFeatureSnap true;

        // Detect features between multiple surfaces
        // (only for explicitFeatureSnap, default = false)
        multiRegionFeatureSnap false;


    // wip: disable snapping to opposite near surfaces (revert to 22x behaviour)
    detectNearSurfacesSnap false;
}



// Settings for the layer addition.
addLayersControls
{
    // Are the thickness parameters below relative to the undistorted
    // size of the refined cell outside layer (true) or absolute sizes (false).
    relativeSizes true;

    // Per final patch (so not geometry!) the layer information
    layers
    {
    }

    // Expansion factor for layer mesh
    expansionRatio 1.0;


    // Wanted thickness of final added cell layer. If multiple layers
    // is the thickness of the layer furthest away from the wall.
    // See relativeSizes parameter.
    finalLayerThickness 0.3;

    // Minimum thickness of cell layer. If for any reason layer
    // cannot be above minThickness do not add layer.
    // See relativeSizes parameter.
    minThickness 0.25;

    // If points get not extruded do nGrow layers of connected faces that are
    // also not grown. This helps convergence of the layer addition process
    // close to features.
    // Note: changed(corrected) w.r.t 17x! (didn't do anything in 17x)
    nGrow 0;


    // Advanced settings

    // When not to extrude surface. 0 is flat surface, 90 is when two faces
    // are perpendicular
    featureAngle 60;
```

```
    // Maximum number of snapping relaxation iterations. Should stop
    // before upon reaching a correct mesh.
    nRelaxIter 5;

    // Number of smoothing iterations of surface normals
    nSmoothSurfaceNormals 1;

    // Number of smoothing iterations of interior mesh movement direction
    nSmoothNormals 3;

    // Smooth layer thickness over surface patches
    nSmoothThickness 10;

    // Stop layer growth on highly warped cells
    maxFaceThicknessRatio 0.5;

    // Reduce layer growth where ratio thickness to medial
    // distance is large
    maxThicknessToMedialRatio 0.3;

    // Angle used to pick up medial axis points
    // Note: changed(corrected) w.r.t 16x! 90 degrees corresponds to 130 in 16x.
    minMedianAxisAngle 90;

    // Create buffer region for new layer terminations
    nBufferCellsNoExtrude 0;


    // Overall max number of layer addition iterations. The mesher will exit
    // if it reaches this number of iterations; possibly with an illegal
    // mesh.
    nLayerIter 50;

    // Max number of iterations after which relaxed meshQuality controls
    // get used. Up to nRelaxIter it uses the settings in meshQualityControls,
    // after nRelaxIter it uses the values in meshQualityControls::relaxed.
    nRelaxedIter 20;
}



// Generic mesh quality settings. At any undoable phase these determine
// where to undo.
meshQualityControls
{
    //- Maximum non-orthogonality allowed. Set to 180 to disable.
    maxNonOrtho 65;

    //- Max skewness allowed. Set to <0 to disable.
    maxBoundarySkewness 20;
    maxInternalSkewness 4;

    //- Max concaveness allowed. Is angle (in degrees) below which concavity
    //  is allowed. 0 is straight face, <0 would be convex face.
    //  Set to 180 to disable.
    maxConcave 80;

    //- Minimum pyramid volume. Is absolute volume of cell pyramid.
    //  Set to a sensible fraction of the smallest cell volume expected.
    //  Set to very negative number (e.g. -1E30) to disable.
    minVol 1e-13;

    //- Minimum quality of the tet formed by the face-centre
    //  and variable base point minimum decomposition triangles and
    //  the cell centre.  Set to very negative number (e.g. -1E30) to
    //  disable.
    //     <0 = inside out tet,
    //      0 = flat tet
    //      1 = regular tet
    minTetQuality 1e-30;

    //- Minimum face area. Set to <0 to disable.
```

```
    minArea -1;

    //- Minimum face twist. Set to <-1 to disable. dot product of face normal
    //- and face centre triangles normal
    minTwist 0.05;

    //- minimum normalised cell determinant
    //- 1 = hex, <= 0 = folded or flattened illegal cell
    minDeterminant 0.001;

    //- minFaceWeight (0 -> 0.5)
    minFaceWeight 0.05;

    //- minVolRatio (0 -> 1)
    minVolRatio 0.01;

    //must be >0 for Fluent compatibility
    minTriangleTwist -1;

    //- if >0 : preserve single cells with all points on the surface if the
    //  resulting volume after snapping (by approximation) is larger than
    //  minVolCollapseRatio times old volume (i.e. not collapsed to flat cell).
    //  If <0 : delete always.
    //minVolCollapseRatio 0.5;


    // Advanced

    //- Number of error distribution iterations
    nSmoothScale 4;
    //- amount to scale back displacement at error points
    errorReduction 0.75;



    // Optional : some meshing phases allow usage of relaxed rules.
    // See e.g. addLayersControls::nRelaxedIter.
    relaxed
    {
        //- Maximum non-orthogonality allowed. Set to 180 to disable.
        maxNonOrtho 75;
    }
}
```

A.3 fvOptions

```
turbine
{
    type            crossFlowTurbineALSource;
    active          on;

    crossFlowTurbineALSourceCoeffs
    {
        fieldNames          (U);
        selectionMode       cellSet; // cellSet || points || cellZone`
        cellSet             turbine;

        origin              (0 0 0.45);
        axis                (0 0 -1);     // Negative for opposite rotation
        rotorRadius         0.25;

        freeStreamVelocity  (10 0 0);

        UInf                10;          // freestream speed magnitude
        rhoInf              0.89;       // air density
        rhoRef              0.89
        rotorArea           0.4;    // π * 0.3^2 = 0.283

        tipSpeedRatio       1.2;
        tsrAmplitude        0.0;        // Amplitude for TSR oscillation 0.1
        tsrPhase            0.0;         // Angle of first peak (rad) 1.9

        dynamicStall
```

```
{
    active              on;
    dynamicStallModel   LeishmanBeddoesSGC;
    LeishmanBeddoesSGCCoeffs
    {
        Tp          1.7;        // Default = 1.7
        Tf          3.0;       // Default = 3.0
        TAlpha      6.25;         // 6.25
        alphaDS0DiffDeg 5;      //3.8
        r0          0.02;
        Tv          11; //11
        Tvl         8.7; //8.7
        B1          0.5;
        eta         0.95;
        E0          0.12;
        ReList        (1e6);
        CNAlphaList   (2.0);
        CD0List       (0.02);
        CN1List       (2);
        alpha1List    (18);
        S1List        (0.5);
        S2List        (1.5);
        // Uncomment lists below to disable automatic calculations
        // ReList      (4e4 8e4 1.6e5 3.6e5 7e5 1e6 2e6 5e6);
        // CNAlphaList (3.2397 4.7255 5.2274 5.6084 5.8048 5.8904 5.9625 6.2771);
        // CD0List     (0.0232 0.0177 0.0139 0.0111 0.0094 0.0089 0.0082 0.0078);
        // CN1List     (0.34311 0.57438 0.72628 0.87407 0.97478 1.0264 1.1324 1.2367);
        // alpha1List  (7.7466 9.0006 10.2013 11.3078 12.1635 12.6109 13.7035 14.0118);
        //S1List      (0.70707 1.2121 1.8182 2.1212 2.4242 2.5253 2.8283 4.2424);
       //S2List      (1.5152 2.4242 3.7374 5.1515 5.8586 6.1616 6.6667 6.6667);


  }
}

flowCurvature
{
    active              on;
    flowCurvatureModel  Goude; // Goude || MandalBurton
}

blades
{
    blade1
    {
        writePerf   true;
        writeElementPerf true;
        nElements   18;
        endEffects  on;
        elementProfiles (myairfoil);
        pitchAxis (0 0 1);
        elementData
        // axialDistance, radius, azimuth, chord, chordMount, pitch
        (
          (-0.400   0.25   157.0   0.19   0.5    -42.0)
          (-0.311   0.25   149.5  0.19   0.5     -33.89)
          (-0.222   0.25   142.1  0.19   0.5     -25.78)
          (-0.133   0.25   134.6  0.19   0.5     -17.67)
          (-0.044   0.25   123.2  0.19   0.5     -9.56)
          (+0.044   0.25   119.8  0.19   0.5     -1.44)
          (+0.133   0.25   112.4  0.19   0.5     6.67)
          (+0.222   0.25   104.9  0.19   0.5     14.78)
          (+0.311   0.25   97.5   0.19   0.5     22.89)
          (+0.400   0.25   90.0   0.19   0.5     31.0)
        );
    }
    blade2
    {
        $blade1;
        //writePerf   false;
        //writeElementPerf false;
        azimuthalOffset 120.0; // Degrees
    }
```

```
            blade3
            {
                $blade1;
                azimuthalOffset 240.0;
            }
        }



        shaft
        {
            nElements   20;
            elementProfiles (cylinder);
            elementData
            ( // axialDistance, diameter
                (-0.4 0.05)
                (0.4 0.05)
            );
        }

        profileData
        {
            myairfoil
            {
                tableType   multiRe; // singleRe (default) || multiRe

                ReList // For tableType = multiRe
                (
                    #include "/home/astrogiulia/OpenFOAM/astrogiulia-
v2412/turbinesFoam/crossFlowTurbine_multiRe/foilData/myairfoil_multiRe_Re"
                );
                clData // For tableType = multiRe
               (
                    #include "/home/astrogiulia/OpenFOAM/astrogiulia-
v2412/turbinesFoam/crossFlowTurbine_multiRe/foilData/myairfoil_multiRe_cl"
                );
                cdData // For tableType = multiRe
               (
                   #include "/home/astrogiulia/OpenFOAM/astrogiulia-
v2412/turbinesFoam/crossFlowTurbine_multiRe/foilData/myairfoil_multiRe_cd"
                );

            }
            cylinder
            {
                data ((-180 0 1.1)(180 0 1.1));
            }
        }
    }
```

List of Figures

List of Tables

List of symbols

Variable	Description	SI unit
A	Rotor swept area	m^2
a	Axial induction factor	-
C_L	Lift coefficient	-
C_D	Drag coefficient	-
C_M	Momentum coefficient	-
C_P	Power coefficient	-
c	Chord	m
H	Height	m
I	Moment of inertia	$kg \cdot m^2$
P	Power	W
R	Radius	m
Re	Reynolds number	-
T	Torque	Nm
U_∞	Free stream velocity	m/s
α	Angle of Attack	°
λ	Tip speed ratio	-
ρ	Density	kg/m^3
ω	Angular velocity	rad/s

List of Abbreviations

Abbreviation	**Meaning**
VAWT	Vertical Axis Wind Turbine
3D	Three dimensions
CFD	Computational Fluid Dynamics
ALM	Actuator Line Method
2D	Two Dimensions
AoA	Angle of Attack
HAWT	Horizontal Axis Wind Turbine
NACA	National Advisory Committee for Aeronautics
TSR	Tip Speed Ratio
AL	Actuator Line
LE	Leading Edge
TE	Trailing Edge
AR	Aspect Ratio
SST	Shear Stress Transport
RANS	Reynolds Averaged Navier Stokes
RAS	Reynolds Averaged System
GAMG	Geometric-Algebraic MultiGrid
CPR	Counts Per Revolution